An Analysis of Extreme-Scale, Load-Aligned Wind Turbines

A Dissertation

Presented to

the faculty of the School of Engineering and Applied Science

University of Virginia

in partial fulfillment of

the requirements for the degree

Doctor of Philosophy

by

Carlos C. Noyes

December 2018

Approval Sheet

This Dissertation is submitted in partial fulfillment of the requirements for the degree of

Doctor of Philosophy

Author Signature: Carlos Noyes

This Dissertation has been read and approved by the examining committee:

Advisor: Eric Loth

Committee Member Sean Agnew

Committee Member: Haibo Dong

Committee Member: Daniel Quinn

Committee Member: Chao Qin

Committee Member: Patrick Moriarty

Accepted for the School of Engineering and Applied Science:

Craig H. Benson, School of Engineering and Applied Science

December 2018

Contents

Acknowledgements

I would like to thank Dr. Eric Loth, for his leadership, guidance, and patience throughout my PhD studies. He has taught me a great many things, both technical and non-technical skills that will aid me throughout the entirety of my future career. I would like to thank the other members of Dr. Loth's research group specifically, Dr. Chris Qin, for his mentorship and for his continual assistance during my project. I would like to thank my father and mother, Michael and Margarita Noyes for preparing me for and encouraging me through this journey. I would like to thank Mrs. Brenda Perkins who straightened out a multitude of bureaucratic messes in which I found myself. Finally, I would like to thank ARPA-e for funding my research project.

Abstract

Over time the cost of wind energy has dropped and the size of wind turbines has grown. This trend has been consistent over the last several decades, but will the trend continue? Wind turbine designers are reaching technical barriers that limit the size of wind turbines. One such barrier is the out of plane bending loads the blades must support. A 100m long rotor blade experiences loads of a magnitude that no other aerospace structure has ever been designed to support. The blade must both be strong enough to withstand the ultimate and fatigue loads, and stiff enough not to deflect backwards to strike the tower. Satisfying these concerns has become cost prohibitive at extreme-scales (>10MW). One clever solution is the load-aligned rotor, which offsets the thrust bending loads with the centrifugal bending load resulting from downwind coning. The first challenge of the load-aligned rotor is that it must operate in the downwind configuration, and therefore must pass through the wake of the tower. The effect of the tower shadow must be fully understood as it may undo the benefits experienced by load-alignment. The second challenge is that the effects of coning as a method of load-reduction are not fully understood. This dissertation explores these two areas (tower shadow and load-alignment) in extensive detail. Some key findings were that tower shadow significantly effects wind turbine aerodynamics. The tower shadow can excite oscillatory modes for small-scale wind turbines, which typically have relatively stiff blades and fast rotational rates, but can be mitigated with a tower fairing. For large scale wind turbines, which typically have relatively flexible blades and slower rotational rates, operating under field-conditions tower shadow has relatively minimal effect, and no tower fairing is required. Downwind coning was shown to reduce loads sufficiently that a load-aligned rotor could meet structural and power constraints using 26% less material that conventional upwind rotors. Load-alignment via longer blades with a variable coning hinge was shown to increase power production by 12% without significantly affecting ultimate loads or fatigue damage. Load-alignment has been shown to be an effective way to decrease cost of wind energy, which may bring us one step closer to a more resource responsible world.

Chapter 1

Introduction

Extreme-scale wind turbines (rated powers greater than 10 MW) have large capture areas but immense structural loads that can impede the reduction of levelized cost of wind energy. Chapter 2 shows that load-alignment, through active downwind coning, can reduce/eliminate flapwise bending loads by balancing the transverse components of thrust and centrifugal force. For a 13.2 MW scale with 100-meter-level wind turbine blades, it is found that a load-alignment coning schedule can substantially reduce the root flapwise bending moments. This moment reduction allows the rotor mass to be decreased by 26.8%, when compared with a conventional upwind three-bladed rotor, while maintaining structural performance and annual energy output.

Downwind two-bladed rotor configurations can have advantages in reducing rotor mass for wind turbines, compared with three-bladed upwind designs. However, the tower shadow adds an aerodynamic complication that can be difficult to quantify and predict. Chapter 3 presents and analyzes a previously unpublished subset of data collected during an extensive wind tunnel campaign, the Unsteady Aerodynamic Experiment (UAE). At high tip speed ratios, the tower shadow is a dominating contributor to bending moment oscillations but can be mitigated by the use of a tower fairing when such a fairing is aligned with the flow. At lower tip speed ratios where the blades can undergo aerodynamic stall and hysteresis, tower shadow was only a secondary contributor to bending moments and the tower fairing did not significantly impact bending moments. The aeroelastic simulation code called FAST was used to predict the same experimental conditions. In general, simulations reasonably predicted most of the cycle-averaged aspects, but only qualitatively predicted the unsteady variations due to tower shadow. To improve simulation predictions inside the tower wake, it is suggested that future work model the unsteady wake component associated with cylinder shedding and to consider a wake model for tower fairings at various wind incidence angles.

As wind turbine size increases so does the interest in the downwind rotor configuration, since they can provide a structural advantage for blade loads as compared to an upwind design. However, tower shadow, the blades passing through the tower wake, has long been a concern for downwind systems. The tower shadow negatively affects the blade by introducing a load impulse during the wake passage. An aerodynamic fairing could shroud the tower reducing the wake deficit and thus the load fluctuation effect of the tower shadow. However, there is no clear consensus on the importance of a tower shadow and of a fairing for large utility-scale wind turbines. Chapter 4 shows FAST simulations to quantify the effect of tower shadow for a 13.2 MW downwind turbine. Two cases were analyzed: steady wind conditions (e.g. wind tunnel experiment) and turbulent wind conditions (e.g. operating conditions). Under steady wind conditions, the tower shadow had a significant effect on predicted blade loads, increasing the Damage Equivalent Loading (DEL) by 70%. In this case, a tower fairing can reduce this impact by more than 75%. However, conditions with atmospheric turbulence were much less sensitive to tower shadow, and the predicted DEL decrease with a tower fairing was only 3%. These results indicate that a tower fairing can be important for low turbulence (e.g. wind tunnel) testing conditions but that an extreme-scale downwind turbine in field turbulence does not suffer significantly from tower shadow and does not benefit significantly from a tower fairing. Instead, the highest unsteady load fluctuations are due to atmospheric turbulence.

Load-alignment, balancing the thrust moment with the centrifugal moment, is a promising innovation for extreme-scale wind turbines. Load-alignment can allow for longer blades, facilitating an increase in power capture, while maintaining similar blade loads. As blades lengthen, larger coning angles are required to balance increasing thrust loads with centrifugal loads. This yields a key question for such extreme-scale load-aligned rotors: should the blades be hinged to actively vary coning or simply pre-aligned at a fixed coning angle? Chapter 5 answers this using FAST simulations conducted on a variety of rotors with different blade lengths and coning angles. The longest rotor without a hinge was shown to increase the energy production by 13.4% without an increase in peak blade loads. However, in turbulent wind there was an approximately 100% increase in damage equivalent load. When the coning angle was allowed to change slowly as a function of wind speed (by means of a morphing hinge), the power increase grew to 19% and the peak loads again increased under turbulent wind conditions, but only by 40%. Inclusion of teeter with the hinge decreased the peak flapwise moments and the fatigue damage back to near baseline values while maintaining 12% power production increase, as compared with the baseline rotor. The results show that load-alignment can be achieved with a fixed coning angle (pre-alignment) or by a morphing hinge. A morphing hinge allows for up to a 4.6% power increase compared to a fixed coning angle, and is structurally reasonable for rotors that already include a teeter hinge, which itself led to significant load reduction for large rotor blades.

Extreme-scale wind turbines have grown in popularity over the last decade. Load-alignment is an effective concept to lower average loads allowing for longer blades with larger than before possible rated powers. The first gravo-aeroelastically-scaled, experiment of an extreme-scale wind turbine is underway. This unique experiment requires unique methods to analyze the data. With load-alignment an area of interest it is necessary to separate the out-of-plane bending loads into their fundamental components (thrust, centrifugal and gravitational). The data analysis approach developed herein allows the measured resultant moment at a fixed coning angle to be decomposed into the fundamental components, and uses these components to estimate the resultant bending load the rotor would have experienced at a variety coning angles. The methodology was demonstrated using simulated data. The results show that a coning angle of 12.5° (testing conditions) results in a bending load that is 75% less than the load would have been without coning, and that a coning angle of 15° would result in near-zero average bending load over all wind speeds.

Chapter 2

Extreme-Scale Actively-Coned Rotors with Full- and Partial Load-Alignment

Abstract

Extreme-scale wind turbines (rated powers greater than 10 MW) have large capture areas but immense structural loads that can impede the reduction of levelized cost of wind energy. This analytical study shows that load-alignment, through active downwind coning, can reduce/eliminate flapwise bending loads by balancing the transverse components of thrust and centrifugal force. For a 13.2 MW scale with 100-meter-level wind turbine blades, it is found that a load-alignment coning schedule can substantially reduce the root flapwise bending moments. This moment reduction allows the rotor mass to be decreased by 26.8%, when compared with a conventional upwind three-bladed rotor, while maintaining structural performance and annual energy output.

Nomenclature

F	Force acting on the blade
m	Mass
M	Root flapwise bending moment
P	Generator power
r	Coordinate in the radial direction from the center of rotation
R	Tip radius
R_h	Hub radius
s	Coordinate from the blade root in the direction of the blade tip
S	Blade length
t	Coordinate from the blade root in the transverse direction
U_∞	Free stream wind velocity
x	Coordinate from the center of rotation in the free stream wind direction
y	Coordinate from the center of rotation in the direction defined by $\boldsymbol{e_y} = \boldsymbol{e_z} \times \boldsymbol{e_x}$
z	Coordinate from the center of rotation in the vertical direction
β	Coning angle
β_0	Coning angle resulting an average root flapwise bending moment of zero
$\beta_{2/3}$	Coning angle which reduces average root flapwise bending moment to 2/3 of original
τ	Shaft tilt angle
ψ	Azimuth angle ($\psi = 0°$ when the blade points up)
ω	Rotational rate of the rotor
$(\ )_C$	Component from centrifugal force
$(\ )_c$	Conventional value (from simulation)
$(\ )_G$	Component from gravity
$(\ )_T$	Component from thrust
$[\ ]'$	Distributed along the span of the blade

1. Extreme-Scale, Load-Aligned Wind Turbines

Wind turbine size is a primary factor determining a wind turbine's energy production. Larger turbines have larger swept areas and reach higher into the atmosphere, accessing stronger and more consistent winds due to reduced effect of the boundary layer which can increase their net power (Loth *et al.* 2017). This has led many to view extreme-scale wind turbines (rated power exceeding 10 MW) as an effective way to lower LCOE. For example, the European UpWind project predicted that 20 MW (252 m rotor diameter) wind turbines might be possible for off shore conditions (Peeringa *et al.* 2011). General Electric (GE Renewable Energy, 2018) has released plans to build a 12MW off-shore wind turbine with a rotor radius (R) of 110m. However, any increase in annual energy production (AEP) should be ideally larger than the corresponding increase in capital and operational expense (CAPEX and OPEX) so that there is a net decrease of levelized cost of energy (LCOE) for the system (Reiso & Muskulus, 2013). Since, some portion of CAPEX and OPEX scales with rotor mass, it is important to limit the increases in rotor mass that occur as rotor sizes increase.

Wind turbine blade mass[1] typically scales with $R^{2.2}$, which is consistent with the 13.2 MW turbine designed by Sandia National Labs (Griffith & Richards, 2014). However, at extreme-scale, downwind and gravitational forces (and moments) are no longer small relative to centrifugal forces and moments. Extreme-scale upwind turbines thus require strength and stiffness requirements to ensure the gravitational loads do not lead to excessive dynamics loading and that the downwind bending loads do not cause a blade-tower strike. As a result, the structural loads on extreme-scale turbine blades with a conventional upwind rotor become difficult to manage (Zhang *et al.* 2016). Additionally, a large rotor mass increases structural requirements for the nacelle, shaft, bearings, tower, and support structure (Fingersh *et al.* 2006). For these reasons, the extreme blade loads have impeded the growth of wind turbine size. To allow for lower cost extreme-scale turbines, innovations are needed to reduce blade-bending loads, reduce the requirements on tower strike, and reduce the rotor mass (and thus gravity loads).

Load-alignment with a downwind rotor is a proposed solution to decrease the root flapwise bending loads, reduce tower strike requirements, and potentially reduce the overall rotor mass. In particular, the load-alignment concept involves finding a balance between the downwind thrust loads and the radial centrifugal loads in an attempt to align the longitudinal axis with the resultant load (Crawford, 2008; Ning & Petch 2016; Noyes *et al.* 2018). The resultant load for a downwind coned rotor is shown in Fig. 1 in the turbine reference frame. The integrated transverse force components and their respective moment arms lead to root flapwise bending moments that must be structurally supported but are unused for power generation. These loads are a function of coning angle. Load-alignment eliminates the flapwise bending load by setting the coning angle such that the contributions from the centrifugal and thrust loads cancel out. This can only be done when coning is in the direction of the wind as in the case of a downwind rotor so the centrifugal component is upwind and opposite to the downwind thrust component. Because gravity is cyclic (the transverse component is a function of azimuth angle) only the average bending moment over one revolution is instead considered i.e. the combination of thrust and centrifugal components.

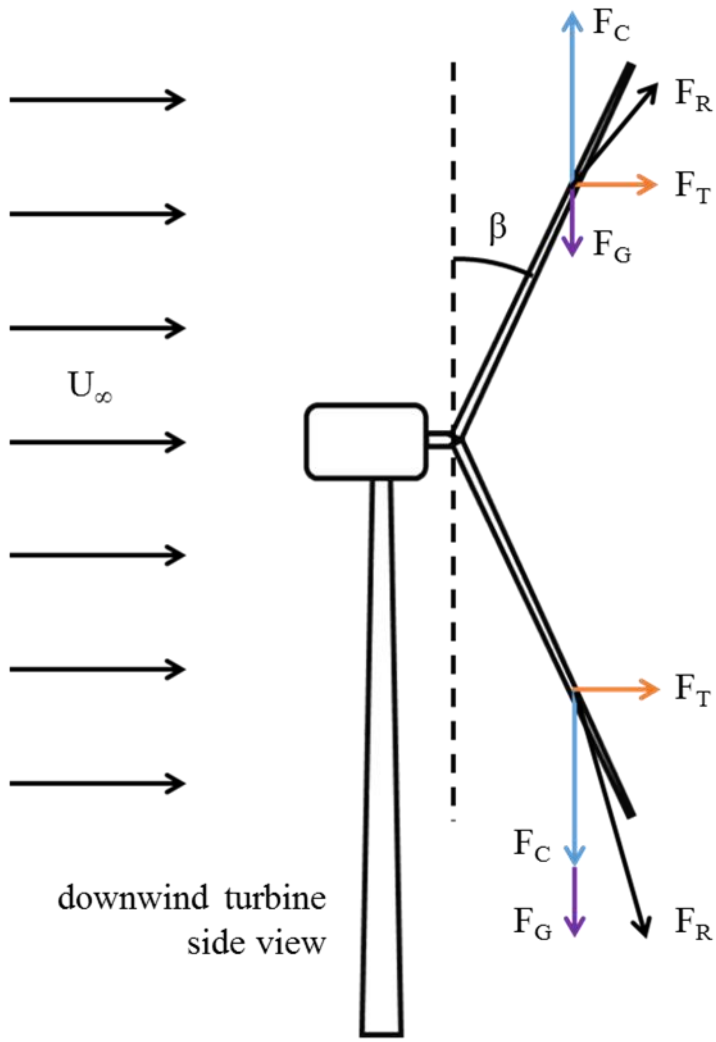

Figure 1. Downwind rotor shown from side-view in turbine reference frame indicating centrifugal, thrust and gravity forces summed into resultant force at a particular spanwise location

Because both the centrifugal and thrust loads are a function of wind speed, the load-aligned coning angle is also a function of wind speed. The downwind load-alignment concept can be applied in two ways: 1) setting a fixed pre-cone angle to achieve load-alignment at one specified condition (pre-aligned) and partial-alignment at other conditions via aeroelastic deflection, and 2) actively by changing the coning angle as a function of wind speed in order to achieve full-load alignment at a variety of conditions, by means of a hinge. The pre-aligned method is simpler to implement as it reduces the need for an additional actuator, hinge and controller. However, the active coning method can reduce the flapwise bending moment over a larger range of wind speeds at and above rated (where loads tend to be highest) but can be scheduled to minimize coning at lower wind speeds (where the loads are relatively lower) to maximize power capture. While these aeroelastic and active strategies for coning to morph the rotor have been conceptually studied (Noyes *et al.* 2017; Ichter *et al.* 2016), a detailed theoretical analysis of the load-alignment has not yet been presented. Such an analysis is needed to quantitatively characterize and optimize the performance of such rotors.

There are three primary objectives of this chapter, none of which have been studied previously based on authors' knowledge. The first is to develop an analytical framework that defines the moments on a downwind load-aligned rotor and their relationship to coning angle for a three-bladed system. The second is to analyze a 13.2 MW wind turbine to quantify the amount of coning needed to achieve a specified degree of load-reduction (including both full partial load-alignment). The third objective is to demonstrate the advantages of active coning by directly comparing a 13.2 MW turbine with a conventional turbine design (three-bladed and upwind rotor) into a load-aligned two-bladed, downwind turbine with an active coning hinge. The conventional turbine and load-aligned turbine have the same tower, drive train and 13.2 MW generator, and will be compared in terms of rotor mass, structural loads, and generated power.

2. Analytical Relationships Between Loads and Coning

The objective of this section is to develop the analytical relationships between the flapwise bending load (M) resulting from centrifugal force (F_C), thrust (F_T), and gravitational force (F_G) at a given coning angle (β). For simplicity, the effects of hub radius and shaft tilt are ignored in this analysis, since they are relatively small values with weak impact on the results presented herein. For completeness, the derivations with the inclusion of hub radius and shaft tilt are shown in the appendix.

To determine the geometric load relationships, it is important to establish the detailed reference frames. Figure 2 shows a schematic of the azimuthal and side views, both for an upwind and a downwind turbine. The azimuthal angle (ψ) is defined in the y-z plane as shown by Fig. 2a, with a reference value of ψ=0° when the blade points directly upward and increases counter clockwise about the positive x-axis. As shown in Fig. 2b, the coning angle is defined as a counter clockwise rotation about the positive y-axis, resulting in a negative value for upwind rotors. The negative coning angle for the upwind conventional turbine will be defined as β_c. The incoming wind flows in the positive x direction, while the coordinates s and r rotate with the blade. Note the spanwise coordinate ranges as $0 \leq s \leq S$, where S is the blade length, while radial coordinate ranges as $0 \leq r \leq R$, where R is the tip radius. The coordinate s is coned out or the rotor plane to follow the blade, while r stays inside the rotor plane such that $r = s\cos(\beta)$. The three loads that lead to flapwise bending moments for a coned rotor (shown in Fig. 2d) are thrust, centrifugal and gravitational.

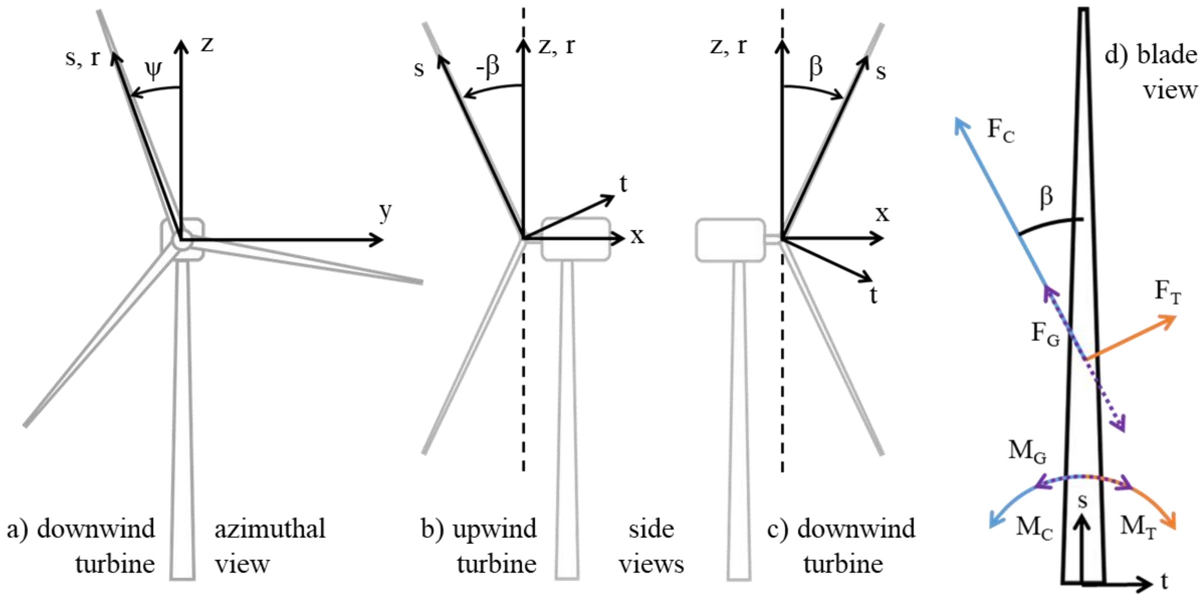

Figure 2. Schematic of an extreme-scale 3-bladed wind turbine where wind flows in the positive x direction, radial position (r), spanwise position (s), transverse direction (t), coning angle (β), azimuthal angle (ψ): (a) azimuthal view, blade points up at ψ=0°, (b) side view of upwind rotor, (c) side view of downwind rotor and (d) downwind coned rotor blade with centrifugal, thrust and gravitational loads and root moments shown.

The centrifugal force (F_C) acts in the radial direction and is a function of rotational rate (ω), mass (m), and radial distance (r). The centrifugal force for a point mass in a rotating reference frame is given by Eq. 1a. This result can be used to determine the differential force associated with a differential mass distributed along the blade span (Eq. 1b). To rewrite the force per unit span, we employ the prime notation for a general variable q as $q' \equiv \frac{\delta q}{\delta s}$. By dividing both sides by the differential spanwise element, $\delta s = \delta r/\cos(\beta)$, the centrifugal force per unit blade span (F_C') can be related to the distributed mass per unit blade span (m') as shown by Eq. 1c. The component of the differential centrifugal force in the transverse direction ($F_{C,t}'$) can then be obtained by taking the projection of Eq. 1c onto the transverse axis to yield the result of Eq. 1d.

$$F_C = \omega^2\, m\, r \tag{1a}$$
$$\delta F_C = \omega^2\, \delta m\, r \tag{1b}$$
$$\boldsymbol{F_C'} = \omega^2\, m'\, s \cos(\beta)\, \boldsymbol{e_r} \tag{1c}$$
$$\boldsymbol{F_{C,t}'} = -\,\omega^2\, m' s \cos(\beta) \sin(\beta)\, \boldsymbol{e_t} \tag{1d}$$

A similar differential spanwise decomposition can be used for the gravitational force, which is defined in terms of a point mass and the acceleration due to gravity (g) as shown in Eq. 2a. The previously applied process of assuming differential force and mass leads to Eq. 2b. Taking the component in the radial direction and then the transverse direction leads to Eq. 2c and 2d respectively. The cos(ψ) term causes the gravitational component to average to zero over one revolution.

$$F_G = m\, g \quad (2a)$$
$$\boldsymbol{F'_G} = -\, m'\, g\, \boldsymbol{e_z} \quad (2b)$$
$$\boldsymbol{F'_{G,r}} = -\, m'\, g \cos(\psi)\, \boldsymbol{e_r} \quad (2c)$$
$$\boldsymbol{F'_{G,t}} = m'\, g \cos(\psi) \sin(\beta)\, \boldsymbol{e_t} \quad (2d)$$

The thrust force cannot be modeled as simply since it involves a more complex distribution related to highly-coupled three-dimensional aerodynamic flow field behavior. As such, herein a baseline distribution is obtained using the simulation tool Aerodyn (Jonkman *et al.* 2015) for the conventional turbine coning angle (β_c) of an upwind system. The differential thrust distribution for this conventional configuration ($F'_{T,c}$) is given in Eq. 3a. A more general relationship can be developed for thrust force at any coning angle by employing blade element momentum theory (Mikkelsen *et al.* 2001), by assuming the thrust from a differential blade element is proportional to the differential area through which the element sweeps (Eq. 3b). This relationship is found to be reasonable (within 2%) for coning angles as high as 30°. In this case, the thrust distribution at any coning angle is given by Eq. 3c. Since $\cos^2(\beta_c) \sim 1$, the relationship becomes Eq. 3d. Finally, the important value for load-alignment is the transverse component, shown in Eq. 3e.

$$\boldsymbol{F'_{T,c}} = F'_{T,c}\, \boldsymbol{e_x} \quad (3a)$$
$$\frac{\delta F_T}{\delta A} = \frac{dF_T}{2\,\pi\, r\, dr} = \frac{1}{2\,\pi\, s \cos(\beta)} \frac{dF_T}{ds} \frac{ds}{dr} = \frac{1}{2\,\pi\, s \cos^2(\beta)} F'_T \quad (3b)$$
$$F'_T(\beta) = F'_T(\beta_c) \frac{cos^2(\beta)}{\cos^2(\beta_c)} \quad (3c)$$
$$F'_T = F'_{T,c}\, cos^2(\beta) \quad (3d)$$
$$\boldsymbol{F'_{T,t}} = F'_{T,c} \cos^3(\beta)\, \boldsymbol{e_t} \quad (3e)$$

With all three transverse load relationships developed, the root flapwise bending moments (M_R) for each of the forces angle can be obtained noting that the moment arm is the coordinate s and that these are the moments about the y-axis. The components of M_R are shown in the Eq. 4 a-c, and the resultant flapwise moment is shown in Eq. 4d. Nothing inside the square brackets of Eqs. 4a-4c changes as a function of β, therefore these three bracketed terms are replaced with load-alignment constants (K) for simplicity in Eq. 4d, such that the azimuthally-averaged M_R can be expressed as a trigonometric function of β for a given rotational rate (ω).

$$M_C = \int_0^S -\,\omega^2\, m' s^2 \cos(\beta) \sin(\beta)\, ds = -\left[\omega^2 \int_0^S m' s^2 ds\right] \cos(\beta) \sin(\beta) \quad (4a)$$
$$M_G = \int_0^S m'\, g \cos(\psi) \sin(\beta)\;\, s\, ds = \left[g\;\cos(\psi) \int_0^S m'\, s\, ds\right] \sin(\beta) \quad (4b)$$
$$M_T = \int_0^S F'_{T,c} \cos^3(\beta)\, s\, ds = \left[\int_0^S F'_{T,c}\, s\, ds\right] \cos^3(\beta) \quad (4c)$$
$$M_R = -K_C \cos(\beta) \sin(\beta) + K_G \sin(\beta) + K_T \cos^3(\beta) \quad (4d)$$

This relationship between coning angle and the resultant moment in Eq. 4d is useful for selecting a coning angle to reduce the load by any specified amount. For instance, the load-aligned angle (β_0) is defined as the coning angle that results in no azimuthally-averaged root flapwise bending moment (M_R=0 at ψ=90°). The coning required for a partial load reduction (relative to the conventional coning angle) can be solved from Eq. 4d. In particular, the coning angle where the load is reduced to 2/3 of the upwind case (M_R = 2/3 $M_{R,c}$) is defined as $\beta_{2/3}$. This partial-alignment case will be shown to have important characteristics as discussed in the following section.

In order to obtain β_0 and $\beta_{2/3}$ for various wind speeds (U_∞), we note that a constant tip speed ratio below rated conditions indicates ω varies linearly with U_∞, leading to a change in K_C. As wind speed changes, so does the thrust force distribution causing a change in K_T, which thus must be recalculated at every wind speed of interest. If aero elastic deflections are neglected for the purpose of determining β_0 and $\beta_{2/3}$, the wind speed does not affect K_G.

3. Relationships Applied to a 13.2 MW Wind Turbine

The 13.2 MW extreme-scale upwind turbine design by Sandia National Lab (SNL) was chosen as the conventional design baseline for the analysis. This three-bladed turbine design was originally scaled up from NREL's 5 MW reference turbine (Jonkman *et al.* 2009) to design a series of 100 m blades, denoted SNL100-0x (Griffith & Richards, 2014). The lightest and most advanced blade of that series, SNL100-03, was chosen for the present analysis as the conventional baseline (Table 1). Although the turbine has a non-zero value for shaft tilt as shown in the table, the tilt herein was be set to zero during the analysis to prevent additional complexity and since its inclusion affects the results by less than 5% in terms of root flapwise bending load.

Table 1. Turbine properties for SNL100-03 blade

Rotor configuration	Upwind three-bladed
Rated power	13.2 MW
Rated wind speed (U_{rated})	11.3 m/s
Optimal tip speed ratio	9.66
Rated rotor speed	7.46 rpm
Blade length (S)	100 m
Blade mass	49,500 kg
Coning angle (β)	-2.5°
Hub Radius (R_h)	2.5 m
Shaft tilt (τ)	-5° (0° used)

Aerodyn v15 has been shown to be reasonably robust in predicting aerodynamic performance for a variety of rotors and operating conditions (Jonkman *et al.* 2015). This simulation tool was used herein to calculate distributed thrust force ($F'_{T,c}$) for steady wind speeds ranging from cut-in to cut-out for the turbine of Table 1. For this simulation, the blade was segmented into 18 elements. Nine of the elements (roughly evenly spaced) were used as output channels. Rotational speed and blade pitch were set for each wind speed based on the SNL100-03 blade analysis (Griffith & Richards, 2014).

Based on this simulation, the magnitude of the forces per unit span (Eq. 1c, 2b & 3d) acting on the SNL100-03 turbine blade at steady rated conditions (U_{rated} = 11.3 m/s) are shown in Fig. 3a as a function of blade span. Over the majority of the span (15%-90%), the centrifugal force is the largest force acting on the blade. Through decomposition (Eq. 1d, 2d & 3e), the transverse component of the forces (related to blade flapwise bending) are shown in Fig. 3b. The thrust load is the largest contributor to the transverse component of the resultant load. All the other loads have little effect on bending because the coning angle is relatively low (β = -2.5°). Rotors with higher coning angles will be shown to have larger contributions from centrifugal and gravitational loads.

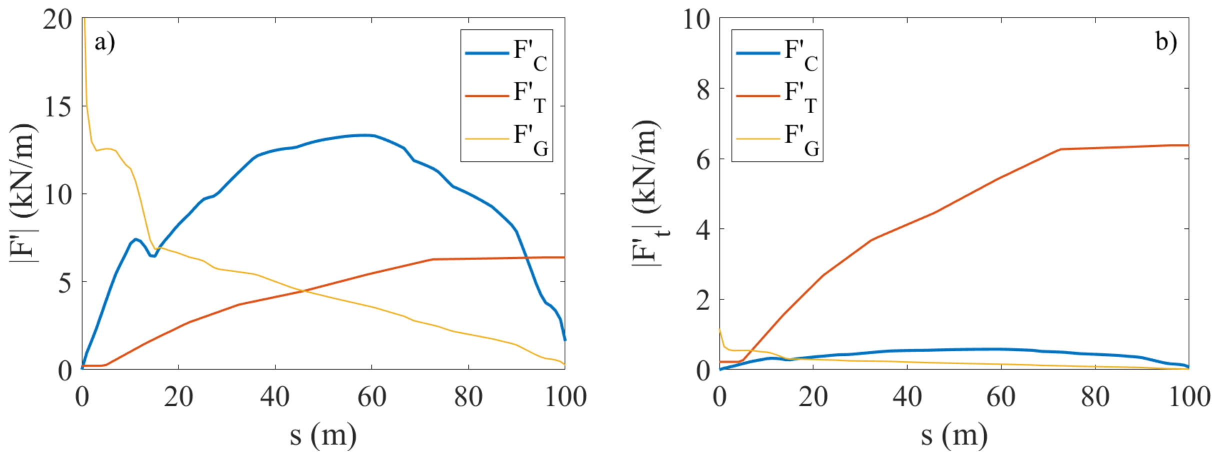

Figure 3. Spanwise distribution of the centrifugal, thrust, and gravity forces per unit span on the SNL100-03 rotor blade at rated conditions (U_{rated} = 11.3 m/s) as function of blade span: (a) total force magnitude (b) magnitude of transverse component.

Load-alignment concepts focus changing the coning angle such that the average bending load is decreased or eliminated. The relationship between bending moment and coning angle can be modeled with Eq. 4d. Two of the load-alignment constants (K_C & K_T) are functions of wind speed as shown in Fig. 4a. The relative significance of thrust on bending increases from cut-in to rated wind speed, and then decreases until cut-out. The relative significance of centrifugal force increases as the rotor speeds up and plateaus at constant rotational rate. Figure 4b shows the resultant moment as a function of coning angle at three wind speeds (rated, half-rated & twice-rated). The shaded portion represents the range of moment values including the oscillatory gravitational component. As coning increases, the average load decreases because the centrifugal contribution in the transverse direction of the blade is relatively higher. The gravitational contribution is also higher which increases the range of values. The oscillatory load due to gravity can be mitigated by means of teeter for two-bladed wind turbines. Complete load-alignment results when there is zero azimuthal average root flapwise bending moment (M_R=0). The coning angle that results in this load-alignment (where the solid line passes through the x-axis) is defined as the load-aligned angle (β_0) and is a function of wind speed.

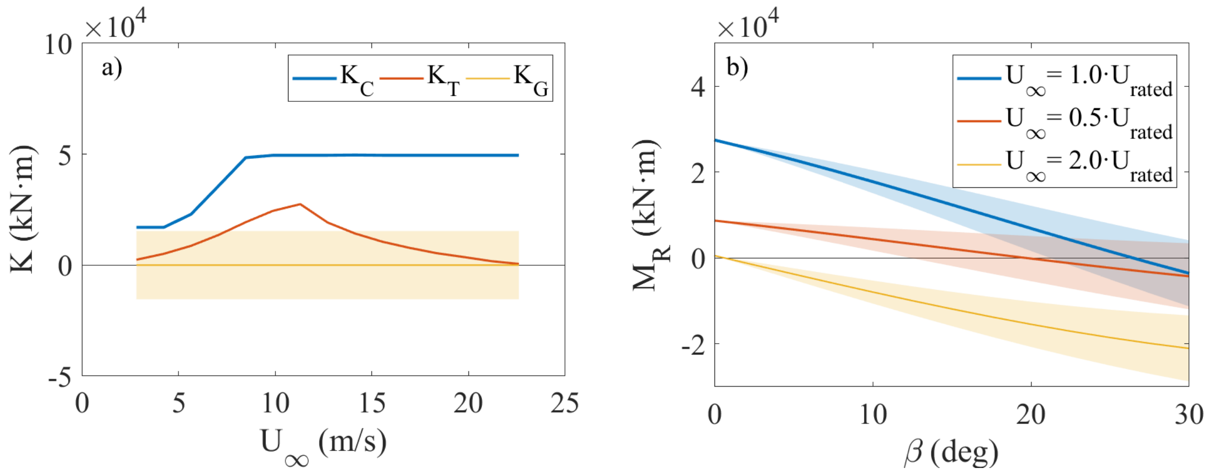

Figure 4. Relationship between root flapwise bending load and coning angle (a) load-alignment constants for centrifugal, thrust and the range of gravity loads as a function of wind speed and (b) root flapwise bending load as a function of coning angle for three different wind speeds. The shaded region shows the range of values due to gravity whereas the solid lines shows the azimuthally-averaged values.

The load-aligned angle can often require relatively large coning angles, which comes with drawbacks: less power due to decease in swept area and increased oscillatory loads due to gravity. As such, it may not be optimal to achieve complete load-alignment and instead a partial load-alignment may be a reasonable strategy. Partial load-alignment may decrease the structural loads of the blade such that the blade can be designed less expensively. Adapting a 3-blade rotor to a 2-bladed rotor results in the average flapwise and torque-wise bending moments increasing by roughly 50% per blade. Since the flapwise bending moment is generally much larger, a sensible load reduction strategy is to only increase coning until the average bending load is reduced to 67% of the conventional moment. This would lower the loads sufficiently that an adapted 2-bladed, coned turbine with similar structural stiffens and mass per blade would have roughly the same average bending load per blade. As a result, the two-bladed rotor would have about 2/3 the rotor mass compared to the conventional rotor. This strategy allows direct cost savings, in the form of rotor capital expense, without requiring a significant structural blade redesign.

As noted before, one strategy may be to fix the coning angle based on load-alignment for all wind speeds. Such a schedule may not be ideal for power capture, but is a helpful baseline in understanding the relationship between load-alignment angles and mean wind speed operating conditions. Figure 5a, shows the load-alignment angle (β_0), partial load-alignment angle ($\beta_{2/3}$) and the conventional coning angle (β_c=-2.5°) from cut-in, to cut-out. It can be seen that these angles β_0 and $\beta_{2/3}$ reach their highest values (β_0=26.4°, $\beta_{2/3}$=8.1°) at rated conditions where K_T is the highest. Notably, the partial load-alignment strategy allows much more manageable coning angles than the complete load-alignment strategy. Figure 5b shows the root flapwise bending load resulting from the three coning angle schedules. As expected, conventional coning (β_c) results in the largest moments. The complete load-aligned schedule, results in zero average load (by design) but results in the largest load-range (shaded region). The partial load-alignment strategy results in a load that is 67% as large as the initial load (by design) and has relatively minimal oscillatory loads as compared to the load-aligned case. This can be beneficial since structural mass generally increases with both the mean load increases and when the oscillating loads about this mean also increase[16]. These results show that moderate downwind coning (5°-25°) can have large reductions in average bending loads and that this reduction is roughly proportional to the difference between the conventional and fully-aligned coned angles, i.e. M_R tends to scale with $(\beta-\beta_0)/(\beta_c-\beta_0)$. However, there is concomitant increase in gravitational cycling loads as the coned angle approaches β_0. It should be noted that the partially-aligned conditions with $\beta_{2/3}$, will have lower coning angles below rated such that it can have greater power capture as compared to the case with β_0.

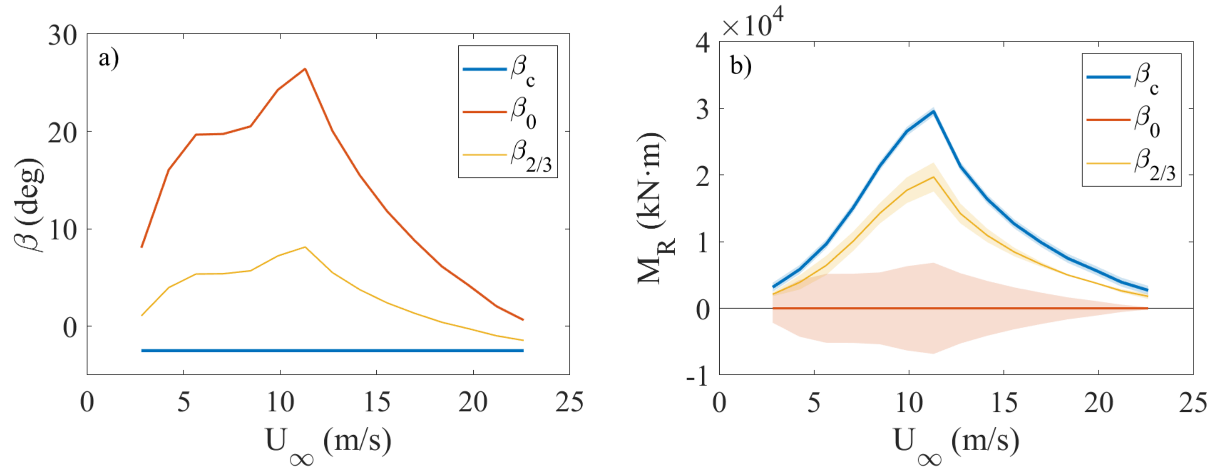

Figure 5. Complete and partial load-alignment for the SNL100-03 rotor (a) coning angle schedule as a function of wind speed & (b) root flapwise bending load under different coning schedules, shaded region represent range of values for different azimuthal positions.

Another strategy, as discussed in section 1, compared with the actively-coning strategy, is the pre-aligned method (Noyes *et al.* 2018; Qin *et al.* 2016), which avoids the need for a hinge and actuator. A fixed coning angle can minimize bending loads for a single wind speed, but will be less optimal away from that design condition. A pre-aligned system could be effective at reducing peak loads but will not generate as much power below rated conditions compared with a hinged system. A dynamically actuated coning system could allow for more aggressive coning ($\sim\beta_{2/3}$) near rated when loads are high, and less aggressive coning ($\sim\beta_c$) when loads are lower and power is more important, this allows for a sensible balance between maximizing power and minimizing loads. Further investigation can focus on whether the increased power generation from a hinge offsets the increased costs due to additional components and complexity.

4. Simulation of Actively Coned, Load-Aligned Wind Turbine

The analytical relationships developed in the previous sections provide important insight on the behavior of load-aligned rotors. However, these relationships are simplified first-order approximations. To quantify the benefits of load-alignment under more realistic conditions (e.g. turbulence), two rotors (one conventional and one load-aligned) will be compared using a wind turbine simulation tool. The two rotors compared are named CONR (CONventional Rotor) and SUMR (Segmented, Ultralight, Morphing Rotor) (Martin *et al.* 2017; Zalkind *et al.* 2017; Ananda *et al.* 2018). The rotor is deemed ultralight in that it uses at least 25% less mass compared with the state of the art conventional rotor (CONR). The segmentation portion of SUMR does not pertain to this investigation and is not discussed herein. The rotor is ultralight in that it uses 26.8% less mass compared with the state of the art conventional rotor (CONR). Morphing refers to the active coning system that allows the rotor to adjust the coning angle as a function of wind speed.

The morphing system allows for large coning angles when loads are greatest (near rated) and lower coning angles when power production is more important (below rated). General parameters for the two rotors are shown in Table 2.

Table 2. Turbine properties for CONR and SUMR

	CONR	**SUMR**
Rotor configuration	Rigid upwind three-bladed	Teetered downwind two-bladed
Rated power	13.2 MW	13.2 MW
Rated wind speed (U_{rated})	11.3 m/s	11.3 m/s
Rated rotor speed	7.29 rpm	8.96 rpm
Blade length (S)	100 m	110 m
Blade mass	49,500 kg	54,500 kg
Rotor mass	148,500 kg	108,900 kg
Precone angle (β)	-2.5°	2.5° to 12.5°
Shaft tilt (τ)	-5°	5°

In the present simulations, both rotors use the SNL100-03 blade. However, to preserve rated power, the SUMR blade is lengthened linearly by 10%. This is to compensate for decreased swept area from coning and decreased solidity from using only two blades. The spanwise local parameters (profile, thickness, chord, linear stiffness & linear mass density) were left unchanged. Therefore, the 10% increase in length results in a blade 110m long with mass of 54,500 kg (10% increase). The combination of the blade mass increase and the decrease in the number of blades, results in a rotor mass which is 26.8% less compared with the state of the art conventional rotor (CONR). It should be noted that this degree of linear lengthening has been employed previously (Noyes *et al.* 2018; Qin *et al.* 2016) and has been shown to be a reasonable replacement for a full re-design blade from a structural, aerodynamics and control point of view to within a few % of blade mass. As such, the lengthened blade is not optimized, but instead represents a simple and reasonable design for comparison purposes.

One note of caution in reducing the number of blades is the impact on dynamics. Two-bladed turbines have an unsteady gyroscopic effect that is not present for three-bladed turbines (Stol *et al.*, 2002). The To counter this load, SUMR uses a teetered axis, which is typical for two-bladed rotors. Teeter for two bladed rotors also reduces the oscillatory gravitational flapwise moment that results from increased coning.

Another note of caution is that the rotor solidity is reduced which will increase the rated tip speed ratio and decrease the rated power coefficient. Therefore, separate aerodynamic and power performance simulations were completed using FASTv8 (Jonkman & Buhl, 2005) for both rotors (CONR and SUMR). Simulations were run with turbulent wind, ranging in nominal wind speed (U_∞) from 2.83 m/s (25% U_{rated}) to 22.6 m/s (200% U_{rated}). TurbSim (Jonkman & Kilcher, 2012) was used to generate turbulent fields. Kaimal turbulence model was used with B turbulence intensity. The grid resolution was set to 25 x 25 with dimensions of 240m x 240m. The reference height was set to the hub height, which was 146.4m. This was in accordance with IEC Class IIb wind (Burton *et al.* 2011).

At each nominal wind speed, 12 simulations were conducted with different numerically generated turbulent wind fields. For each of these unsteady simulations, the time step was set at 0.0125 s and the simulations ran for 11 minutes for each wind speed. Only the last 10 minutes were used for data processing to exclude startup variations. Simulation averages of root flapwise bending moment (M) and generator power were reported.

MLife (Hayman Buhl, 2012) was used to calculate Damage Equivalent Loading (DEL) for root flapwise bending load, where DEL is defined as the amplitude of a zero mean, 1 Hz sinusoidal signal that would result in equivalent fatigue damage. MLife uses a rain flow counting algorithm to compute DEL. Short term DEL, calculated from each 10-minute simulation, were calculated and reported. Lifetime DEL, calculated using data from all the simulations, was also reported. Lifetime DEL requires an assumed lifetime of 20 years, and wind speed defined by a Weibull distribution with shape factor of 2 and scaling factor of 9.59 m/s. Using the same wind speed distribution, Annual Energy Production (AEP) was calculated and reported.

The present SUMR rotor utilizes an active coning schedule (changes as a function of wind speed) to reduce the average bending load over a wide range of turbulent wind speeds. The coning schedule, Fig. 6, is tailored to have little coning at below rated wind speeds to maintain high power production, and more aggressive coning near rated conditions to lower the loads. This was found to be a reasonable schedule due to its general effectiveness and relative simplicity. Note that coning actuation is assumed to be slow given the large rotational inertia of the rotor. The coning angle was fixed at a single value during each nominal wind speed simulation.

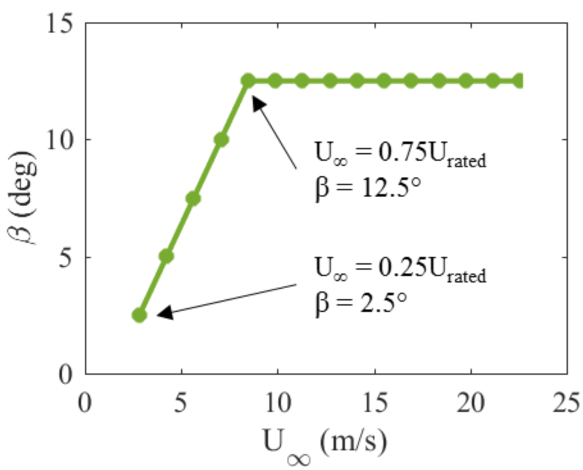

Figure 6. SUMR coning angle schedule designed to maximize power while maintaining similar root flapwise bending load (mean and DEL) compared with CONR.

An example turbulent wind field based on a nominal wind speed given by U_{rated} is shown in Fig 7a. The free stream component at the reference height is plotted versus time. The root flapwise bending loads resulting from the same wind field is shown in Fig 7b. The dotted line shows the instantaneous data, while the solid line represents the mean value. At this wind speed, the mean bending moment can be seen to be about 12% lower for SUMR than for CONR. This is notable because 2-bladed rotor on a conventional turbines (without the advantage of load-alignment) would be expected to have a larger bending moment (by roughly 50%) than the 3-bladed versions for similar power production. The fact that SUMR has a lower mean bending moment is due to the load-aligned concept.

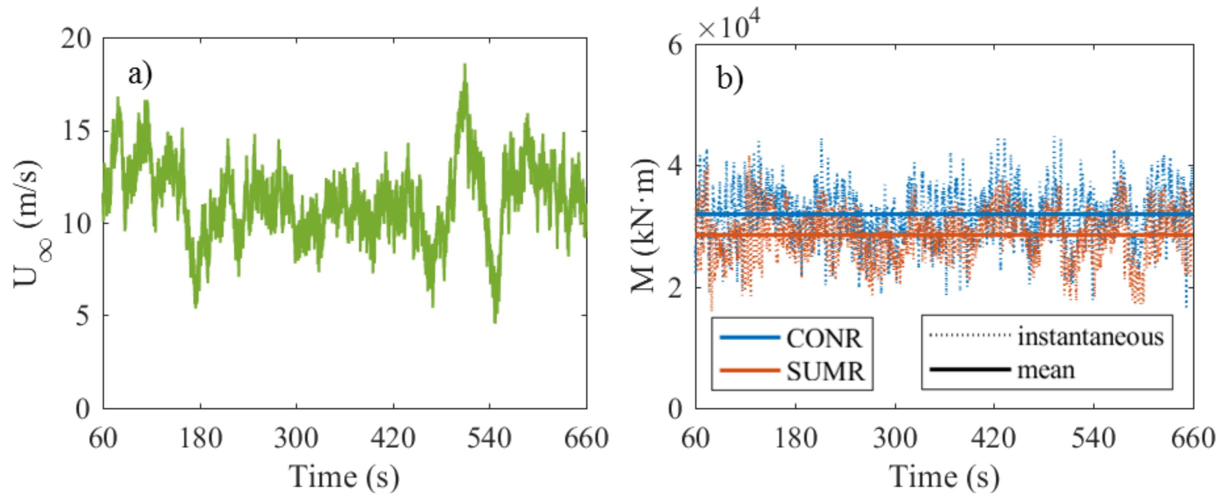

Figure 7. Simulation at rated wind speed: (a) streamwise component of turbulent wind at nominally rated wind speed (b) instantaneous root flapwise bending moment for CONR and SUMR.

Further illustrating the benefit of the load-aligned concept, Fig. 8a demonstrates the load reduction over the entire wind speed domain. Despite a much lower structural mass of the rotor, SUMR reduces the moment especially at high speeds. This mean bending load reduction is a good indicator of success. However, if increased gravitational bending and other unsteady loads caused higher load oscillations relative to the conventional case, then fatigue could be adversely impacted. Figure 8b shows the average of the short term DEL for each wind speed. The DEL for CONR and SUMR are similar but the SUMR DEL is even slightly lower. A similar result was obtained by comparing the lifetime DEL for each rotor calculated in MLIFE, which yielded 26,000 kN·m (SUMR) and 28,400 kN·m (CONR).

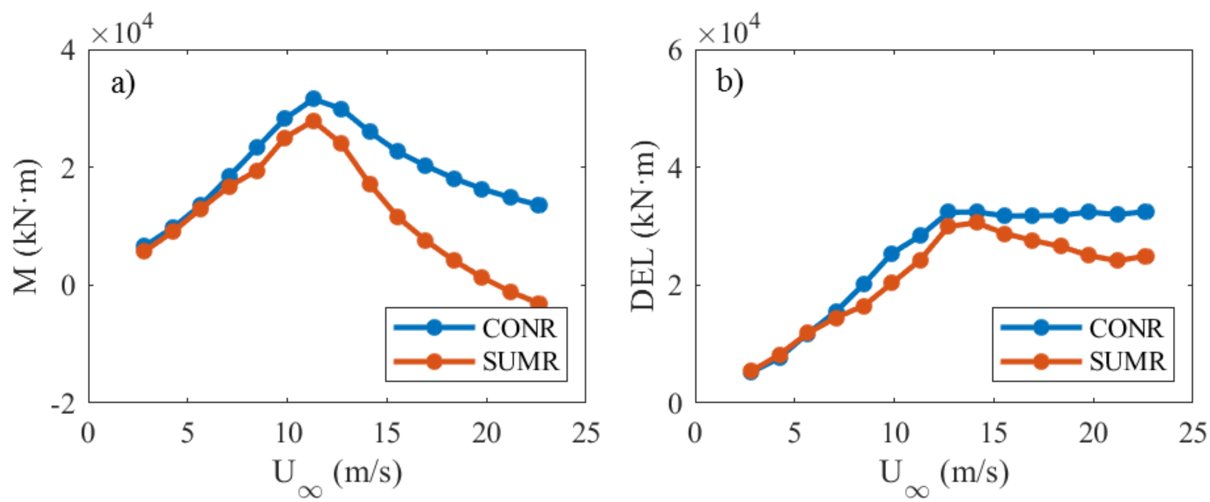

Figure 8. Response of CONR and SUMR over all turbulent wind speeds (a) mean root flapwise bending moment (b) mean short term DEL.

Finally, the Annual Energy Production was compared for the two rotors using the Weibull wind speed distribution. It was found that there was only a 0.5% reduction in annual energy production: 52,340 MW·hr/yr (CONR) to 52,060 MW·hr/yr (SUMR). The power loss while significant would have generally been larger for a fixed cone angle schedule, but the SUMR utilizes active coning to maximize capture areas at low wind speeds to increase AEP. This represents a clear measure of success of the load-alignment concept since it yielded a significantly lighter rotor while maintain the same (or less) damage equivalent loads and effectively the same similar annualized power output. The importance of the 26.8% rotor mass can be significant. This directly lowers capital expense of the rotor, but can also indirectly lower capital expense of other components: nacelle, shaft, tower, support etc. Another strategy could be to make the rotor mass the same as the conventional rotor so that the load-aligned rotor could have longer blades. This would allow greater energy capture at conditions below rated, thereby increasing the AEP that can be captured as compared to the conventional turbine (Ananda *et al. 2018*).

5. Conclusions

Load-alignment via downwind coning can significantly reduce root flapwise bending loads. The relationship between centrifugal, gravitational and thrust bending moments was simplified to a trigonometric function of coning angle. These relationships can be solved for a particular coning angle that eliminates (or reduces by a specified amount) the root flapwise bending load. Reducing bending loads can save the amount of blade mass necessary to meet structural requirements, leading to less expensive rotors. The relationships can be used in the rotor design stage or additionally as the base model for the control design for a hinged system.

Based on the analytical analysis developed in this chapter, for a three-bladed 13.2 MW turbine, downwind coning (~25°) can be used to eliminate the average bending loads at rated conditions. Less extreme coning angles (~8°) could be used to significantly reduce the loads (by 33%) such that the structural requirements can be met less expensively, with only minimal decrease in swept area (2% decrease).

The SUMR turbine implemented an active coning schedule to align the rotor blades closer with the resultant loads at high wind speeds, but at low wind speeds the rotor extends to capture more power. The SUMR turbine does not experience the typical load increase that would accompany a transition from 3-bladed to 2-bladed rotors because of leveraging the load-aligned concept. In fact, the two-bladed SUMR rotor significantly lowered the loads while producing similar power outputs.

There are several recommendations to improve the performance of the SUMR rotor. The aerodynamic profiles of the blades could be redesigned when moving from an upwind three-bladed design, to a downwind two-bladed design, with a higher tip speed ratio. With an aerodynamic redesign the rotor would likely produce more power. Because the aerodynamics were suboptimal, the blade was stretched to capture more wind, while the structural design of the blade was unchanged. With a structural redesign the rotor would likely become stronger with the use of less material. With a controller redesign, the rotor would likely experience less damage while producing more power. The SUMR rotor used in this study is only the first iteration; it supports the concept of using active coning for load-alignment and lays groundwork for rotor designs that can be significantly improved upon. Further investigations should determine if the increase in power justifies the increase cost and complexity of the hinged system. The load-alignment concept may be an efficient way to lower the cost of energy for future extreme-scale wind turbines.

Acknowledgments

The authors would like to thank ARPA-e for funding and guiding the research reported herein. The authors would like to thank members from the following institutions and labs for their assistance and guidance: University of Illinois, Urbana Champagne; University of Texas, Dallas; University of Colorado, Boulder; Colorado School of Mines; National Renewable Energy Laboratory.

Funding

Advanced Research Projects Agency – Energy: DE-AR0000667

References

Ananda, G. K., Bansal, S., & Selig, M. S. (2018). Aerodynamic Design of the 13.2 MW SUMR-13i Wind Turbine Rotor. In *2018 Wind Energy Symposium* (p. 0994).

Burton, T., Jenkins, N., Sharpe, D., & Bossanyi, E. (2011). *Wind energy handbook*. John Wiley & Sons.

Crawford, C. (2008). Parametric Variations of a Coning Rotor Wind Turbine. In *46th AIAA Aerospace Sciences Meeting and Exhibit* (p. 1340).

Fingersh, L. J., Hand, M. M., & Laxson, A. S. (2006). Wind turbine design cost and scaling model.

GE Renewable Energy. GE announces Haliade-X, the world's most powerful offshore wind turbine. Press Release. 2018 (https://www.genewsroom.com)

Griffith, D. T., & Richards, P. W. (2014). The snl100-03 blade: Design studies with flatback airfoils for the sandia 100-meter blade. *Sandia National Laboratory, SAND2014-18129*.

Hayman, G. J., & Buhl Jr, M. (2012). Mlife users guide for version 1.00. *National Renewable Energy Laboratory, Golden, CO*.

Ichter, B., Steele, A., Loth, E., Moriarty, P., & Selig, M. (2016). A morphing downwind-aligned rotor concept based on a 13-MW wind turbine. *Wind Energy*, *19*(4), 625-637.

Jonkman, J., Butterfield, S., Musial, W., & Scott, G. (2009). Definition of a 5-MW reference wind turbine for offshore system development. *National Renewable Energy Laboratory, Golden, CO, Technical Report No. NREL/TP-500-38060*.

Jonkman, J. B., & Kilcher, L. (2012). *TurbSim User's Guide: Version 1.06. 00, National Renewable Energy Laboratory*. Technical Report. Draft available at: https://wind. nrel. gov/designcodes/preprocessors/turbsim/TurbSim. pdf.

Jonkman, J. M., & Buhl Jr, M. L. (2005). FAST user's guide. *National Renewable Energy Laboratory, Golden, CO, Technical Report No. NREL/EL-500-38230*.

Jonkman, J. M., Hayman, G. J., Jonkman, B. J., Damiani, R. R., & Murray, R. E. (2015). AeroDyn v15 user's guide and theory Manual. *NREL: Golden, CO, USA*.

Loth, E., Steele, A., Qin, C., Ichter, B., Selig, M. S., & Moriarty, P. (2017). Downwind pre-aligned rotors for extreme-scale wind turbines. *Wind Energy*, *20*(7), 1241-1259.

Martin, D. P., Johnson, K. E., Zalkind, D. S., & Pao, L. Y. (2017, May). LPV-based torque control for an extreme-scale morphing wind turbine rotor. In *American Control Conference (ACC), 2017* (pp. 1383-1388). IEEE.

Mikkelsen, R., Sørensen, J. N., & Shen, W. Z. (2001). Modelling and analysis of the flow field around a coned rotor. *Wind Energy: An International Journal for Progress and Applications in Wind Power Conversion Technology*, *4*(3), 121-135.

Ning, A., & Petch, D. (2016). Integrated design of downwind land-based wind turbines using analytic gradients. *Wind Energy*, *19*(12), 2137-2152.

Noyes, C., Qin, C., & Loth, E. (2017). Low Mass, Morphing Rotor for Extreme Scale Wind Turbines. In *35th Wind Energy Symposium* (p. 0924).

Noyes, C., Qin, C., & Loth, E. (2018). Pre-aligned downwind rotor for a 13.2 MW wind turbine. *Renewable Energy*, *116*, 749-754.

Peeringa, J., Brood, R., Ceyhan, O., Engels, W., & De Winkel, G. (2011). UpWind 20MW Wind Turbine Pre-Design. *ECN, Paper No. ECN-E–11-017*.

Qin, C., Loth, E., Lee, S., & Moriarty, P. J. (2016). Blade Load Reduction for a 13 MW Downwind Pre-Aligned Rotor. In *34th Wind Energy Symposium* (p. 1264).

Reiso, M., & Muskulus, M. (2013). The simultaneous effect of a fairing tower and increased blade flexibility on a downwind mounted rotor. *Journal of Renewable and Sustainable Energy*, *5*(3), 033106.

Stol, K., Balas, M., & Bir, G. (2002). Floquet modal analysis of a teetered-rotor wind turbine. Journal of solar energy engineering, 124(4), 364-371.

Thomsen, K., & Sørensen, P. (1999). Fatigue loads for wind turbines operating in wakes. *Journal of Wind Engineering and Industrial Aerodynamics*, *80*(1-2), 121-136.

Zalkind, D. S., Pao, L. Y., Martin, D. P., & Johnson, K. E. (2017). Models used for the simulation and control of a segmented ultralight morphing rotor. *IFAC-PapersOnLine*, *50*(1), 4478-4483.

Zhang, M., Tan, B., & Xu, J. (2016). Smart fatigue load control on the large-scale wind turbine blades using different sensing signals. *Renewable Energy*, *87*, 111-119.

Appendix: General Analytical Relationships between Loads and Coning Angle

The equations developed in the chapter ignored hub radius (R_h) and shaft tilt (τ). If these values are small (which is often true) they only minimally effect the relationships. In this section the relationships will be derived including these parameters. Three reference frames are defined: inertial frame ($\boldsymbol{e_i}$), the rotor frame ($\boldsymbol{e_r}$) and the blade frame ($\boldsymbol{e_b}$). Each frame follows the right hand rule ($\boldsymbol{e_1} \times \boldsymbol{e_2} = \boldsymbol{e_3}$). The inertial and rotor frame are centered at point p_r, while the blade reference frame is offset by the hub radius and is centered at point p_b. Both the rotor frame and blade are tilted with respected to the inertial frame and rotate with the azimuth angle (ψ). The blade frame is coned (β) with respect to the rotor frame.

An arbitrary vector can be described in all three frames with three frame specific components (V_1, V_2, V_3), shown in Eq. A1a. The vector containing the three components can be rotated into any other frame using a 3x3 matrix (Q) shown in Eq. A1b. The translational portion of the transformation is not captured by the Q matrix and must be later accounted for. The rotor frame ($\boldsymbol{e_r}$) compared with inertial frame ($\boldsymbol{e_i}$) is first rotated by τ about $-\boldsymbol{e_{i,2}}$ and then rotated by ψ about $\boldsymbol{e_{i,1}}$. There is no translation between the two frames. The two frames can be related by Q_{ri} defined in Eq. A1c. The blade frame ($\boldsymbol{e_b}$) compared with the rotor frame ($\boldsymbol{e_r}$) is first translated in the $\boldsymbol{e_{r,3}}$ direction by R_h then rotated about the translated $\boldsymbol{e_{b,2}}$ axis. The two frames can be related by Q_{br} defined in Eq. A1d. A vector in the inertial frame can be expressed in the blade frame using Q_{bi} defined in Eq.A1e.

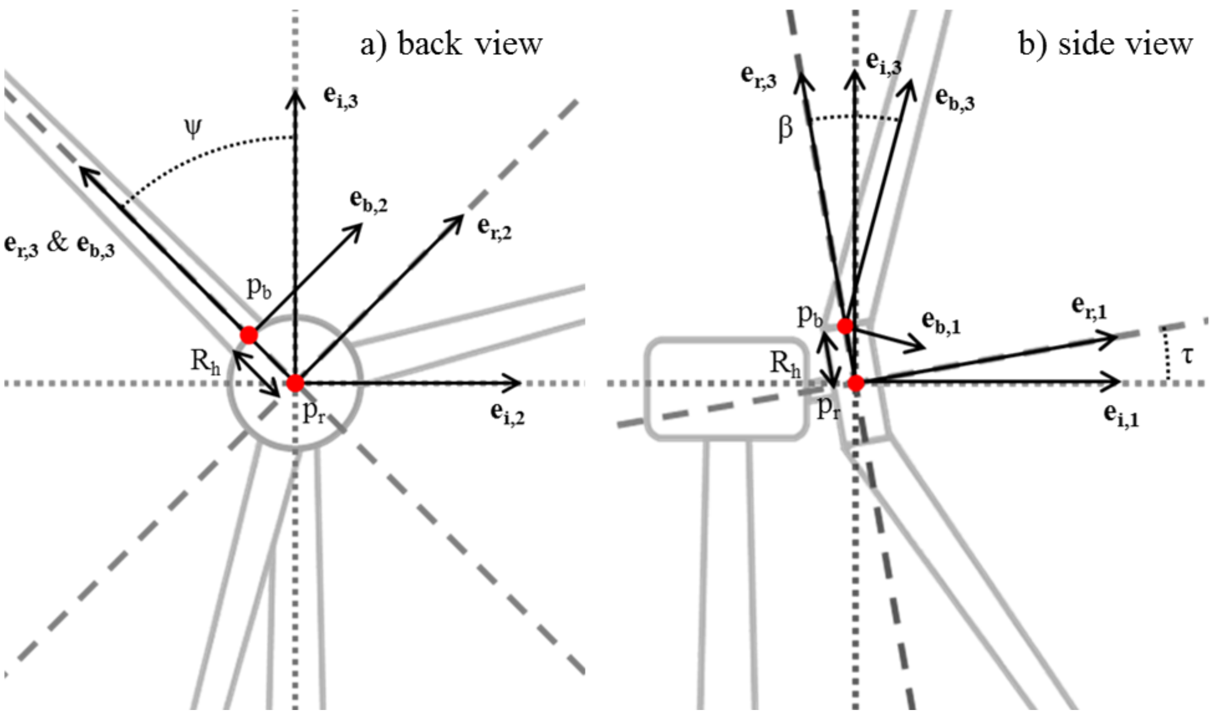

Fig. A1 schematic of an extreme-scale, 3-bladed, downwind turbine. Three reference frames, inertial (e_i), rotor (e_r) and blade (e_b).

$$\boldsymbol{V} = [V_{a,1}, V_{a,2}, V_{a,3}]\boldsymbol{e_a} = [V_{b,1}, V_{b,2}, V_{b,3}]\boldsymbol{e_b} \tag{A1a}$$
$$\boldsymbol{V_b} = \boldsymbol{Q_{ba}V_a} \tag{A1b}$$
$$Q_{ri} \equiv \begin{bmatrix} \cos(\tau) & 0 & \sin(\tau) \\ -\sin(\tau)\sin(\psi) & \cos(\psi) & \cos(\tau)\sin(\psi) \\ -\sin(\tau)\cos(\psi) & -\sin(\psi) & \cos(\tau)\cos(\psi) \end{bmatrix} \tag{A1c}$$
$$Q_{br} \equiv \begin{bmatrix} \cos(\beta) & 0 & -\sin(\beta) \\ 0 & 1 & 0 \\ \sin(\beta) & 0 & \cos(\beta) \end{bmatrix} \tag{A1d}$$
$$Q_{bi} \equiv Q_{br}Q_{ri} \tag{A1e}$$

Two useful coordinates are radial position (r), spanwise position (s). r is defined as the distance in the $\boldsymbol{e_{r,3}}$ direction from p_r. s is defined as the distance in $\boldsymbol{e_{b,3}}$ direction from p_b. They are related as $r = R_h + s\cos(\beta)$. Coordinates r and s range from 0 to tip radius (R) and blade length (S) respectively.

Centrifugal force (Eq. A2a) acts in the $\boldsymbol{e_{r,3}}$ direction. For load-alignment the important component is in the $\boldsymbol{e_{b,1}}$ direction. Employing Eq. A1d results in the new relation Eq. A2b.

$$\boldsymbol{F'_C} = \omega^2\, m'\, r\, \boldsymbol{e_{r,3}} \tag{A2a}$$
$$\boldsymbol{F'_C} \cdot \boldsymbol{e_{b,1}} = -\omega^2\, m'\, (R_h + s\cos(\beta))\sin(\beta) \tag{A2b}$$

Gravitational force (Eq. A3a) acts in the $-\boldsymbol{e_{i,3}}$ direction. For load-alignment the important component is in the $\boldsymbol{e_{b,1}}$ direction. Employing Eq. A1e results in the new relation Eq. A3b.

$$\boldsymbol{F'_G} = -\, m'\, g\, \boldsymbol{e_{i,3}} \tag{A3a}$$
$$\boldsymbol{F'_G} \cdot \boldsymbol{e_{b,1}} = m'\, g\, (\sin(\beta)\cos(\tau)\cos(\psi) - \cos(\beta)\sin(\tau)) \tag{A3b}$$

The initial thrust force (from simulation tool) acts in the $\boldsymbol{e_{r,1}}$ direction (Eq. A4a). Differential thrust force is proportional to the differential annular area the element passes through (Eq. A4b). Distributed thrust force at any coning angle can be related to the initial coning angle with Eq. A4c. For load-alignment the important component is in the $\boldsymbol{e_{b,1}}$ direction. Employing Eq. A1d results in the new relation Eq. A4d.

$$\boldsymbol{F'_T}\Big|_{\beta = \beta_i} = F'_{T,i}\, \boldsymbol{e_{r,1}} \tag{A4a}$$
$$C = \frac{dF_T}{2\,\pi\, r\, dr} = \frac{1}{2\,\pi\,(R_h + s\cos(\beta))}\frac{dF_T}{ds}\,\frac{ds}{dr} = \frac{1}{2\,\pi\,(R_h + s\cos(\beta))\cos(\beta)}F'_T \tag{A4b}$$
$$F'_T(\beta) = F'_{T,c}\,\frac{(R_h + s\cos(\beta))\cos(\beta)}{(R_h + s\cos(\beta_c))\cos(\beta_c)} \tag{A4c}$$
$$\boldsymbol{F'_T} \cdot \boldsymbol{e_{b,1}} = F'_{T,c}\,\frac{(R_h + s\cos(\beta))\cos^2(\beta)}{(R_h + s\cos(\beta_c))\cos(\beta_c)} \tag{A4d}$$

The root flapwise bending moment is defined as the reaction moment about the $\boldsymbol{e_{b,2}}$ axis (Eq. A5a). Equations A5b - A5d show the components of the moment as a function of coning angle. The three components combine to equal the root flapwise bending moment as a function of coning angle (eq. A5e).

$$M = \int_0^S \left(\boldsymbol{F}' \cdot \boldsymbol{e_{b,1}}\right) s\, ds \tag{A5a}$$

$$M_C = -\omega^2 \sin(\beta) \int_0^S m' \left(R_h + s\cos(\beta)\right) s\, ds \tag{A5b}$$

$$M_G = g \left(\sin(\beta)\cos(\tau)\cos(\psi) - \cos(\beta)\sin(\tau)\right) \int_0^S m'\, s\, ds \tag{A5c}$$

$$M_T = \frac{\cos^2(\beta)}{\cos(\beta_c)} \int_0^S F'_{T,c} \frac{R_h + s\cos(\beta)}{R_h + s\cos(\beta_c)} s\, ds \tag{A5d}$$

$$M(\beta) = M_C + M_G + M_T \tag{A5e}$$

Chapter 3

Measurements and Predictions of Wind Turbine Tower Shadow and Fairing Effects

Abstract

Downwind two-bladed rotor configurations can have advantages in reducing rotor mass for wind turbines, compared with three-bladed upwind designs. However, the tower shadow adds an aerodynamic complication that can be difficult to quantify and predict. This study presents and analyzes a previously unpublished subset of data collected during an extensive wind tunnel campaign, the Unsteady Aerodynamic Experiment (UAE). At high tip speed ratios, the tower shadow is a dominating contributor to bending moment oscillations but can be mitigated by the use of a tower fairing when such a fairing is aligned with the flow. At lower tip speed ratios where the blades can undergo aerodynamic stall and hysteresis, tower shadow was only a secondary contributor to bending moments and the tower fairing did not significantly impact bending moments. The aeroelastic simulation code, FAST, was used to predict the same experimental conditions. In general, simulations reasonably predicted most of the cycle-averaged aspects, but only qualitatively predicted the unsteady variations due to tower shadow. To improve simulation predictions inside the tower wake, it is suggested that future work model the unsteady wake component associated with cylinder shedding and to consider a wake model for tower fairings at various wind incidence angles.

1. Introduction

1.1 Downwind Rotors

An average wind turbine in 1980 had a 15 m rotor diameter and produced 55 kW of power (Quarton & Hanssan, 1998; Shikha & Kothari, 2003). Today, MHI Vestas manufactures turbines with a rotor diameter of 164 m with a world-record 8-9 MW rated power. Furthermore, Sandia National Laboratories (SNL) (Griffith & Ashwill, 2011) released the design for 'the hundred meter blade', and DTU Wind Energy (Bak *et. al.,* 2012) has published work on a 10 MW reference turbine. However, the trend of increasing size is not as fast as in previous decades due to the increasing blade mass to accommodate stress levels that occur as the blades grow in length (Kim, Larsen & Yde, 2014). Structural limits are being reached with the conventional three-bladed, horizontal axis, upwind rotor design resulting in a search for innovative designs (Veers, *et al.*, 2003).

One option, especially being considered to reduce rotor mass is the use of a two-bladed, downwind configuration. The first megawatt-scale wind turbine, Smith-Putnam turbine, used this configuration (Nielsen, 2010). Ming Yang, a Chinese company, worked with Aerodyn from Germany, to manufacture two downwind, two-bladed prototypes, one with rated power of 6 MW and the other with 8 MW. Hitachi, from Japan has been developing a 2 MW and 5 MW rated downwind turbine, using a three-bladed design (Qin & Loth 2016). Moving from an upwind rotor to a downwind rotor may give significant structural advantages, which can help support the evolution of extreme-scale wind turbines of 10-20 MW. Reducing the blade number from three to two results in a rotor mass reduction that corresponds to a lower manufacturing and assembly cost.

The blade number reduction does introduce unfavorable structural loads and instabilities, however these may be managed with the use of a teeter hinge or through advanced turbine control, leading many to think the benefits outweigh the costs (Loth, *et al.*, 2012; Icther, *et al.*, 2015; Noyes, *et al.*, 2018).

However, a well-known concern with downwind turbines is the potential impact of tower shadow, i.e., the downstream wake from the tower impacting the blades as they pass through. The tower shadow is an aerodynamically unsteady region, with significant variations in flow angle and velocity, and with a net momentum deficit. As the downwind turbine blades pass through this region of velocity deficit and increased turbulence, the flow seen by the blade is directly modified. In particular, this can cause a rapid change of the blade's aerodynamic loading (Leishman, 2002; Zahle, *et al.*, 2009). The load fluctuations can increase fatigue damage, or excite a blade vibrational mode (Yoshida, Kiyoki, 2007). In addition to load fluctuation, tower shadow causes a distinct low frequency acoustic noise (Madsen, Aagaard, 2010). This tower shadow induced 'thumping' is the primary reason why upwind rotors became conventional over downwind (Koh, Ng, 2016).

Aerodynamic fairings to cover the tower have been a proposed solution to the tower shadow problem. More validation is required for the tower fairing solution, specifically the effectiveness of the fairing at misaligned conditions (with non-zero fairing angle of attack), which can occur because of wind direction changes in environmental conditions (O'Connor, Loth & Selig, 2013).

1.2 Tower Shadow Experiments

To quantify and understand tower shadow, previous experimental studies (Orlando, *et al.* 2011) conducted an experiment to measure the wake caused by turbine towers at different Reynolds numbers. Anemometers were used to measure average wind speed at various locations. The experiment provided valuable understanding on the time averaged velocity deficit, as well as indicating the limitations of data measured with anemometers. However, the instrumentation only allowed for average data to be collected, which gives no insight into the instantaneous and unsteady structures of the wake and the data was collected from a tower without a rotor, which ignores any induction effect the rotor has on the wake flow field and does not allow direct examination of the impact on blade root moment.

Water tunnel experiments (O'Connor *et al*. 2013) experimentally investigated the wake behind a cylinder and thick symmetric airfoils at various angles of attack (0°, 10° & 20°) to mimic the wake behind a tower (faired and unfaired) at various yaw angles. They used Particle Image Velocimetry (PIV), to achieve a series of instantaneous realizations of the velocity field of the wake. This experiment provides an understanding of the effectiveness of fairings as a method of wake reduction at various yaw angles. However, as with the Orlando *et al.* study, no direct information was obtained on how the wake affects the rotor, and conversely no information is offered on how the rotor affects the wake.

The National Renewable Energy Laboratory (NREL) performed an experimental campaign Phase VI on the UAE turbine in the NASA Ames wind tunnel (Hand, *et al.*, 2001). Tests were conducted in both the upwind and downwind (faired and unfaired) configurations, as shown in Fig. 1. Instantaneous measurements were taken in full rotor operating conditions, leading to a better understanding of tower wake effects on the rotor blades, compared to previous experiments. Pressure taps at various positions along the blade provide a measure of aerodynamic load and consequently insight on tower shadow affects those loads. Strain gauges placed at the root of the blade, provide a measure of root bending loads. The tower shadow can be seen in Fig. 1a, by the flow visualization disturbed behind the tower. The tower fairing used in the experiment can be seen in Fig. 1b. This is perhaps the only data set to comprehensively and quantitatively examine the unsteady influence of the tower wake and that of fairings on flow fields, blade forces and moments (and such aspects have not been previously published).

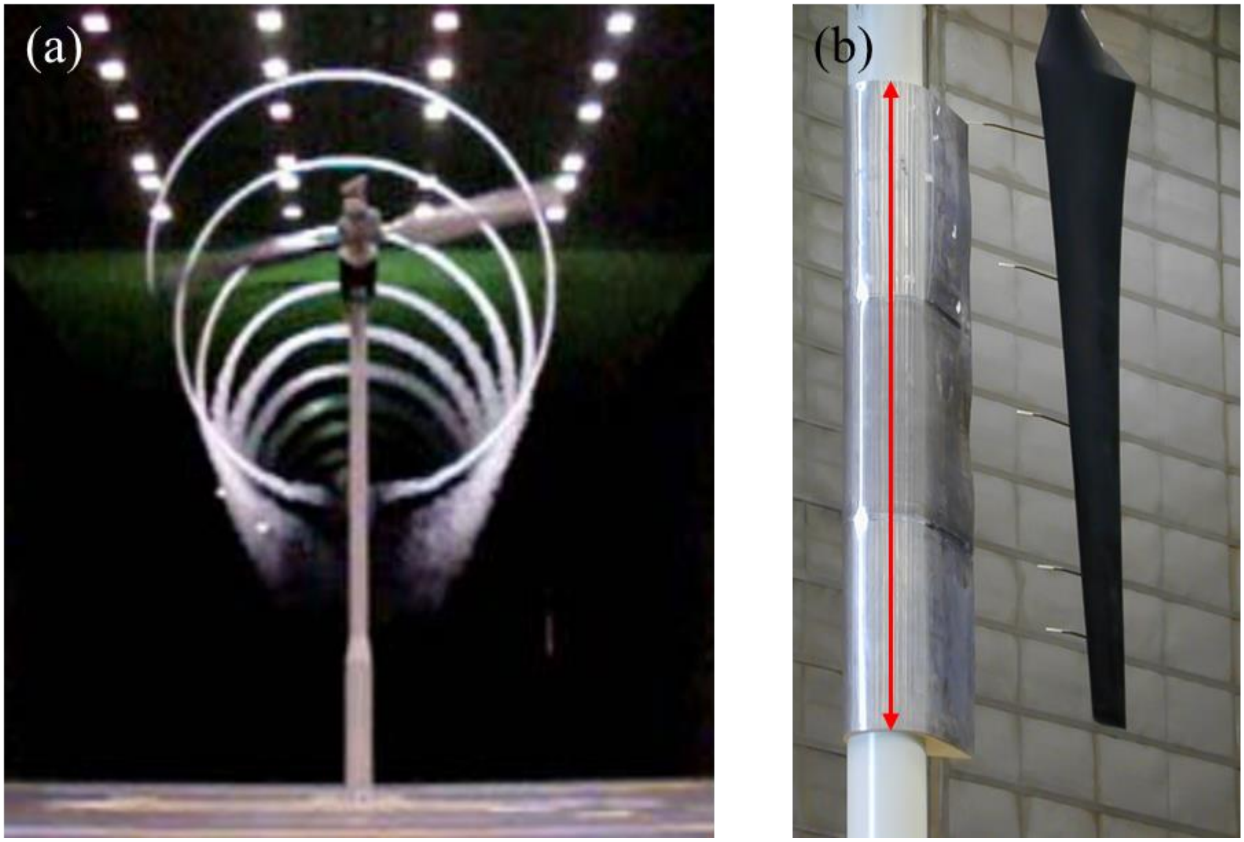

Figure 1. UAE experimental configuration in the NASA Ames tunnel: (a) flow visualization of tip vortices, and (b) UAE tower fairing (with arrow indicating vertical extent) upstream of a UAE blade instrumented with 5-hole pressure probes (Hand *et al.* 2001)

1.3 Tower Shadow Models

Coton *et al.* has done significant work on developing computational tower shadow models for downwind turbines (Wang & Coton, 2001; Wang & Coton, 1999; Munduate *et al.* 2004). The tower wake is modeled as a time-averaged velocity deficit and does not include variations due to vortex shedding and turbulence. However, these models incorporate a transient lift response to a sudden gust. This unsteady component of blade response improves the model in that it can predict the azimuthal asymmetry that can be experimentally seen. However, a detailed study on tower shadow (Zahle, *et al.* 2009) suggests that the asymmetry seen in aerodynamic response may be instead due to the effects of the rotor swirl and circulations on the tower wake.

Turbine simulators such as FAST (Jonkman, *et al.,* 2005) and BLADED (Hassan, 2013) often have a method for simulating tower shadow effect. The most common tower shadow is a steady velocity deficit model proposed by Powles (1983). Adaptions have been suggested, such as flow deflection based on the potential flow solution (Moriarty & Hansen, 2005). However, in general the model does not incorporate any unsteadiness such as vortex shedding, thus solely intended to predict the time-averaged velocity field induced by the tower shadow, but is not designed to capture the instantaneous variations.

Improvements to the velocity deficit tower shadow model can be attained by adding a specified amount of Kaimal spectrum turbulence intensity within the wake as demonstrated by Reiso *et al.* (2013). This adds an unsteady element to the otherwise steady wake improving the predictions. This modification requires a CFD calibration step, and to rewrite the wind input files. Another drawback is that the adaptation ignores the large coherent vortex structures, however Reiso states that these influence the rotor dynamics much less than the small scale turbulent structures. While Reiso's tower shadow model is an improvement, it has yet to be generally adopted. Many downwind turbine simulations implement the steady tower deficit model based on Powles.

FAST employs an aerodynamic module (AeroDyn) that is based on the Blade Element Momentum (BEM) method (Moriarty & Hansen, 2005). Simply, the BEM method is a combination of the blade element theory and the momentum theory. The blade element theory divides the blade into a number of 2D airfoil sections. The momentum theory calculates the change in flow speed through the rotor by calculating the work done to the rotor. These two theories together provide the framework for AeroDyn. Additional models are also included in FAST, such as a tip-loss model, hub-loss model, and the aforementioned tower shadow model.

1.4 Objectives

The present study has two primary objectives: 1) to analyze the effects of fairing misalignment on the blade flow condition as well as blade forces and moments for a downwind configuration, and 2) to assess the capability of a steady tower shadow model used in many commercial turbine simulators to predict the instantaneous and time-averaged blade forces and moments. For the first objective, this study analyzes previously unpublished portions of a UAE experimental campaign, specifically those pertaining to flow misalignment of a tower fairing. This experimental campaign was unique in that it includes both the flow field measurement of the wake (important to understand wake physics), coupled with direct measurements of blade bending moments (important to understanding of resultant blade stress and fatigue). The present study is the first to analyze these fully-coupled unsteady shadow effects on a downwind turbine for various configurations and to compare these to a conventional upwind configuration. Using this unique data set can also allow insight into conditions when the tower shadow is likely to substantially influence blade bending moments, and the conditions for which a tower fairing may be useful in mitigating the negative effects of the tower shadow. For the second objective, the study compares the time-dependent results with FAST, to determine if the current tower shadow models used for aeroelastic predictions are qualitatively and quantitatively reasonable in predicting blade wake interactions for the above conditions. This includes investigation of the capability of modeling the local flow angle and velocity as well as the capability of modeling the blade forces and bending moments. In particular, consideration is given in terms of cycle-averaged values as a function of azimuthal angle as well as the maximum range experienced due to unsteady and stochastic effects.

2. Experiment and Analysis

2.1 Experimental

The Unsteady Aerodynamic Experiment (UAE) Phase VI (Hand, *et al.* 2001) was performed by NREL, at the NASA Ames Research Center, in the NFAC 80 ft x 120 ft test section, with less than 2% blockage. Several different turbine configurations were tested including, both upwind and downwind rotor configurations, both rigid and teetered rotors, both cylindrical and faired tower geometries. The test also included a variety of cone angles, yaw angles, blade pitch angles, rotor speeds, and tunnel inlet velocities. The general turbine parameters for the analyzed cases are outlined in Table 1. Measurements included flow pressure, flow angles, blade surface pressures, and blade loads at a rate of 520.83 (Hz). This study focuses on the results that directly pertain to the differences between upwind and downwind rotors and those with and without the use of a tower fairing.

Table 1. General turbine parameters.

Blade Length	5.029 m
Blade Number	2
Hub Height	11.5 m
Tower Diameter	0.406 m
Rotational Speed	72 rpm
Shaft Tilt Angle	0°
Blade Pitch	3°
Rotor Yaw	0°

The objective of this study is to specifically investigate how the tower shadow affects the flow field seen by the blade, blade aerodynamic response, and the blade loading in terms of flapwise bending moment. For this, four different configurations were analyzed as shown in Fig. 2 and outlined in Table 2 based on three sequences:

1) Sequence H: an upwind rotor with a cylindrical tower (UC)
2) Sequence B: a downwind rotor with a cylindrical tower (DC)
3) Sequence 7: a downwind rotor with a tower fairing aligned with the flow (DF0)
4) Sequence 7: a downwind rotor with a tower fairing a misalignment angle, χ_F = 20° (DF20)

The fairing misalignment angle, χ_F = 20°, was chosen from the two options of 10° and 20° because O'Connor *et al.* (2014) showed that this was the maximum misalignment angle that turbines with yaw control should be designed to manage. These four different configurations are shown in Fig. 2 and outlined in Table 2. The differences in coning angle and teeter between the four cases will lead to some performance changes. The difference in coning angle will affect the mean bending load, and differences in teeter could affect the range of bending loads. These differences are noted when relevant.

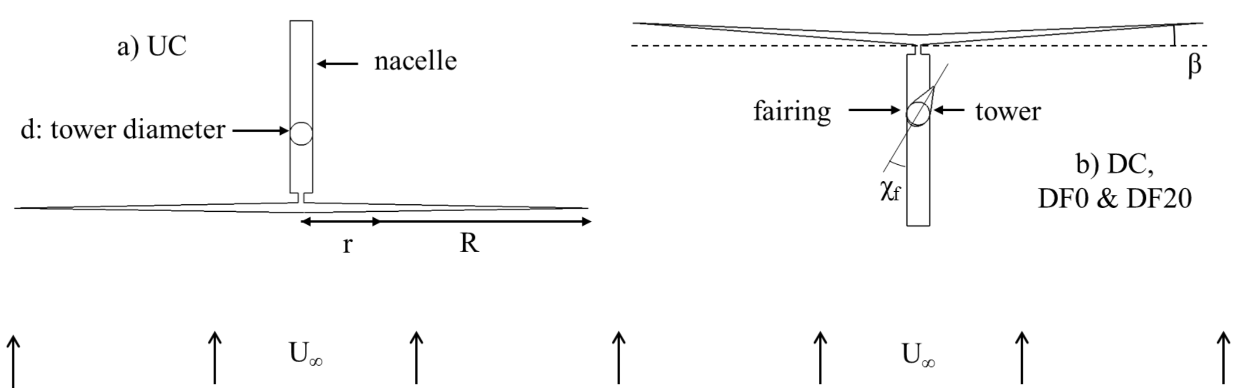

Figure 2. Top view turbine schematic: (a) upwind rotor and (b) downwind rotor with fairing free to rotate about tower

Table 2. Case specific parameters.

	UC	DC	DF0	DF20
Cone Angle	0°	3.4°	3.4°	3.4°
Rigid/Teetered	Rigid	Teetered	Rigid	Rigid
Fairing Chord	NA	NA	0.89m	0.89m
Fairing Span	NA	NA	3.66m	3.66m
Fairing Angle	NA	NA	0°	20°
Tip Clearance	1.2m	1.5m	1.0m	1.0m

Tests for all four configurations were completed at mean upstream velocities (U_∞) of 5, 7, 10, 15, 20 and 25 m/s. As this velocity approaches the rotor plane, it is slowed and modified by induction and other effects, including any instantaneous wind deflection from tower wake for a downstream rotor configuration. The instantaneous wind velocity just upstream of the rotor is then defined as U, as shown in Fig. 3. The resultant flow vector seen by the blade at a given radius (r) is the vector addition of streamwise flow (U) and local blade rotational speed (V_ω=ωr). The resultant velocity is defined by the resultant flow speed (V_r) and aerodynamic angle of attack (α) relative to the blade chord line. It should be noted that U and α were not obtained directly in the UAE test but are related to other measurements that were obtained.

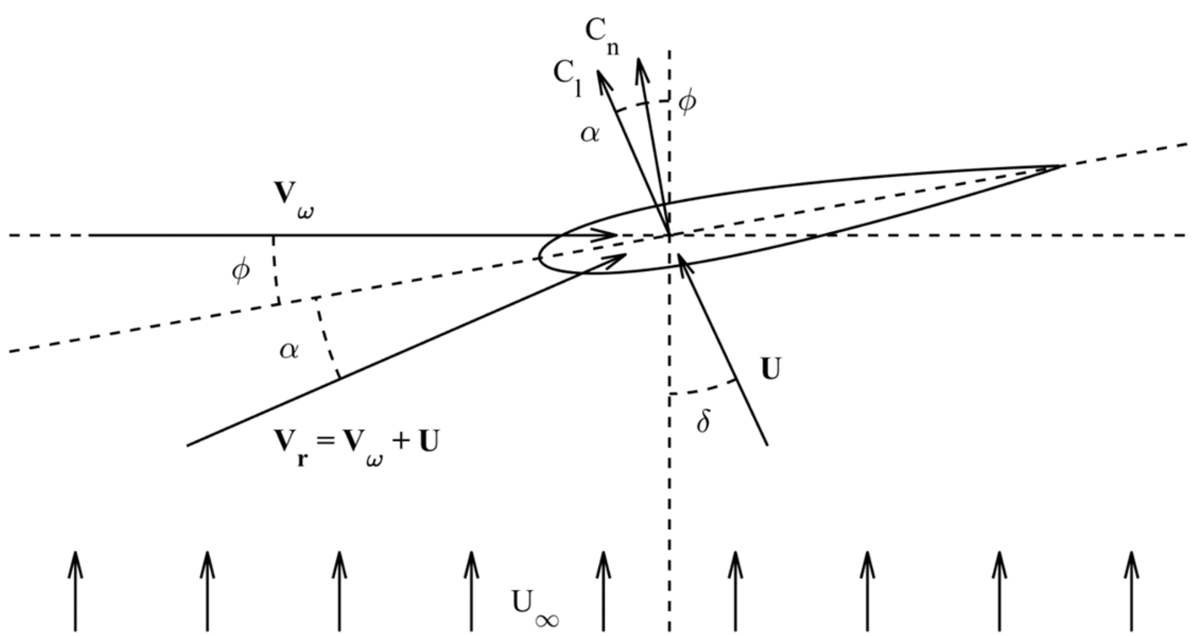

Figure 3. Schematic of flow parameters: pitch plus local twist (φ), instantaneous wind deflection (δ), instantaneous wind (U), free stream wind (U_∞), angle of attack (α), rotational velocity (V_ω), where C_n is normal to chord line & C_l is normal to the resultant flow (V_r).

In particular, four of the measured variables from the test were analyzed herein: Local flow angle (LFA), resultant velocity (V_r), normal force coefficient (C_n), and root flapwise bending moment (M). The flow parameters were measured at r/R = 0.34, 0.51, 0.67, 0.84 & 0.91 with 5-

hole probes extending ahead of the blade by 80% the local chord length (Hand, *et al.*, 2001). Importantly, LFA values based on these probes are related to, but differ from, α. The differences are described later in the Results and Discussion section. Surface pressures were also measured along the blade surface using pressure taps, which were then used to calculate pressure coefficient at various positions along the span and chord. Integrating these pressure coefficients along the chord at r/R = 0.30, 0.47, 0.63, 0.80 & 0.95 (and neglecting skin friction effects) yielded the local aerodynamic normal force coefficient (C_n). Local blade properties at two of the key spanwise stations are provided in Table 3. Finally, strain gauges mounted at the blade root were used to measure M.

Table 3. Geometric properties at key spanwise locations.

r/R	Chord Length (m)	Pitch + Twist (degrees)	Rotational Speed (m/s)
0.63	0.543	4.150	23.9
0.67	0.523	3.719	25.4

2.2 Computational

To examine the steady tower shadow model, FAST was used to model the test conditions (UC, DC, DF0) and output the same four variables previously defined (V_r, α, C_n, M). The upstream velocities were nominally set at integer values (5, 7, 10, 15, 20 and 25 m/s) the actual free stream values measured were slightly different. These two velocities are outlined in Table 4 with significant digits consistent with experimental accuracy. The experimentally measured velocities were used in the simulations however in the discussion below, the results will be referred to by the nominal value not the measured value.

Table 4. Nominal and experimentally measured free stream velocities in m/s.

Nominal	UC	DC	DF0	DF20
5	5.08	5.06	5.00	5.00
7	7.05	6.68	7.00	6.99
10	10.07	10.32	10.05	10.02
15	15.03	14.85	15.05	15.04
20	19.99	20.66	20.12	20.11
25	25.22	25.67	25.18	25.19

The tower drag model used in the simulations uses the drag of a cylinder to calculate the average velocity reduction behind the tower (Calkins, 1984) define with equations 1 and 2:

$$u_{wake} = \frac{C_d}{\sqrt{x^2+y^2}} \cos^2\left(\frac{\pi}{2}\frac{y}{\sqrt{x^2+y^2}}\right) \qquad for \quad |y| \le \sqrt{x^2+y^2} \qquad (1)$$

$$u_{wake} = 0 \qquad for \quad |y| > \sqrt{x^2+y^2} \qquad (2)$$

The specific value of the drag coefficient is based on the drag of a cylinder versus Reynolds number. Although the tower shadow model does not include an option for a faired tower, there is an option to specify C_d, by adapting the lookup table. The DF0 case was modeled by assuming that the fairing wake was could be approximated by an ellipse with ratio of major to minor axis of 0.5. Drag coefficient vs Reynolds number of an ellipse is shown to be roughly 75% of the drag of a cylinder over the operational Reynolds numbers of the UAE. Specifically, data from Belvins (1984) shows the range to be between 70% and 85% over the operating range, which is a remarkably tight range considering the operating range passes through the critical Reynolds numbers for both the cylinder and the ellipse. Base on Belvins and drag data for a similarly thick fairing aerodynamics from (O'Connor, *et al.* 2013) roughly modeling the fairing with a constant 75% drag reduction was deemed reasonable. Note that this drag coefficient was not later adjusted nor optimized to improve the predictions relative to the experiments. For the fairing at misalignment angle of 20 degrees (DF20), a comparable drag coefficient could not be reasonably approximated and furthermore the effects of unsteadiness were likely to be more extreme, indicating that a mean wake model may be inappropriate. Therefore, no simulations were conducted for the DF20 cases.

3. Results and Discussion

The results are examined in the order of causation influence, starting with the tower shadow impact on flow angles and flow speeds seen by the blades, followed by examining how these speeds and angles impact the aerodynamic blade forces, and the blade root bending moments. The tip speed ratio (TSR) is 5.42 at upstream velocity (U_∞) of 7 m/s. This TSR is a typical magnitude for many turbines. For example, the NREL 5MW reference turbine has a TSR of 7.08 at rated conditions. The highest TSR case (U_∞ = 5 m/s) was not chosen for in depth analysis because the lower inlet speed lead to relatively high turbulence in the wind tunnel and therefore a high signal to noise ratio. For this reason, the cases at U_∞ = 7 m/s are analyzed in the most depth, although cases with different TSRs are also discussed. The tower Reynolds number at U_∞ = 7 m/s based on tower diameter is 189,000, which is in the super-critical drag regime.

3.1 Effect on Resultant Flow Field

The 5-hole pressure probes used in the UAE experiment measured the local flow field at 0.8 chord length in front of the airfoil (Hand, *et al.*, 2001). The local flow angle (LFA) is generally not equal to the local aerodynamic angle of attack (α, of Fig. 3) since the LFA also includes effects associated with the local aerodynamic influence of the blade on the flow just upstream, including effects of a) upwash due to local lift, b) streamline deviation due to blade finite thickness, c) swirl induced by the rotor, and d) tip vortices. Of these effects, upwash due to the lift-induced bound vortex is often the most significant. The upwash from the bound vortex can be approximated by relating the local lift per unit span to circulation (Γ), which can then be employed to determine induced upwash velocity via the Bio-Savart law for a vortex filament, as shown in Fig. 4. Notably the upwash is linearly proportional to lift (which is linearly proportional to Γ and α), but is inversely proportional to distance from vortex center, which was taken to be at the quarter-chord. For $x/C=0.8$ (the UAE measurement point), this relationship can thus be shown to yield LFA $\approx 1.5\alpha$. As such, the local flow angle will generally be 50% larger than the aerodynamic angle of attack (for the experimentally used probe positions) if only 2-D bound vortex is considered. Tip losses will tend to reduce this difference, especially for more outboard stations, while effects of streamline deviation and swirl are even more complicated to evaluate. The differences between LFA and α for the UAE have been investigated in depth (Sant *et al.* 2006) but an accurate relationship that can be used as a general theoretical correction was not found. Since no relationship is available, it is only noted herein that LFA is related to, but not equal to, α.

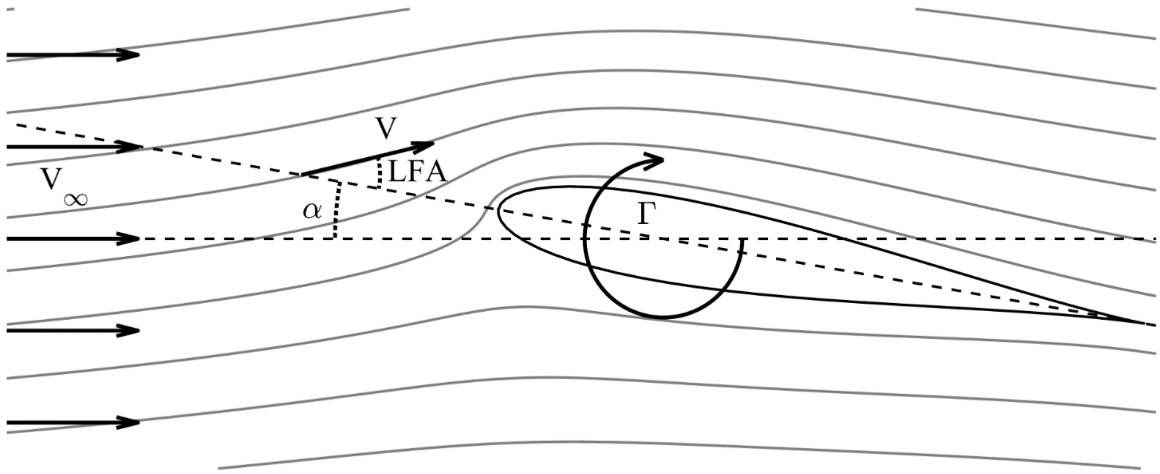

Figure 4. Upwash in front of a two-dimensional airfoil with a bound vortex of strength Γ, which cause the flow angle measured upstream to be increased relative to the aerodynamic angle of attack, which ignore such upwash effects.

Figure 5 shows the LFA (black & gray: experimental) and α (red: simulated) at r/R=0.67 for 36 complete revolutions. This radial location was chosen as the point that approximately separates the swept area in half, i.e. the area inboard of this location approximately equals the swept area outboard of the location. For the upwind case (UC), the LFA is smooth and generally unaffected by the tower shadow, this is in part due to the large overhang for the rotor. Conversely, in all three downwind cases the LFA is greatly influenced by the tower shadow. This is especially true in the region of 160°<ψ<200°, where the LFA varies significantly. In particular, there is a strong average decrease (black line) in LFA near ψ~180°. In the region, the instantaneous data (gray points) varies significantly from the average. This is due to the rotor passing through an unsteady wake with positive and negative wind deflection (δ from Fig. 3).

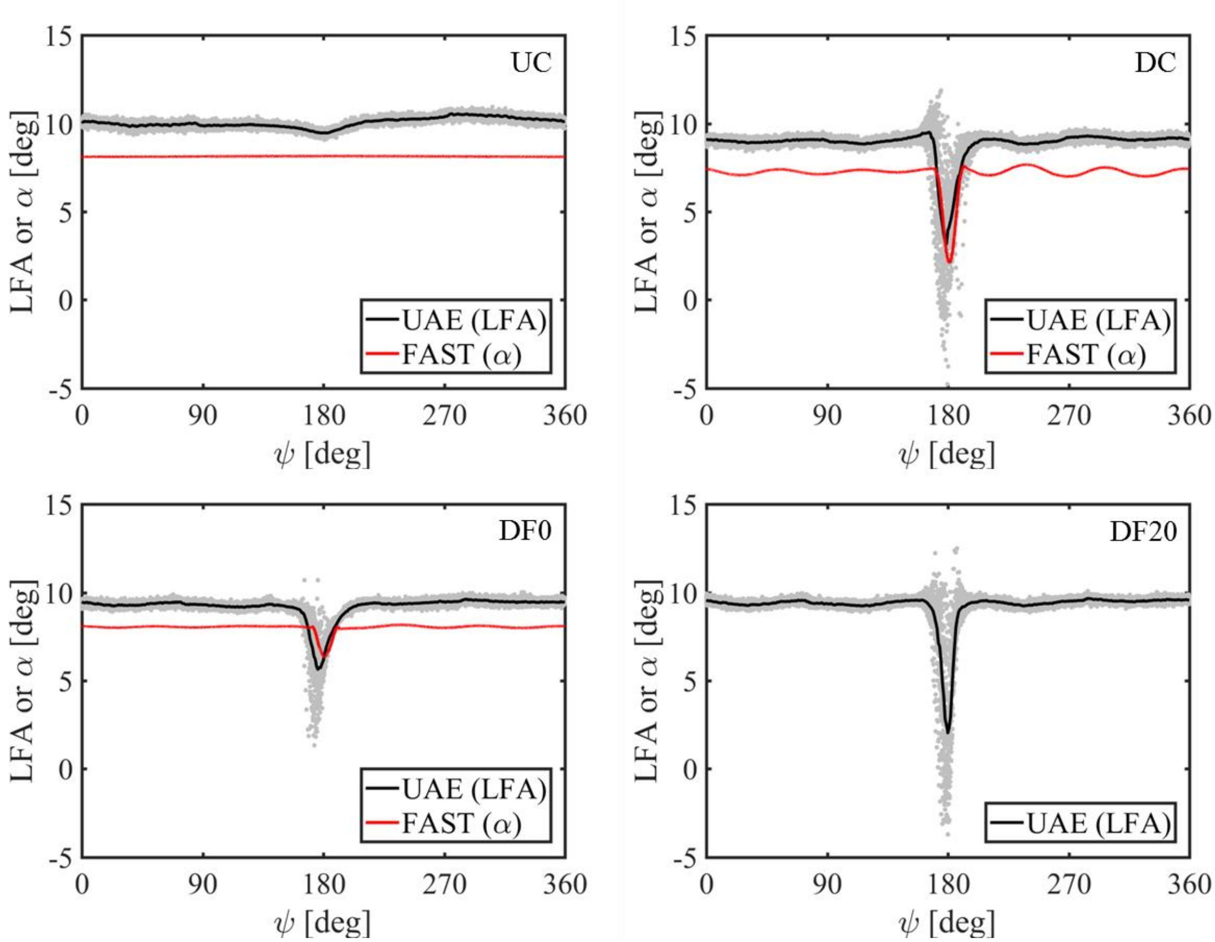

Figure 5. Local flow angle (experimental) & angle of attack (computational) as function of azimuthal angle at r/R=0.67 and U_∞=7m/s. The grey dots indicate instantaneous measured values while the solid black line indicates the cycle-averaged measurements (averaging all values for a given ψ value), and the simulations (red lines) are quasi-steady given that the inflow velocity is steady and wake model assumes a steady velocity distribution with no shedding (Eqs. 1-2). As expected due to upwash effects, the LFA is greater than the aerodynamic angle of attack.

An interesting phenomenon observed is that LFA is not symmetric about ψ=180°, primarily in the DC case. Near ψ~170°, the instantaneous values of LFA can be significantly higher than wake-free values (ψ<160° & ψ>200°). This increase is not seen as the blade exits the wake (ψ~190°) demonstrating that the tower shadow effect is not simply a symmetric reduction in LFA. Since this asymmetry occurs upstream of the blade, it is likely due an interaction effect between rotor swirl and the tower wake. Such an upstream influence causing asymmetry was previously suggested by Zahle *et al*. (Zahle, *et al.*, 2009) Another indication of slight azimuthal asymmetry is that the drop in average LFA entering the wake is steep whereas the return to wake-free values is relatively slower. When comparing the downwind cases of a cylinder tower (DC) vs. a faired tower (DF0), there is an interesting difference in instantaneous extremes. The DC case has LFA values as low as -5° and as high as 12°, whereas the DF0 LFA values are generally confined between 0° and 10°. In general, the DF0 case has variations are limited to be about one-half that of the DC case. However when the misalignment angle, χ_F, is increased to 20° in the DF20 case, LFA seen by the blade for the faired tower is similar to the un-faired case. This suggests that the fairing alignment angle is critical to mitigate tower shadow effects.

It is important to note that FAST (in red) provides the predictions of α, while the experiments measured instead LFA (black). As noted by Fig. 4 and discussion above, LFA should be different and generally greater than α due to upwash, and this difference is consistently seen in Fig. 5 in the azimuthal angles away from the tower shadow (downwind rotors). For the downwind rotors, the strong unsteadiness features seen in the LFA measurements are not reflected by similar variations in the simulation of α. This is an expected result because the tower shadow model is steady and incapable of deviations from the average velocity field. As discussed previously, these instantaneous variations are significant due to large scale shedding and small scale turbulence and can yield flow angle variations on the order of ±7°. This unsteadiness explain why the instantaneous LFA data (grey dots) has strong variations about the cycle-averaged data (black solid lines). For example, the cycle-averaged value always decreases when entering the wake but the instantaneous LFA sometimes increases when entering the wake. This stochastic over-shooting of LFA in the wake and the general variations about the cycle-average are reduced significantly for the faired tower that is aligned (DF0), which can be attributed to significantly reduced unsteadiness for the wake downstream of a fairing.

If one considers the cycle-averaged experimental data for the DC case (solid black line), there is a noticeable wake asymmetry seen in the LFA deficit, whereby the drop in LFA entering to the wake is quicker than the subsequent LFA recovery exiting the wake. This asymmetry can be attributed to a coupled effect of the rotor interacting with vortexes from the wake (Zahle *et al*, 2009). As may be expected, the steady tower shadow model does not simulate this difference. Finally, FAST under-predicts the flow angle drop for the DF0 case, suggesting that the tower 0.75% C_d reduction may have been too great of a reduction for the utilized fairing when predicting the influence on flow angle.

Figure 6, shows generally how the LFA (experimental) and α (computational) change as free stream velocity (U_∞) changes. The boxes show the range of data, the diamond indicates the average value when the blade points directly up (outside of the wake) and the circle indicates the average value when the blade points down (directly inside the wake). As U_∞ increases (TSR reduces) LFA & α predictably increase. The tower shadow substantially increases the variations in angles at all speeds (the variations are negligible for all UC cases). One can also see that the tower fairing reduces the effect of this wake at every speed. Additionally it is clear from the DF20 case that the fairing at high χ_F performs as poorly as or worse than the unfaired (cylindrical tower) case. In terms of predictions, FAST consistently predicts α lower than the LFA measured, as is qualitatively expected due to upwash (Fig. 4). However, the steady tower shadow model does roughly predict the average magnitude of the deficit i.e. the difference between the average flow angle at ψ~0° & ψ~180°. The simulation severely (almost an order of magnitude error in the extreme cases, as shown in Fig 6b) under-predicts the range in the wake for the downwind cases, especially at higher U_∞.

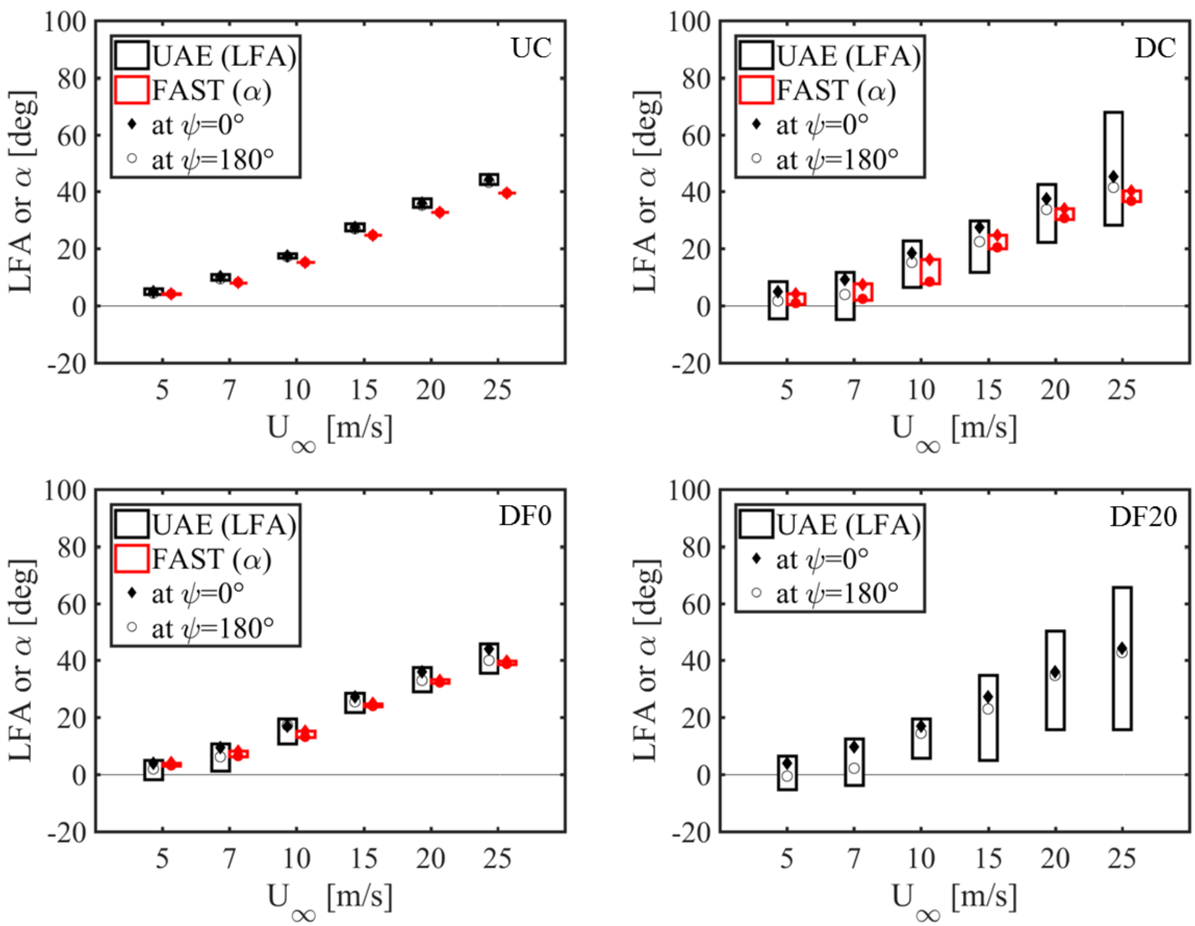

Figure 6. Measured LFA (experimental) & α (computational) at r/R=0.67 at a given wind speed, where cycle-averaging the data for the blade pointed up is given by a solid diamond (◆), cycle-averaging the data for the blade pointed down (behind the tower for downwind rotors) is given by a hollow circle (O) and the range of all instantaneous values is identified an encompassing box (☐)

Figure 7 shows the resultant velocity (V_r), taken at r/R=0.67, plotted against azimuth angle. As expected, there is little variation with azimuth angle in the upwind case, but there is a significant shadow effect in the downwind cases. The average V_r is affected by the tower shadow in all three downwind configurations, although the trend is not consistent. As the blade passes through the wake, there is a slight increase in average flow speed for DC & DF0, but a decrease for DF20. This is not easily explained. Perhaps the fairing turned the flow slightly into the oncoming rotor, which increased the relative flow speed for DF0. Of larger significance are the instantaneous deviations from the average. The deviations are of a magnitude of ±4m/s for DC, ±2m/s for DF0 and ±3m/s for DF20. These significant variations are attributed to the fact that the wake from a cylinder (or fairing) can cause the flow to deflect into and away from (as a function of time) the oncoming rotor. As shown in Fig 3, δ ranging from large positive to large negative values will change the magnitude of V_r.

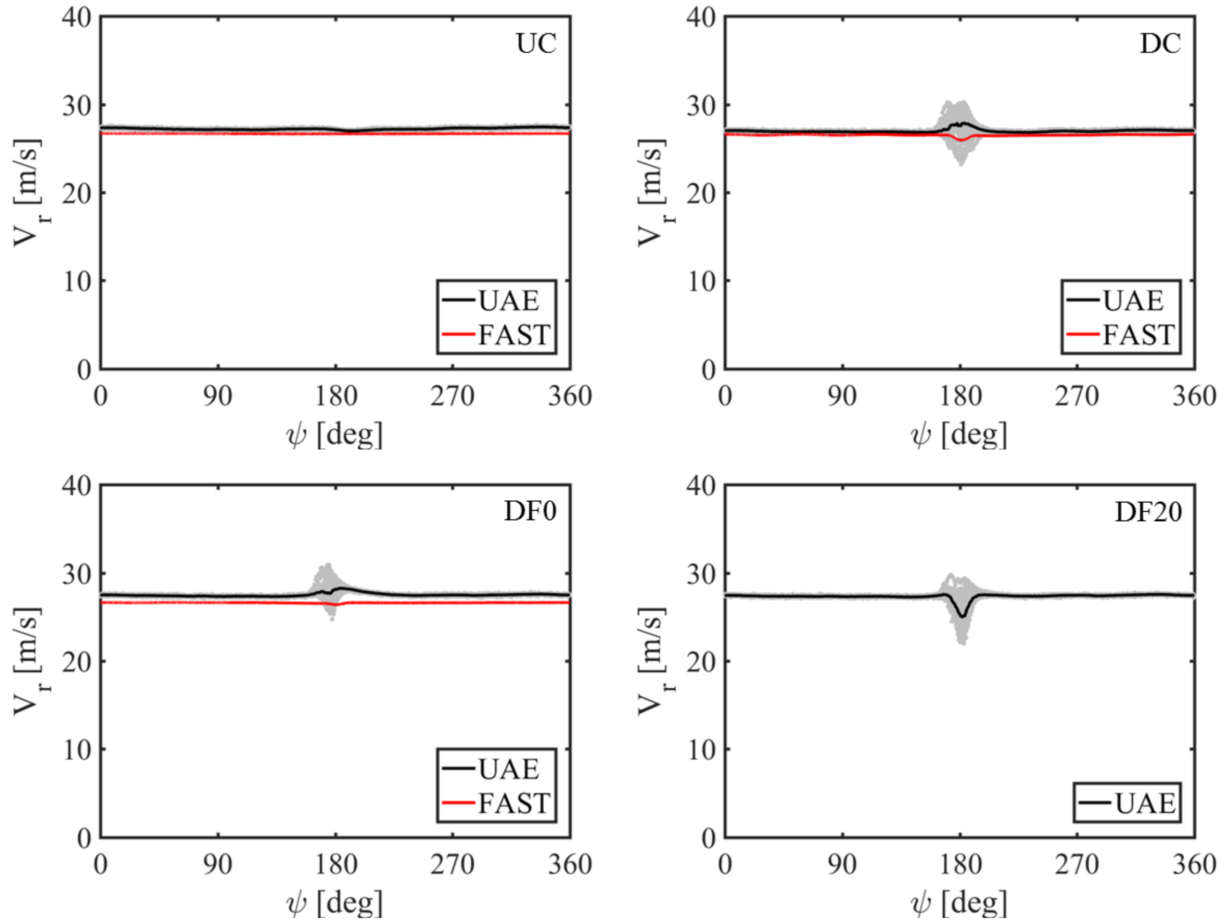

Figure 7. Resultant velocity as function of azimuthal angle at r/R=0.67 and U_∞=7m/s using same symbol representation as in Fig. 5.

In spite of the above complications, FAST accurately models the average results within about 1m/s for all cases. However, the steady tower shadow model results in only a drop in relative flow speed, whereas the trend for the measured data was not consistent, due possibly to average flow deflection. The steady tower shadow model does not lead to any unsteady deviations from the average speed. These deviations are of significant magnitude and this demonstrates a weakness of the wake model.

Figure 8, shows the summary of the resultant velocity measured at r/R=0.67. There is minimal spread in the UC case, maxima and minima are close to the averages, indicating that the tower shadow plays the dominant role in the variation of resultant flow velocity for the downwind cases. With the possible exception of U_∞=10 m/s, the fairing reduces the range of the measured relative flow velocity. Again, the DF20 case performed comparably or worse than the DC case at every speed. FAST predicts reasonably well the average values (both inside and far from the wake). The tower shadow model does lead to correct predictions of the spread of values, which is large inside the tower shadow, with values both much greater and much less than the wake-free value (the diamond).

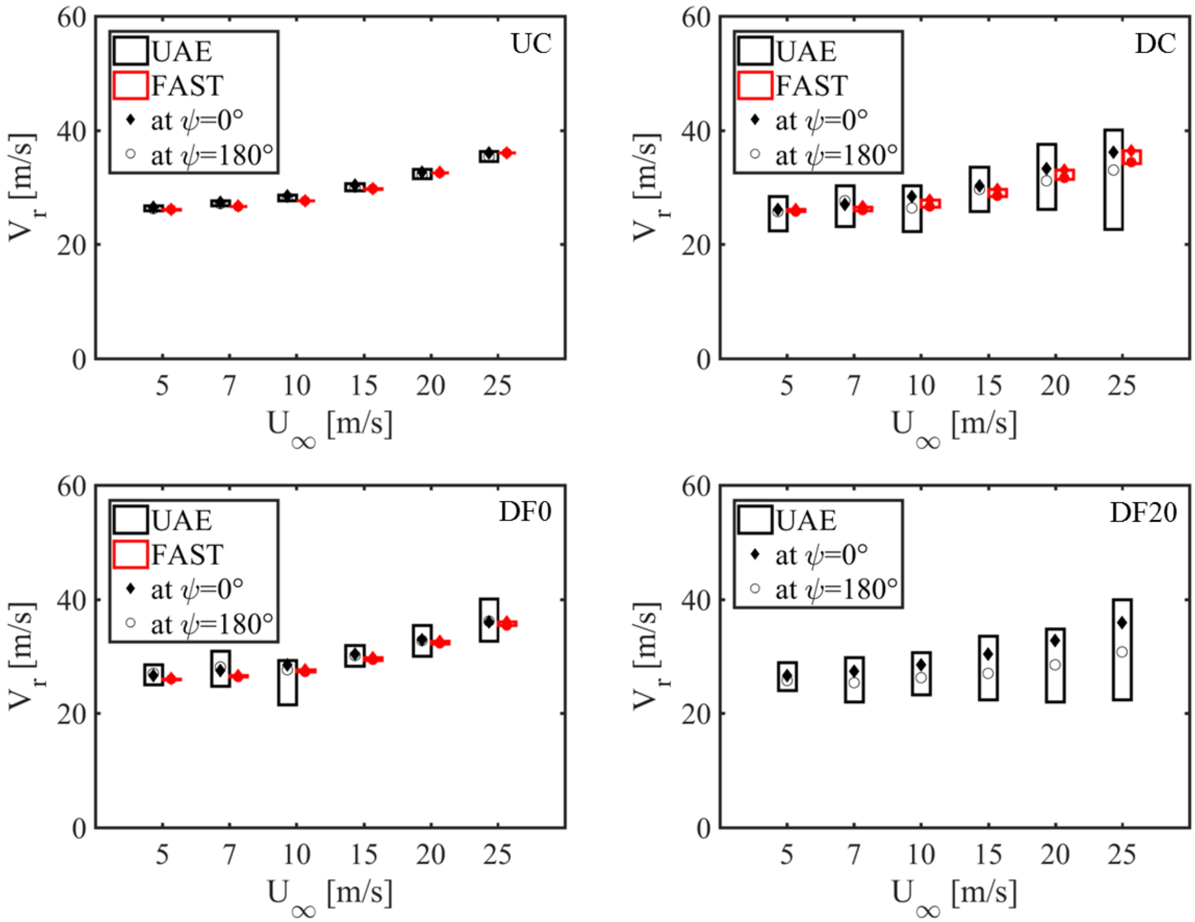

Figure 8. Resultant velocity at r/R=0.67 using same symbol representation as in Fig. 6.

3.2 Effect on Aerodynamic Loads

Figure 9, shows the normal force coefficient, taken at r/R=0.63, plotted against azimuth angle. With respect to the shadow effects in the experimental data, the plots of C_n have many of the same qualitative characteristics as the plots from the LFA (Fig. 5), i.e. a pronounced dip and wake asymmetry. The tower shadow does not only lead to a force reduction. There are instantaneous cases where the loads are significantly larger inside the tower shadow than the wake free values. Primarily as a result of the flow angle effects, the fairing decreases the peak C_n deficit in the DF0 case by about two-fold. Again, this reduction is lost for the DF20 (misaligned fairing) case as it behaves similarly to the DC (cylindrical tower case).

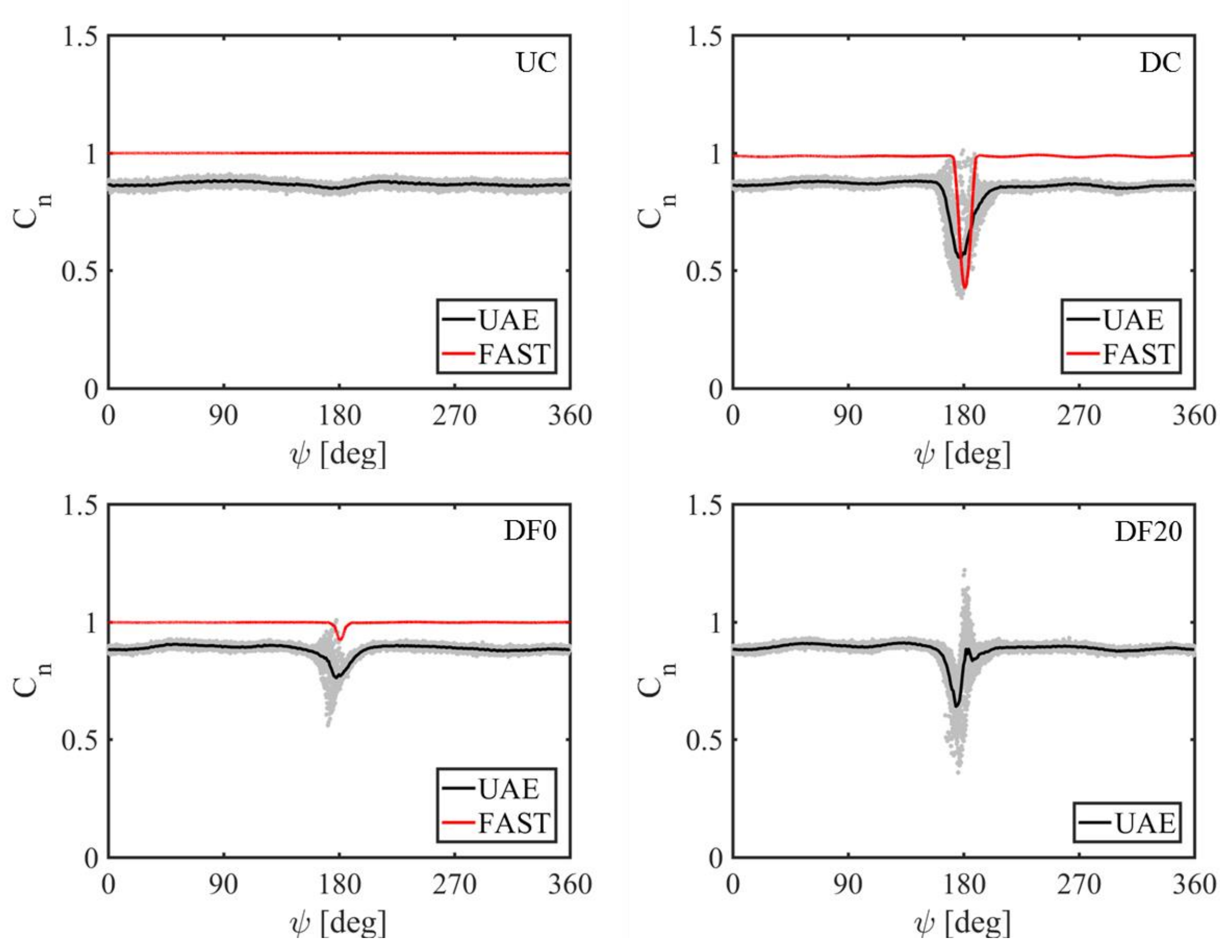

Figure 9. Normal force coefficient as function of azimuthal angle at r/R=0.63 and U_∞=7 m/s using same symbol representation as in Fig. 5.

Interestingly, FAST significantly over-predicts the average wake-free value of C_n (by about 15-20%) for all cases. This may be attributed to airfoils aerodynamically underperforming compared to the ideal case due to airfoil roughness, manufactured imperfections, instrumentation, 3D effects, or flow unsteadiness. In terms of tower shadow effect on C_n, The wake model greatly over-predicts the effect for the cylindrical tower (where wake unsteadiness is expected to be high) but under-predicts for the faired tower (where wake unsteadiness is expected to be low). Some of these differences can also be attributed to the short length and time scales of the wake, whereby FAST assumes a chord-wise averaging phenomenon but the wake interaction time-scale is similar to the aerodynamic time-scale. For example, assuming a wake interaction of $\psi{\sim}10°$, the interaction time-scale is about 0.025 s, which is on the order of the time-scale for flow over the chord length, C/V_r~0.02 s. This is a result of the chord length is on the order of the wake width, which can result in highly non-linear fluid dynamic interactions. To improve the simulation, FAST may require a more sophisticated aerodynamic interaction model with unsteady aerodynamic hysteresis effects.

Despite this problem with FAST for the DC case, the wake model leads to predictions that are too low for the DF0 case. This further demonstrates that using a 75% C_d reduction was too great of a reduction to model the tower fairing (noted in the previous section). In addition to the issues of the predicting magnitude of the cycle-averaged wake effects for a given ψ (solid lines) the steady model is incapable of predicting the unsteady variations about this cycle-average (individual data points) experimentally on the order of ± 50%) or modeling the asymmetry of the wake.

Figure 10, shows the summary for the normal force coefficient, measured at r/R=0.63. From the UC case at high U_∞, it is clear that the tower shadow is not the sole cause for variation in C_n. It is likely that the low tip speed ratios cause a high amount of unsteady separation which contributes to the variation in C_n. The downwind cases show a larger range than the corresponding upwind cases but this relative increase becomes secondary to unsteady aerodynamic effects at higher speeds. The aligned fairing (DF0) only slightly reduces the spread of the normal force coefficient, possibly because the tower shadow is only a secondary contributor of unsteadiness to the primary causes of separation and stall. FAST again under-predicts the range of variation in both the upwind and downwind cases, and this prediction is particularly poor at high U_∞.

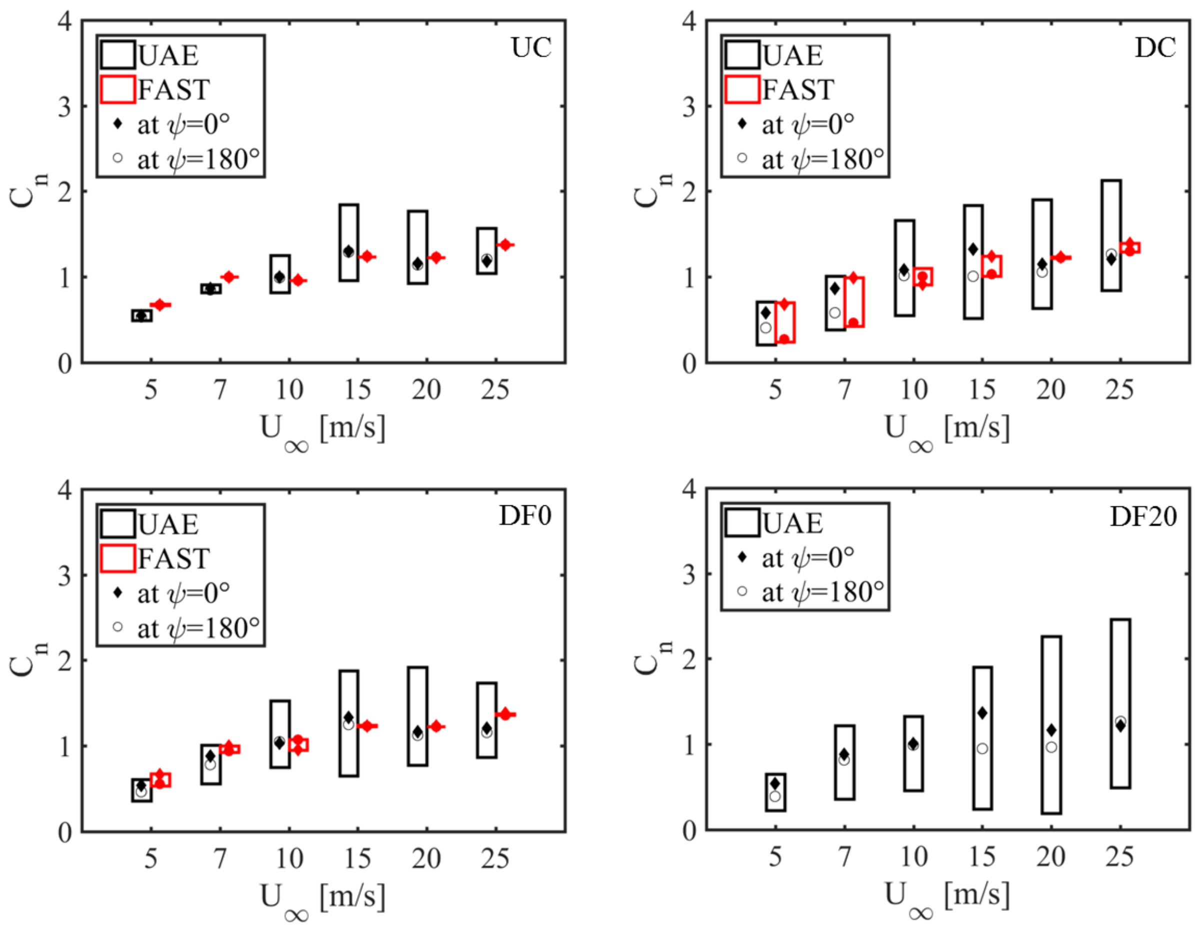

Figure 10. Normal force coefficient at r/R=0.63 using same symbol representation as in Fig. 6.

3.3 Effect on Blade Bending

Figure 11, shows root flap bending moment plotted against azimuth angle. There is an average offset between the upwind and downwind cases, of about 1 kN·m. This offset is attributed to the differences in the relative coning angle for the rotors. In particular, the upwind rotor has no coning but the downwind rotors have a downwind coning of 3.4°. This coning leads to a negative M, due to centrifugal loading countering the positive thrust loads. All the downwind cases show oscillation in the moment at a rate of 6/rev, which is attributed to the natural structural frequency associated with flapwise stiffness of the blade being excited by the tower shadow.

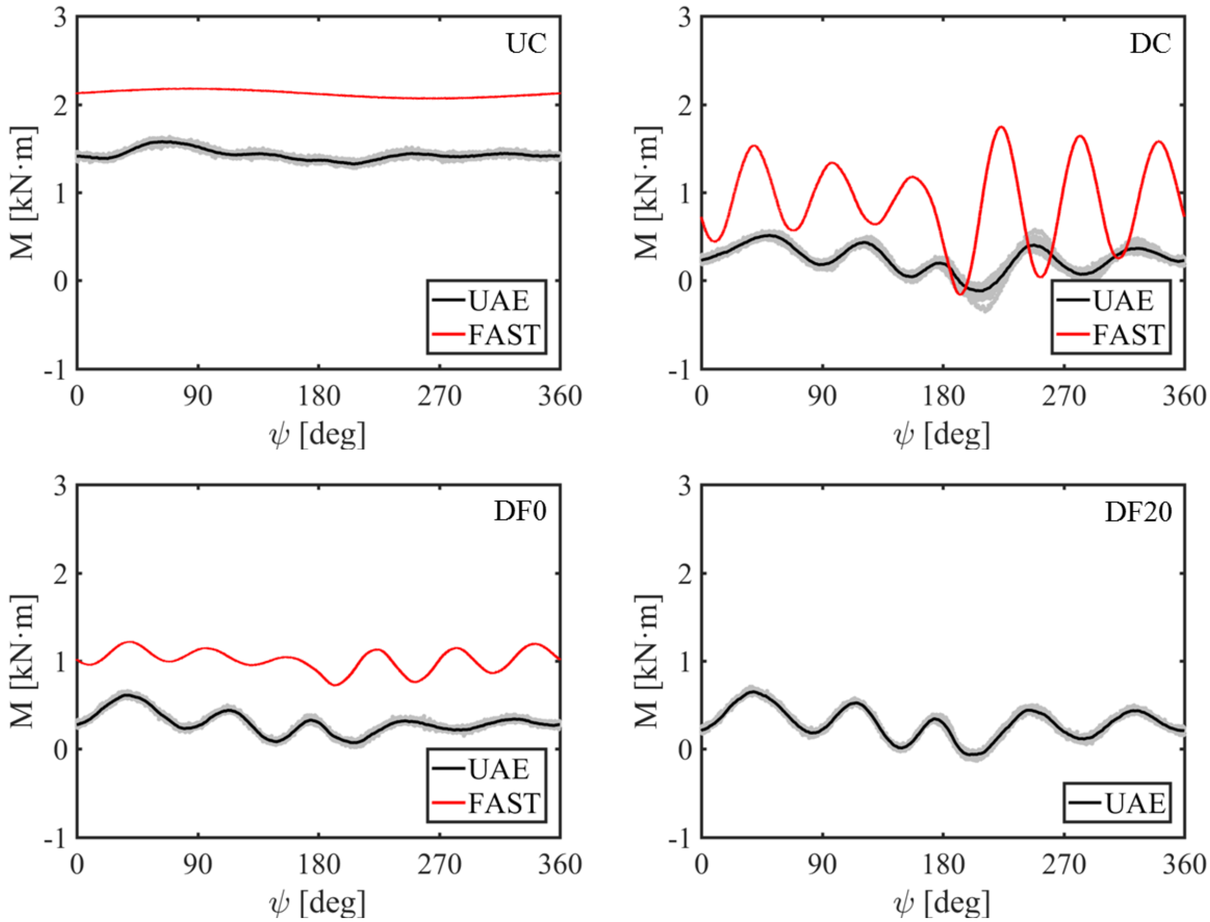

Figure 11. Root flap bending moment as function of azimuthal angle at $U_\infty = 7$ m/s using same symbol representation as in Fig. 5.

It is quite interesting that the tower shadow effect for M (which is integrated over the blade span and depends more strongly on blade dynamics and aeroelasticity) differs substantially from the effect LFA, V_r and C_n previously analyzed (which are primarily associated with local flow features). For the bending moment of the downwind cases, there is no sharp drop in bending load centered at ψ~180°. Instead, the shadow effect appears to be an impulse (with a negative sign) at ψ=180°, resulting in under-damped oscillations. For the DC case, the magnitude of the oscillations is increased by about four-fold compared with the UC case, indicating that the tower shadow effect can substantially increase blade bending loads and therefore the potential for fatigue failure. The fairing reduces the magnitude of the fluctuations by about 50%, whereas the DF20 case shows no improvement over the (unfaired) cylindrical (DC) case.

As was the case with the normal force coefficient, FAST over-predicts the average root flap bending moment in all cases, likely for the same reasons as described for the blade normal force. In the downwind cases, the simulation captures the 6/rev oscillations. The tower shadow model over-predicts the impact on the bending moment for the DC case by about two-fold, but matches well with the DF0 case.

Figure 12, shows the summary of the root flap bending moment. This is perhaps the most important result since the mean and unsteady bending moment is most closely linked to fatigue and structural failure for a given blade design. To see the effect of tower shadow, one may compare bending moment from a downwind case with the corresponding UC case for a given tunnel speed. At low U_∞, the upwind case (UC) has a smaller moment range than the corresponding downwind cases and the DF0 case performs better than then DC or DF20 case. However, at higher U_∞, the UC, DC and DF0 cases tend to perform similarly, though the DF20 case has a much larger range. This indicates the UAE rotor yields high (unwanted) root flap bending moment fluctuations, which can be further exacerbated with fairing misalignment. In terms of predictive capability for the upwind (UC) case, the simulation predicts the cycle-average values well at the higher U_∞ values but over-predicts at the lower speeds. The simulation strongly under-predicts the range of bending loads measured for the UC cases, but is qualitatively consistent for the DC case, despite poor predictions of the ranges of aerodynamic forces by FAST (Figs. 10), these don't seem to translate to as extreme ranges in bending loads. This indicates that FAST can be used to qualitatively predict the effects of tower shadow on bending moment for the reported UAE configurations, despite not capturing the flow physics. This ability to qualitatively predict moments may due to the counter-acting effects of a steady tower wake model (which misses the incoming flow angle variations) coupled with a quasi-steady blade aerodynamic model (which over-predicts changes in the aerodynamic sensitivity in conditions where wake and aerodynamic time scaled are coupled), all coupled with the span-wise and inertia integrating effects of the bending moment. As such, it is difficult to determine, whether such qualitative predictions of the bending moment by FAST would translate to more modern and larger rotor systems. In addition, it should be noted that FAST does not predict the bending moment ranges for the faired tower configurations.

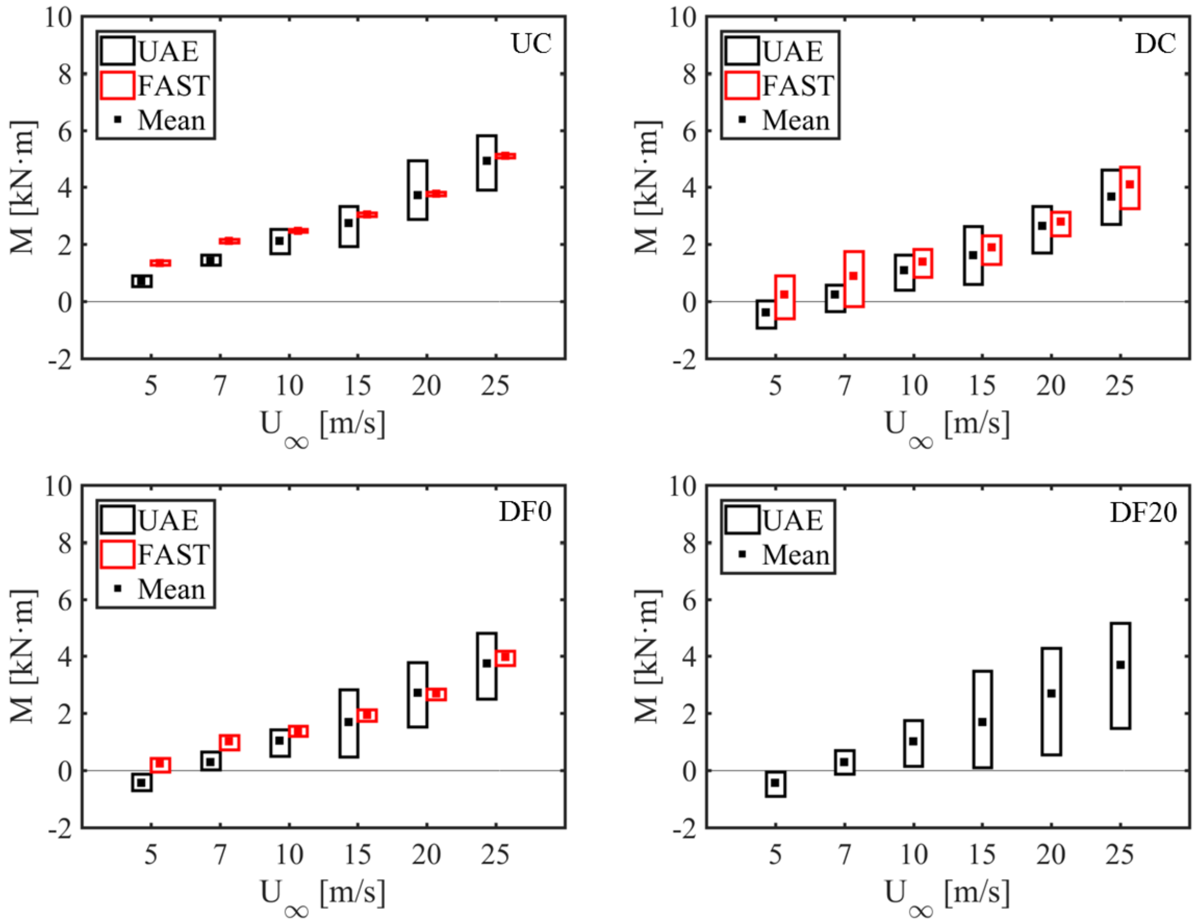

Figure 12. Average (square) and range (box) of root flap bending moment where the time-averaged data are given by the solid square (■) and the range of all instantaneous values for a given wind speed is identified the encompassing box (□).

4. Conclusions

The first objective of this study was to investigate the effects of tower shadow on the flow seen by the blade as well as the blade forces and moments. At low freestream velocities (high tip speed ratios), there was a pronounced tower shadow effect on the resultant flow angle deficit and fluctuations but a relatively weak influence on resultant velocity magnitude seen by the blade. The flow angle effects translated to distinct effects on the normal force coefficient, and blade bending moments. The flow-aligned fairing reduced the tower shadow effects on the resultant flow field, leading to a reduced effect on the normal force coefficient. However, the fairing misaligned with the flow by 20° did not reduce shadow effects at any speed. At high upstream velocities (low tip speed ratios), unsteady spatially-distributed aerodynamic interactions dominated the chord-wise and span-wise characteristics more than tower shadow effects. This led to high bending moments, especially for the misaligned fairing at the lowest tip speed ratio. However, at high tip speed ratios, the aligned tower fairing substantially mitigated bending moment variations (compared to a cylindrical tower) by reducing the cycle-averaged flow angle deficit and more importantly by reducing the instantaneous flow angle variations about the cycle-average. As such, fairing concept can be considered an option to mitigate tower shower effects, but that its benefits may be eliminated if the flow is misaligned by about 20 degrees.

The second objective of this study was to investigate capability of the steady tower shadow model utilized by FAST and other simulators to predict these effects. The simulation model of the UAE simulated some aspects of the experiment accurately. Despite significant aerodynamic simplifications, the simulation reasonably models the cycle-averaged values of the flow field seen by the blade at a given azimuthal angle, away from the tower shadow region. Inside the wake region, the steady wake cannot predict the highly unsteady variations in flow angles, since the model neglects vortex shedding. The wake model lead to substantial over-predictions of the cycle-averaged effect on normal force coefficient by about 100% at the high tip speed ratios. Despite these failings, the steady tower shadow model lead to qualitatively reasonable predictions of bending moment. This may be attributed to the counter-acting effects of a steady tower wake model (which misses the incoming flow angle variations) coupled with a quasi-steady blade aerodynamic model (which over-predicts aerodynamic variations as it does not account for wake time-scales on the order of aerodynamic time-scale), all coupled with the span-wise and inertia integrating effects of the bending moment. As such, it is not clear whether FAST and other turbine simulators can be expected to qualitatively predict tower shadow effects for modern and larger rotor systems, especially for faired tower configurations.

Recommended future experimental work includes investigating the tower shadow effects for a downwind rotor in field conditions with cylindrical tower and for a lightweight self-aligning fairing, to determine if this can allow a net positive mitigation of the shadow effects. To improve predictive computational ability for the instantaneous values and the range of bending moments, FAST should incorporate unsteadiness in the wake model to reflect vortex shedding physics (in terms of both velocity magnitude and angle fluctuations) and to reflect aerodynamic hysteresis associated with blade-wake interaction. Once understood, this interaction could be incorporated into FAST for an even more physically realistic model.

References

Quarton, D. C. "The evolution of wind turbine design analysis—a twenty year progress review." *Wind Energy* 1.S1 (1998): 5-24.

Shikha, Bhatti, T., & Kothari, D. (2003). Aspects of Technological Development of Wind Turbines. *Journal of Energy Engineering*, *129*(3), 81–95. https://doi.org/10.1061/(ASCE)0733-9402(2003)129:3(81)

Griffith, D. Todd, and Thomas D. Ashwill. "The Sandia 100-meter all-glass baseline wind turbine blade: SNL100-00." *Sandia National Laboratories, Albuquerque, Report No. SAND2011-3779* (2011).

Bak, Christian, et al. "Light Rotor: The 10-MW reference wind turbine." *EWEA 2012-European Wind Energy Conference & Exhibition*. 2012.

Kim, Taeseong, Torben J. Larsen, and Anders Yde. "Investigation of potential extreme load reduction for a two-bladed upwind turbine with partial pitch." *Wind Energy* 18.8 (2015): 1403-1419.

Veers, Paul S., et al. "Trends in the design, manufacture and evaluation of wind turbine blades." *Wind Energy* 6.3 (2003): 245-259.

Nielsen, Kristian H. "Technological trajectories in the making: two case studies from the contemporary history of wind power." *Centaurus* 52.3 (2010): 175-205.

Qin, Chao, Eric Loth, Sang Lee, and Patrick J. Moriarty. "Blade Load Reduction for a 13 MW Downwind Pre-Aligned Rotor." In *34th Wind Energy Symposium*, p. 1264. 2016.

Loth, Eric, et al. "Segmented ultralight pre-aligned rotor for extreme-scale wind turbines." *50th AIAA Aerospace Sciences Meeting including the New Horizons Forum and Aerospace Exposition*. Nashville, Tennessee: AIAA, 2012.

Ichter, Brian, et al. "A morphing downwind-aligned rotor concept based on a 13-MW wind turbine." *Wind Energy* 19.4 (2016): 625-637.

Noyes, Carlos, Chao Qin, and Eric Loth. "Pre-aligned downwind rotor for a 13.2 MW wind turbine." *Renewable Energy* 116 (2018): 749-754.

Leishman, J. Gordon. "Challenges in modelling the unsteady aerodynamics of wind turbines." *Wind energy* 5.2-3 (2002): 85-132.

Zahle, Frederik, Helge Aagaard Madsen, and Niels N. Sørensen. "Evaluation of tower shadow effects on various wind turbine concepts." *Risoe*. Danmarks Tekniske Universitet, Risø Nationallaboratoriet for Bæredygtig Energi, 2009. 11-29.

Yoshida, Shigeo, and Soichiro Kiyoki. "Load equivalent tower shadow modeling for downwind turbines." *Nippon Kikai Gakkai Ronbunshu B Hen(Transactions of the Japan Society of Mechanical Engineers Part B)(Japan)* 19.6 (2007): 1273-1279.

Madsen, Helge Aagaard. "Low frequency noise from wind turbines mechanisms of generation and its modelling." *Journal of Low Frequency Noise, Vibration and Active Control* 29.4 (2010): 239-251.

Koh, J. H., and E. Y. K. Ng. "Downwind offshore wind turbines: Opportunities, trends and technical challenges." *Renewable and Sustainable Energy Reviews* 54 (2016): 797-808.

O'Connor, Kyle, Eric Loth, and Michael S. Selig. "Design of a 2-D fairing for a wind turbine tower." *31st AIAA Applied Aerodynamics Conference*. 2013.

Orlando, Stephen, Adam Bale, and David A. Johnson. "Experimental study of the effect of tower shadow on anemometer readings." *Journal of Wind Engineering and Industrial Aerodynamics* 99.1 (2011): 1-6.

Hand, M. M., et al. *Unsteady aerodynamics experiment phase VI: wind tunnel test configurations and available data campaigns*. No. NREL/TP-500-29955. National Renewable Energy Lab., Golden, CO.(US), 2001.

Blevins, Robert D. "Applied fluid dynamics handbook." *New York, Van Nostrand Reinhold Co., 1984, 568 p.* (1984).

O'Connor, Kyle, (2014). "Development and Testing of a Fairing for a Wind Turbine Tower." (Unpublished master’s thesis). University of Virginia, Charlottesville, Va.

Wang, Tongguang, and Frank N. Coton. "A high resolution tower shadow model for downwind wind turbines." *Journal of Wind Engineering and Industrial Aerodynamics* 89.10 (2001): 873-892.

Wang, Tongguang, and Frank N. Coton. "An unsteady aerodynamic model for HAWT performance including tower shadow effects." *Wind Engineering* (1999): 255-268.

Munduate, Xabier, Frank N. Coton, and Roderick A. McD Galbraith. "An investigation of the aerodynamic response of a wind turbine blade to tower shadow." *Journal of Solar Energy Engineering(Transactions of the ASME)* 126.4 (2004): 1034-1040.

Zahle, Frederik, Niels N. Sørensen, and Jeppe Johansen. "Wind turbine rotor-tower interaction using an incompressible overset grid method." *Wind Energy* 12.6 (2009): 594-619.

Jonkman, Jason Mark, and Marshall L. Buhl Jr. *FAST User's Guide-Updated August 2005*. No. NREL/TP-500-38230. National Renewable Energy Laboratory (NREL), Golden, CO., 2005.

Garrad Hassan: Bladed Theory Manual. Version 4.5. Bristol. England: Garrad Hassan, 2013

Powles, S. R. J. "The effects of tower shadow on the dynamics of a horizontal-axis wind turbine." *Wind Engineering*(1983): 26-42.

Moriarty, Patrick J., and A. Craig Hansen. *AeroDyn theory manual*. No. NREL/TP-500-36881. National Renewable Energy Lab., Golden, CO (US), 2005.

Calkins, D. E. "Two-dimensional hydrodynamic characteristics of a bluff symmetrical fairing section." *AIAA journal* 22.9 (1984): 1216-1221.

Reiso, Marit, Torbjørn Ruud Hagen, and Michael Muskulus. "A calibration method for downwind wake models accounting for the unsteady behaviour of the wind turbine tower shadow behind monopile and truss towers." *Journal of Wind Engineering and Industrial Aerodynamics* 121 (2013): 29-38.

Sant, Tonio, Gijs van Kuik, and G. J. W. Van Bussel. "Estimating the angle of attack from blade pressure measurements on the NREL phase VI rotor using a free wake vortex model: axial conditions." *Wind Energy* 9.6 (2006): 549-577.

Chapter 4

Tower Shadow for an Extreme-Scale Downwind Turbine

Abstract

As wind turbine size increases so does the interest in the downwind rotor configuration, since they can provide a structural advantage for blade loads as compared to an upwind design. However, tower shadow, the blades passing through the tower wake, has long been a concern for downwind systems. The tower shadow negatively affects the blade by introducing a load impulse during the wake passage. An aerodynamic fairing could shroud the tower reducing the wake deficit and thus the load fluctuation effect of the tower shadow. However, there is no clear consensus on the importance of a tower shadow and of a fairing for large utility-scale wind turbines. Simulations were conducted in FAST to quantify the effect of tower shadow for a 13.2 MW downwind turbine. Two cases were analyzed: steady wind conditions (e.g. wind tunnel experiment) and turbulent wind conditions (e.g. operating conditions). Under steady wind conditions, the tower shadow had a significant effect on predicted blade loads, increasing the Damage Equivalent Loading (DEL) by 70%. In this case, a tower fairing can reduce this impact by more than 75%. However, conditions with atmospheric turbulence were much less sensitive to tower shadow, and the predicted DEL decrease with a tower fairing was only 3%. These results indicate that a tower fairing can be important for low turbulence (e.g. wind tunnel) testing conditions but that an extreme-scale downwind turbine in field turbulence does not suffer significantly from tower shadow and does not benefit significantly from a tower fairing. Instead, the highest unsteady load fluctuations are due to atmospheric turbulence.

1. Introduction

1.1 Downwind Turbines

Wind turbines have increased in size consistently over the past several decades due to increased power capture (Polinder et al. 2013; Veers et al. 2003; Blaabjerg & Ma, 2013). For a variable speed wind turbine, the power that may be captured is proportional to the rotor swept area and the wind speed cubed. Larger wind turbines have larger radii and reach higher into the atmosphere where the wind is stronger to allow an increase in power production per cost of the system. Thus, as in most industrial trends, the increase in turbine size is primarily driven by economic aspects.

However, the increases in power generation are accompanied with an increase in blade loads. For conventional designs, there is expected to be a limit where the increase in power no longer justifies the increased cost of a larger rotor. Innovations that can reduce loads can allow for larger turbines, which generate more power and still allow for a decreased cost of wind energy. One such innovation is the downwind load-aligned wind turbine (Noyes *et al.* 2018a; Loth *et al.* 2017; Crawford & Platts, 2008; Eggers *et al.* 2005; Pavese *et al.* 2017). Downwind indicates the rotor is positioned downstream of the tower. Load-aligned indicates the rotor uses downwind coning to create a centrifugal moment that counters the thrust moment. Because the two moments act in opposite directions the resultant out of plane moment is much lower than it would have been with a flat rotor. This load reduction benefit is only significantly realized for extreme-scale wind turbines, with rated powers exceeding 10 MW, since relative thrust loads are much stronger for these large scales. As such, downwind rotors are becoming a more attractive rotor for future wind turbine design.

However, downwind rotors are not a new invention. The first megawatt-scale wind turbine, the Smith-Putnam wind turbine in 1943, used a downwind configuration (Vargo, 1974). More recently, in 2016 Hitachi (Japanese) built a 5 MW, offshore, downwind turbine prototype. Ming Yang (Chinese) and Aerodyn (German) in 2014 built a 6 MW, 2-bladed, downwind prototype (De Vries, 2016).

A primary reason that upwind turbines have been preferred over the downwind design is the "tower shadow" effect. This effect occurs when the downwind rotor blades pass through the turbulent wake of the tower. This can be undesirable acoustically as the tower shadow can produce a loud "thumping" noise at high operational wind speeds. This sound, which can travel far, is undesirable for onshore turbines (Butterfield *et al*, 2007). Additionally, there is a common concern that the tower shadow can destructively affect the blades because of the periodic unloading the blade receives every rotation when passing through the tower wake. This could significantly decrease the fatigue life of the blade. The tower shadow complications (acoustic and loading) have led nearly all manufactures to pursue upwind designs for the past four decades. However, as turbine size increases, the thrust loads become more difficult to manage so that there are more significant benefits (blade load-reduction and tower clearance) of downwind coning designs. This has caused researchers to reinvestigating the question of tower shadow (Wang & Coton, 2001, Leishman, 2002; Zahle *et al.* 2009; Reiso *et al.* 2013).

1.2 Tower Shadow Models

As interest in downwind turbines grows, so also do the methods of simulating the tower shadow (Fig. 1). Tower shadow is a complicated phenomenon because it is a complex flow structure interaction, involving the unsteady wake of a tower and the unsteady aerodynamic and structural response of a rotor. Some of the basic aerodynamic features can be addressed with unsteady Computational Fluid Dynamic (CFD) tools which have been developed to simulate the interaction (Zahle *et al.* 2009; Yoshida & Kiyoki, 2007). These CFD tools have not progressed to the point whereby they can predict the structural aeroelastic response and damage equivalent loads due to tower shadow for a field conditions with atmospheric turbulence. Instead, analytical models of the tower wake have been proposed (Moriarty & Hansen, 2005; Hand & Cashman, 2018) and incorporated into aeroelastic turbine system simulation packages, such as FAST (Jonkman & Buhl, 2005).

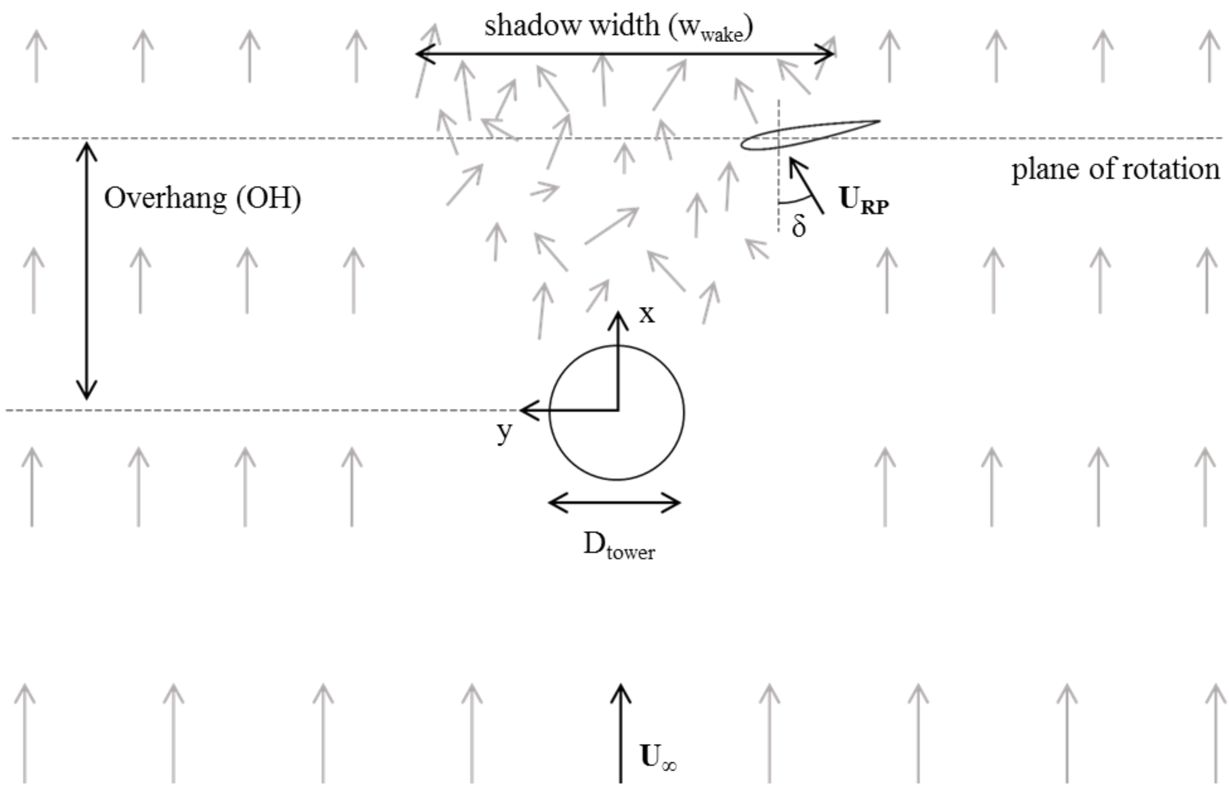

Figure 1. Schematic of a blade cross section of a downwind turbine passing through a turbulent wake of the tower. The magnitude and direction of the wind at the rotor plane (U_{RP}) are a function of space and time.

The simplest and most widely used method for tower wake for such aeroelastic codes is a velocity deficit model based on work by Powles (1983). The model subtracts a steady streamwise velocity deficit, based on tower drag, from the oncoming wind that the blade element will see. This deficit is distributed over the shadow width (w_{wake}) as shown in Fig. 1. Equation 1, defines this deficit as the streamwise velocity lost inside the wake (u_{wake}), which is a function of the diameter of the tower (D_{tower}), the drag coefficient of the tower (C_d), the shadow width (w_{wake}), and the free stream velocity (U_∞) as

$$\frac{u_{wake}}{U_\infty} = \frac{D_{tower} \cdot C_d}{\mathrm{w_{wake}}} \cos^2\left(\frac{y}{\mathrm{w_{wake}}}\pi\right) \tag{1a}$$

$$\left(\frac{\mathrm{w}_{wake}}{D_{tower}}\right)^4 - 4\left(\frac{\mathrm{w}_{wake}}{D_{tower}}\right)^2 = 16\left(\frac{x}{D_{tower}}\right)^2 \tag{1b}$$

The model ignores the unsteady fluctuations (both in magnitude and direction) that are characteristic of a turbulent wake. Work has been done to improve upon this steady wake model by adding an unsteady component (Reiso *et al.* 2013; Yoshida & Kiyoki, 2007; Munduate *et al.* 2004).

1.3 Tower Fairing

Because the tower shadow effect is a primary reason there are so few downwind turbines, there has been some previous work has been done to reduce/eliminate tower shadow. Passive flow control methods have been suggested (Snyder & Wentz, 1981), as has an aerodynamic tower fairing (Fig. 2) that could reduce the circular cylinder drag, and consequently the tower wake, by roughly 75% (O'Connor *et al.* 2015; Noyes & Loth, 2017). The fairing can be design as a lightweight structure that can rotate about a fixed tower, with an aerodynamic design such that it is self-aligning like a weather vane (O'Connor *et al.* 2015). However, there are complications with employing such an aerodynamic fairing. The trailing edge of the fairing may encroach into the rotor-clearance region. In addition, if the wind changes direction more rapidly than the fairing can realign there will be a period when the fairing is operating under high angles of attack. In addition, there is a question as to whether load reductions yielded by fairing are large enough to merit the cost and complexity of adding the fairing to the turbine system (Koh & Ng, 2016).

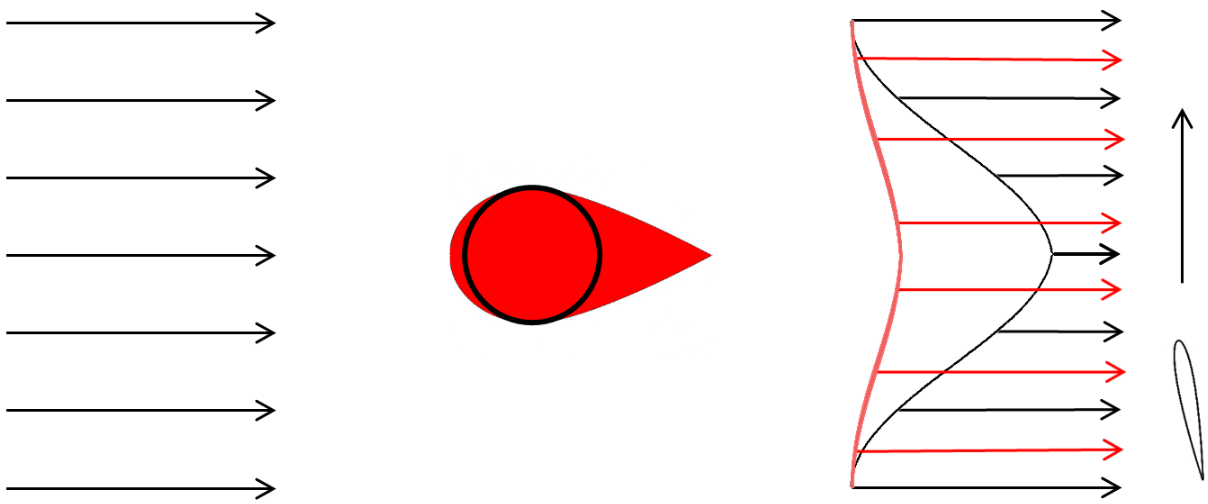

Figure 2. Steady velocity deficit wake model of a tower with (red) and without (black) a tower fairing.

1.4 Project Objectives

The objective of this study is to determine if the tower shadow effect is sufficiently significant to justify the use of a tower fairing for extreme-scale downwind turbines. An extreme-scale wind turbine will be selected and defined for analysis. The effect of tower shadow will be approximated using validated simulation tools. Both ideal steady wind conditions (typical of wind tunnel testing) and more realistic turbulent wind (typical of actual field operations) will be considered. This is the first study that simulates and quantifies the effect of tower shadow on blade aerodynamics and loading, in both steady and turbulent wind conditions for an extreme-scale downwind turbine. It is also the first to consider the potential aerodynamic impact of a tower fairing on the blade moments and damage equivalent loads for an extreme-scale downwind turbine. As such, this study is thus uniquely posited to answer the important questions of whether tower shadow is a major issue for extreme-scale downwind turbine, and whether a tower fairing can significantly reduce blade load fluctuations. Given the rapid increase of interest in extreme-scale turbines and in downwind turbines, the answers to these questions are critical to future wind turbine design.

2. Methodology

2.1 Turbine Description

The extreme-scale turbine selected for the analysis was the SUMR13 turbine (Ananda *et al.* 2018). This 13.2MW downwind turbine, employs the load-aligned concept by means of a morphing hinge (in the flapwise direction) to adjust coning angle as a function of wind speed. As a result, SUMR13 has a rotor mass that is 25% less than that of a conventional wind turbine of the same rated power. However, for simplicity in this study, the coning angle was set statically at the nominal value of 12.5° since this was the angle used between rated and cut-out conditions, where the tower shadow effect is the strongest. Some general parameters of the wind turbine are shown in Table 1.

Table 1. SUMR13 turbine parameters.

Rated Power	13.2 MW
Rated Wind Speed	11.3 m/s
IEC Wind Condition	Class IIB
Rated Rotational Rate	9.54 rpm
Blade Number	2
Blade Length	104.3 m
Coning Angle	12.5°
Hub Height	142.4 m
Hub Radius	2.5 m
Overhang	8.2 m
Tower Diameter at Base	7.0 m
Tower Diameter at Hub	4.5 m
Shaft Tilt Angle	0°

2.2 Simulation Tools

The primary simulation tool used herein is FASTv8 (Jonkman & Buhl 2005), an open source code written in Fortran to simulate horizontal axis wind turbines. This code uses an aerodynamic module, AeroDyn15 (Jonkman & Jonkman, 2016), which is based on blade element momentum theory (BEM) BEM is used widely and has undergone rigorous experimental and computational validation (Jonkman, 2003; Krogstad & Eriksen, 2013). The momentum theory portion of BEM, is used to predict the wind velocity at the rotor plane (U_{RP}). Axial induction causes U_{RP} to be lower than the free stream wind (U_{∞}), but can be adjusted to include tower shadow using the previously defined (EQ. 1) model. For a steady inflow velocity field, the blade element theory portion of BEM takes the known velocities at the rotor plane and calculates the aerodynamic effect by simplifying the blade unto a series of 2-D elements.

However, the above approach can be modified to include atmospheric turbulence using TurbSim (Jonkman, 2009) as an input to FAST, to further modify the velocity distribution in the rotor plane. The turbulent model used is the Kaimal model with turbulence level “B” in accordance with the IEC standards (IEC, 2005). The wind field grid size used herein is 25 x 25 with an element size of 11.5m x 11.5m. For each wind speed, turbulent simulations are run 6 times with different numerically generated 11-minute wind fields. Aerodynamic channels are taken at a non-dimensional spanwise location of 70%, selected as the radial value that roughly separates the swept area in half. Wind speed channels are taken at the hub height.

Using these velocity fields and models for the rotor aeroelastic characteristics, FAST output aerodynamic and structural data. The aerodynamic output channels of particular interest (shown in Fig. 3) are dynamic pressure (q) which is used to calculate resultant velocity (V_R) with Eq. 2 (ρ is the density of air), angle of attack (α), normal force coefficient (C_n) and root flapwise bending load (M). Root flapwise bending moment is defined as the moment about the chord line at 0° twist and rotates with pitch.

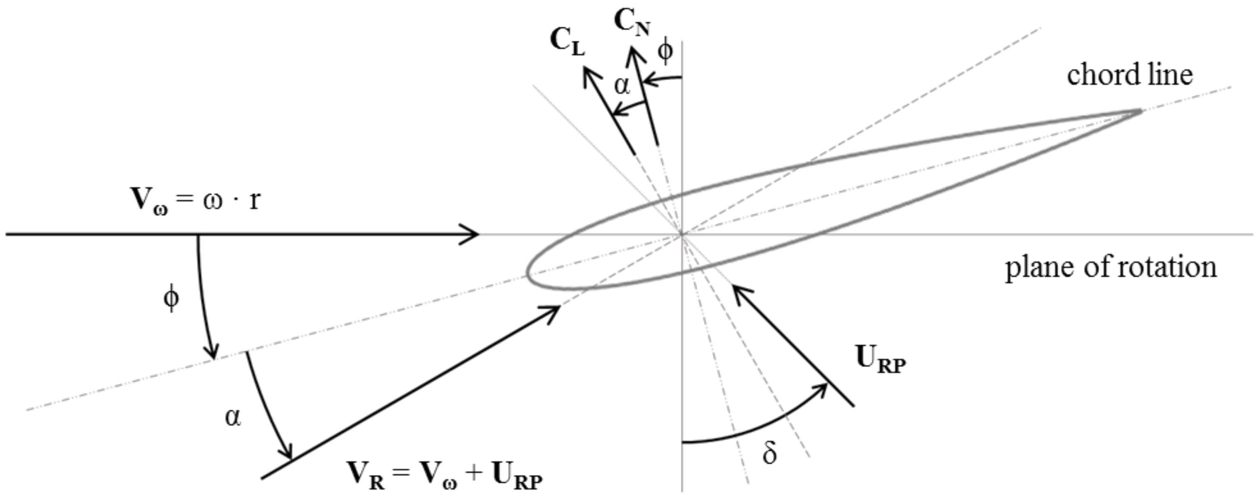

Figure 3. Aerodynamics of a blade element in a rotation reference frame with non-zero wind deflection angle (δ) due to tower shadow effects.

$$V_R = \sqrt{2q\rho} \tag{2}$$

Depending on the level of turbulence, large values of δ can be experienced. Although the tower shadow model in FAST includes a small steady value of δ based on potential flow, it does not include the unsteady δ variations from large scale vortex shedding or small scale turbulence. This can be seen as a limitation of the Powles tower shadow model. To examine this, experimental data from the UAE phase VI turbine were compared to FAST simulation of the same experiment (Noyes *et al. 2018b*; Hand *et al.* 2001). A subset of that experiment is shown in Fig. 4. Panel A shows the aerodynamic response, panel B shows the bending moment at a single wind speed, and panel C shows bending moment mean and range over a range of wind speeds. As shown in Panel C, FAST reasonably predicts the effect of tower shadow on mean moments for moderate to high wind speeds (U_∞ in the range of 10-25 m/s). This suggests that using the Powles model is reasonable at approximating the tower shadow effect on the mean moment but fails at capturing the instantaneous values and the strength of the fluctuations.

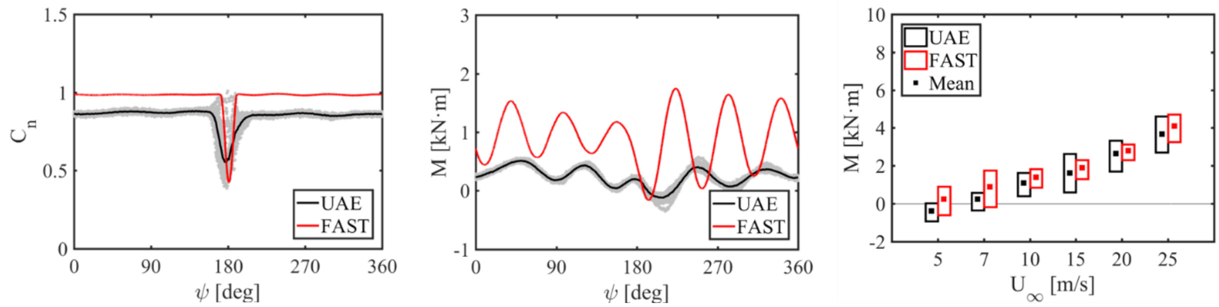

Figure 4. Response of the UAE rotor based on experimental data (black) and simulated data (red) for: A) normal force coefficient at U_∞=7 m/s as a function of azimuthal angle, B) root flapwise bending moment at U_∞=7 m/s as function of same angle, & C) average and range of root flapwise bending moment as a function of incoming wind speed.

Another post-processing code available with FAST is MLife (Hayman & Buhl, 2012) which considers the moment acting on the blade. MLife is a code that uses a rain flow counting algorithm to take a time series data input and return damage equivalent load (DEL). DEL is defined as the amplitude of a zero-mean, 1 Hz sinusoidal signal that would result in the same amount of fatigue damage. DEL is calculated using the time series of this moment. The statistical data (max, mean, min and DEL) are calculated using the last 10 minutes of data from all 6 simulations, as is standard practice. It should be noted that Reiso & Muskulus (2014) indicated that the large scale vortex shedding (not included in Powles model) accounts for only about 3% of the DEL of the tower shadow. As such, the present approach is deemed reasonable.

3. Results

3.1 Steady Wind Conditions

The tower shadow directly affects the flow field though which the blade passes. This affected flow field leads to an alteration of the blade's aerodynamic forces. Figure 5, displays the effect of tower shadow on the SUMR13 at the steady rated wind condition of 11.3 m/s. The blue line represents simulations that did not use the tower shadow model, while the red line represents the simulations that included the tower shadow model. The difference between the two lines is entirely due to tower shadow effects. This color scheme will be used throughout the entirety of this chapter. All aerodynamic channels, panels B-D, are taken at 70% spanwise location. Panel B, shows the angle of attack over one rotation. There is only a minor change in angle of attack without tower shadow effects, however inclusion of the show effect leads to a sharp decrease as the blade passes through the tower wake. The resulting angle of attack decreases by about 50% through the tower shadow. In contrast, there is only a small change in the resultant velocity (panel C) between the two simulations. To quantify this impact on velocity magnitude, the variation of the resultant velocity over one revolution was determined to be approximately 2% without tower shadow and approximately 2.5% with the tower shadow. Panel D, displays how both the combined effects of angle of attack and resultant velocity impact the normal force coefficient. The tower shadow adds a sharp negative impulse, with a magnitude of about 17% the average load, to an otherwise smooth signal.

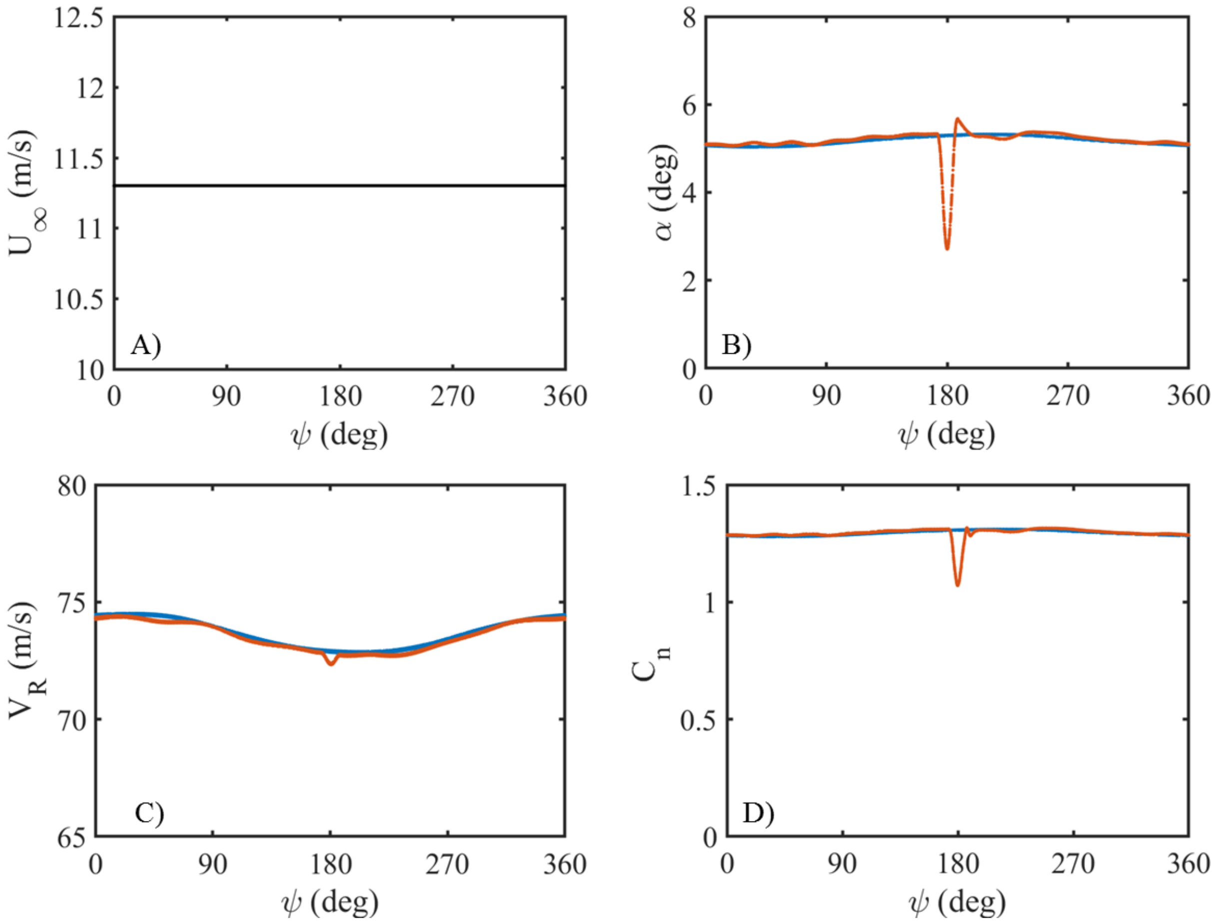

Figure 5. Aerodynamic response of the SUMR13 rotor at 70% spanwise location operating at steady rated wind including (red) and excluding (blue) tower shadow model: A) steady wind profile, B) angle of attack, C) resultant velocity & D) normal force coefficient.

From a structural viewpoint, the root flapwise bending moment is important because much of the blade design is aimed at supporting this cantilever load. This moment is often the design driver for both the ultimate strength and the fatigue strength of the blade. Figure 6, shows the bending moment for SUMR13 as predicted by FAST, with and without tower shadow effect. Panel A shows the raw data for a single simulation. The baseline (blue line) bending moment oscillates at a 1-P frequency due to the gravitational load. This is a result of a coned rotor and can be mitigated by using a teeter hinge because this is a two-bladed system. Once the shadow effect is included (red line), there is a pronounced negative impulse on moment as the rotor passes through the wake. The tower shadow impulse is about equal to 50% of the baseline range. Panel B shows statistics (maximum & minimum and mean) for simulations with wind speeds ranging from 25% to 200% of the rated wind speed. In general, the root flapwise bending load is greatly dependent on wind speed with the greatest loads occur at rated conditions for both conditions with and without tower shadow. For no tower shadow, the range of moments is relatively constant over wind speeds and the mean moment is effectively the average of the minimum and maximum values. With the inclusion of tower shadow (red), the mean and maximum values are largely unaffected, however the minimum value decreases significantly. Thus, tower shadow for this extreme-scale wind turbine in steady winds only affects the range of moments and not the average, as is also the case for gravitational force.

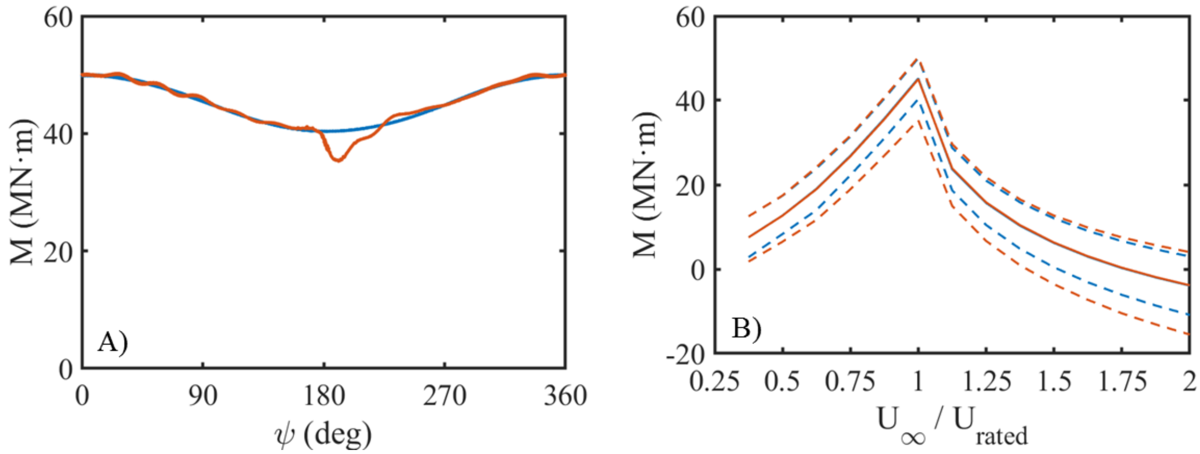

Figure 6. Root flapwise bending moment including (red) and excluding (blue) tower shadow model for A) at steady rated conditions vs. azimuth angle & B) mean (solid line) and maximum/minimum (dashed line) over range of steady wind speeds.

3.2 Turbulent Wind Conditions

Unfortunately, field-deployed turbines will not experience steady wind conditions during operation; instead, the wind condition can contain significant turbulence. The turbine was simulated over the entire range of nominal wind speeds (2.8 – 22.6 m/s) using turbulent wind fields as described in the methods section above. The same convention as previously defined was used: red includes the tower shadow model and blue excludes the model.

A single rotation of a single simulation taken at nominal wind speed equal to 11.3 m/s is shown in Fig. 7. Panel A shows the streamwise component of the free stream wind at a point upstream of the center of the rotor. There are large fluctuations of wind speed over a single rotation. These wind speed fluctuations dominate the blade aerodynamics (panels B-C). Panel B shows the angle of attack corresponding to the wind field shown. As the blade passes through the tower shadow (ψ=180°) there is a noticeable dip in angle of attack, by roughly 2°. This is approximately the same decrease simulated with steady wind. However, in the turbulent case, this decrease due to the tower shadow is weak compared to the influence of turbulent fluctuations. For resultant velocity (panel C), there is no distinguishable tower shadow effect. A trend similar to that seen in angle of attack can be seen for the normal force coefficient (panel D). There is a noticeable dip of about 0.2, which is roughly the magnitude with steady wind, but the dip is generally small compared to the highly fluctuating associated with wind turbulence.

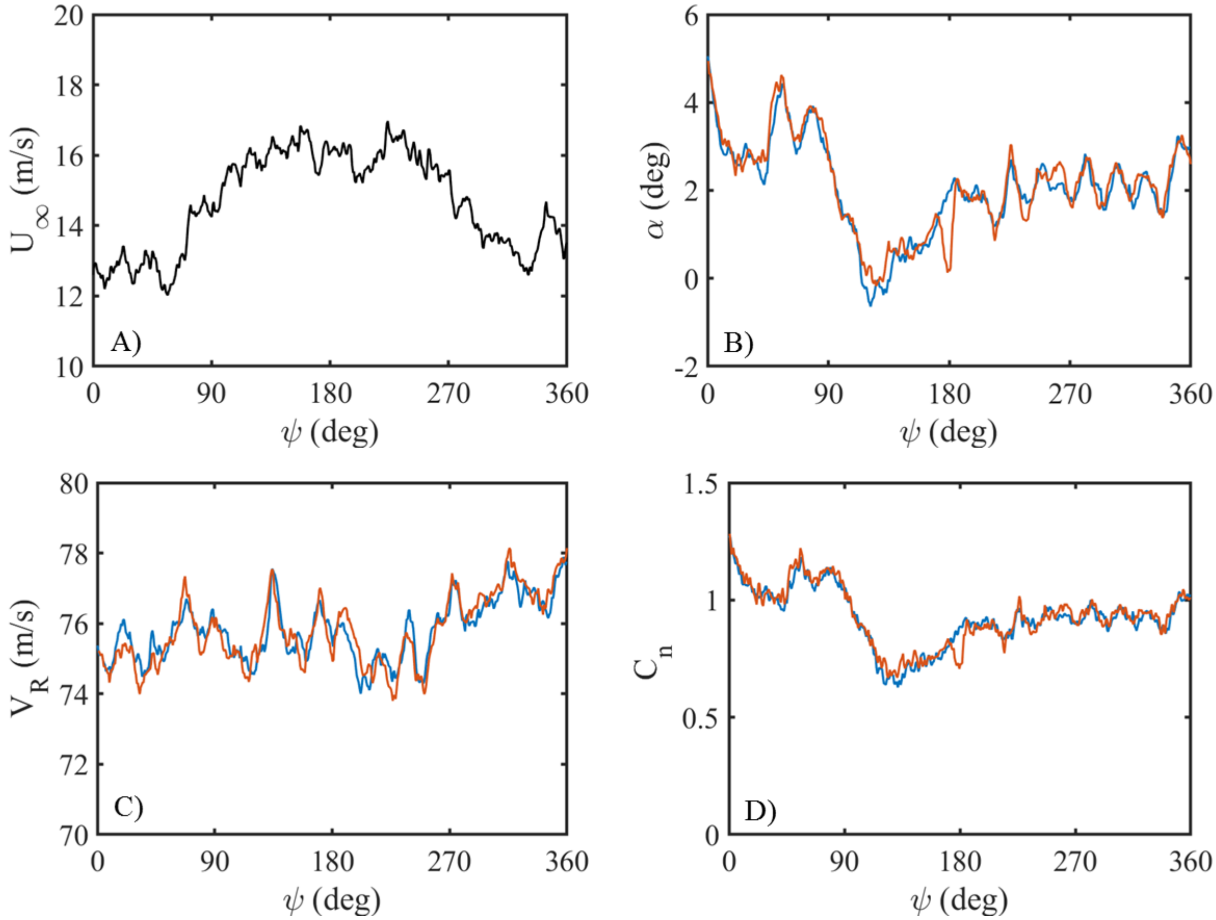

Figure 7. Aerodynamic response of the SUMR13 rotor at 70% spanwise location operating at turbulent rated wind including (red) and excluding (blue) tower shadow model: A) turbulent wind field, B) angle of attack, C) resultant velocity & D) normal force coefficient.

The most interesting data channel is the root flapwise bending moment. Figure 8a, shows M over a single rotation for a single simulation at rated conditions (under the same wind field shown in Fig. 7A). As the blade passes through the tower shadow, there is a noticeable dip compared with the baseline. The dip is roughly 5 MN·m in magnitude, which is equivalent to the dip simulated with the steady wind. The dip is of much smaller magnitude compared with the baseline fluctuations due to turbulence. The DEL was obtained by combining the data from all 6 simulations (for a single nominal wind speed) together and is shown in panel B. There is virtually no difference with and without tower shadow up until rated conditions, and only a very minor difference above rated conditions. As such, the tower shadow does increase the moment fluctuations and DEL but these changes are quite small compared to the changes associated with inclusion of turbulence. Therefore, tower shadow is not expected to significantly the fatigue life of a downwind rotor blade for a extreme-scale load-aligned 13.2 MW turbine. The potential impact for other downwind rotors and the potential impact of a tower fairing, are discussed in the following.

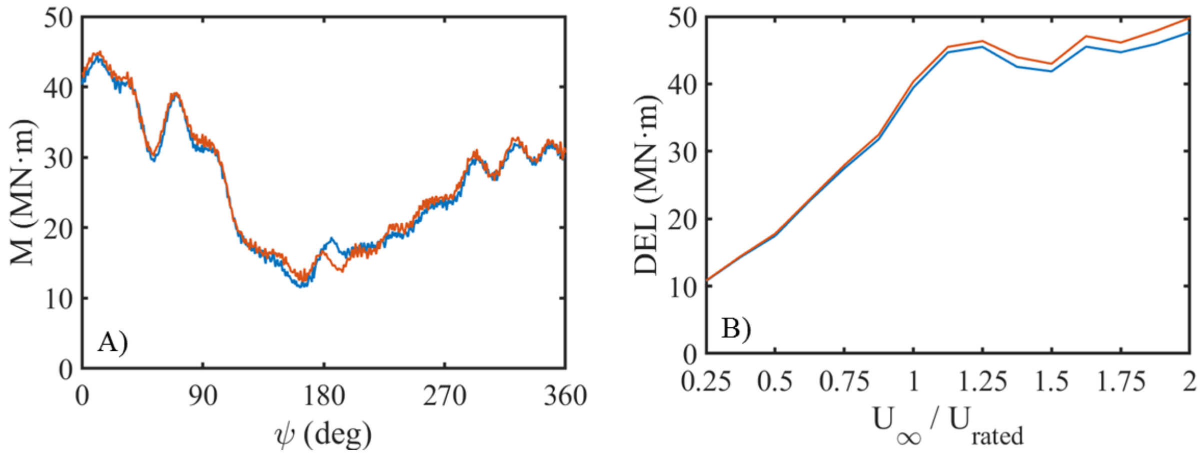

Figure 8. Turbulent response including (red) and excluding (blue) tower shadow model for: A) root flapwise bending moment vs. azimuth angle & B) damage equivalent loading over range of wind speeds.

3.3 Clearance Sensitivity

As the downstream distance relative to the rotor increases, the tower wake width increases while the velocity deficit decreases. As this distance increases, one may expect that the wake effect on blade passage is mitigated. The SUMR13 turbine has a particularly large coning angle of 12.5, and consequently a large clearance. As such, one may expect that the above results may vary depending on the blade path relative to the tower centerline. Such changes can occur, due to variations in coning angle, tilt angle and overhang distance. To determine whether the above trends are sensitive to the distance between the tower and rotor passage, simulations with varying degrees of overhang were conducted at rated wind speed for both steady and turbulent flow conditions. Figure 9 displays the damage equivalent loads as a function of non-dimensional overhang (OH* defined as rotor overhang normalized by the baseline value of 8.16m) under steady (panel A) and turbulent (panel B) wind conditions. For steady wind, it can be seen that tower shadow effect leads to roughly a 70% increase in DEL. This result is consistent with the roughly 50% increase of moment range at rated conditions shown in Fig. 6B. The increase in DEL is maintained for a wide range of overhang clearances. Note that this range of OH* is consistent with a rotor tip clearance range of 4.7D to 7.0D from the rear tower surface. As such, the tower shadow effect is not very sensitive to tower clearance for steady wind. The more important operational case of turbulent wind also shows a very weak influence of tower shadow, consistent with the results of Fig. 8B, and this holds over a wide range of clearance with even further reductions for the largest clearance (consistent with Fig. 9A).

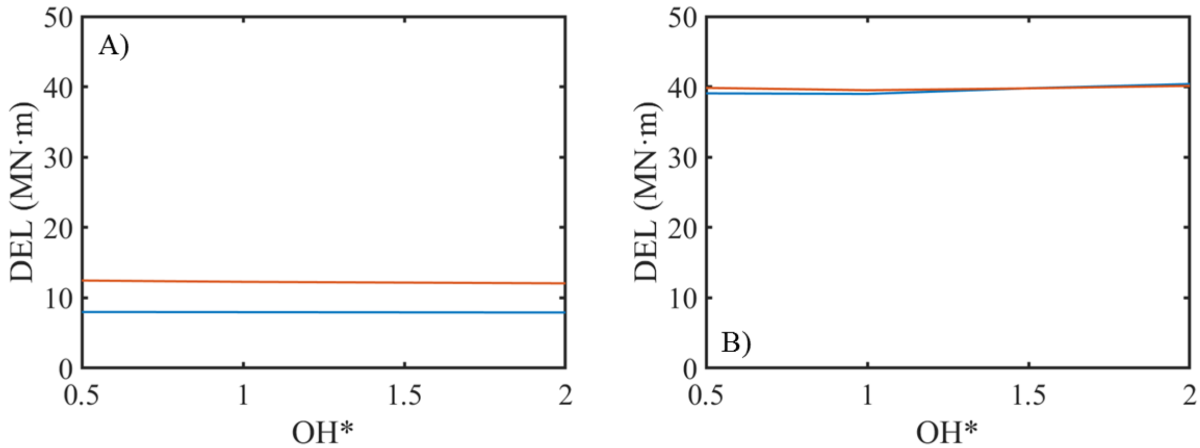

Figure 9. Damage equivalent loads at rated conditions as a function of non-dimensional overhang (nominal OH = 8.16m) under A) steady wind & B) turbulent wind.

3.4 Potential Impact of a Tower Fairing

The above results show that under steady wind conditions, as in a low turbulence wind tunnel, the tower shadow effect yields a pronounced an increase in DEL of about 70% at rated conditions (as seen above). An aerodynamic fairing that shrouds the tower is the most commonly proposed solution to reduce the effect of tower shadow (Koh & Ng, 2016) and a fairing has been shown to reduce blade moment fluctuations experimentally for a research turbine (Noyes *et al. 2018b*; Hand *et al.* 2001). To investigate the effect of a tower fairing for a geometry consistent with a state-of-the-art extreme-scale wind turbine, one must incorporate the effects of drag reduction into the FAST wake model. Herein this is approximated by reducing the drag coefficient of the tower by a constant factor over the range of Reynolds numbers considered. Such an approach is consistent with changes in drag for a 2:1 ellipse as compared to a cylinder of the same width, whereby the elliptical shape reduced the drag by about 75% over a wide range of Reynolds numbers (Blevins, 1984; Noyes *et al.* 2018b). Herein, a drag coefficient reduction of 75% is estimated for fairing effectiveness consistent with maximum performance designs with rounded trailing edges (Noyes & Loth, 2017). More advanced fairings can have higher effectiveness at perfectly aligned conditions, but are more like an ellipse when considering over an average drag reduction range of angles of attack from 0^o to 20^o (Noyes & Loth, 2017).

FAST simulations were run with steady rated wind using reduced tower drag i.e. fairings with different simulated effectiveness, and the impact on DEL are shown in Figure 10. A fairing with 75% effectiveness (75% drag reduction) leads to roughly a 75% reduction in the portion of the DEL that is attributed to tower shadow effects. Note that the green line does not exactly meet the blue dashed line at fairing effectiveness of 100%. This is because the potential flow portion of the FAST tower shadow model is turned on with the fairing, but turned off in the ideal case. Even for a hypothetical fairing of zero drag, the potential flow field has some contribution to the DEL (as would be the case for a cylinder as well). However, this potential flow portion of the model is minimal compared with that due to the drag-based velocity deficit. The results indicate that a tower fairing can significantly reduce the DEL for a downwind turbine blade operating in steady-state conditions, as in a wind tunnel. While an extreme-scale turbine would not be expected to operate in a wind tunnel, one could operate a sub-scale version using gravo-aeroelastic scaling (Kaminski *et al.* 2018) for which the non-dimensional moments and dynamics would be effectively replicated. In this case, the relative % saving in DEL with a tower fairing can be expected to occur by use of a tower fairing.

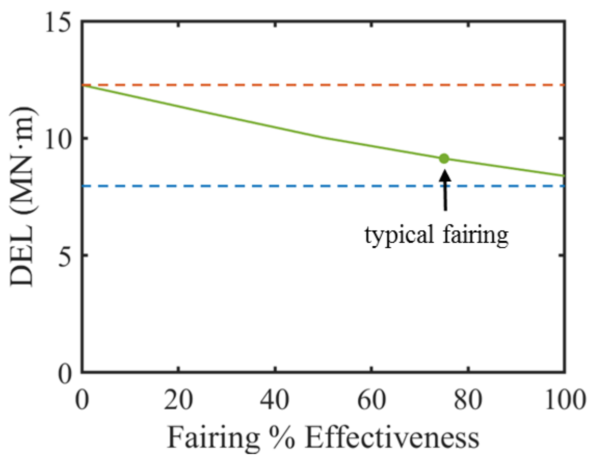

Figure 10. Damage equivalent load varying the tower fairing effectiveness from 0% to 100% drag reduction under steady rated wind.

Under general operating (turbulent) conditions with an extreme-scale turbine, even an ideal tower fairing (that perfectly eliminates tower shadow) would demonstrate little benefit. This is because the atmospheric turbulent fluctuations dominate the fluctuations from tower shadow effects. As a result, the impact of fairing effectiveness was not considered for the turbulent flow case, as such the cost and complexity for including such a fairing would be impractical. In particular, modeling this effect would require considering the angular inertia and self-aligning moment of the fairing to predict the dynamic so misalignment angle. Furthermore, the tower fairing under turbulent conditions would also be less effective than for steady conditions since the wind can change direction rapidly, leading to a period under which the fairing is misaligned with the wind and therefore operating with less than ideal efficiency.

4. Conclusions

FAST simulations of a 13.2 MW downwind two-bladed turbine were conducted with and without using the tower wake model. The difference between the two simulations was due to tower shadow effects. The simulations were run in steady and turbulent wind, with varying tower clearance, and with different simulated tower fairings. All these simulations were conducted to answer two questions: 1) Is tower shadow a significant problem for extreme-scale downwind turbine blade loads in atmospheric turbulence? 2) How much benefits could a tower fairing provide aerodynamically?

For steady conditions, tower shadow was found to create a significant negative impulse in blade angle of attack and force coefficient, though the effect of relative velocity magnitude was negligible. This resulted in a significant decrease in the minimum moment experience by a rotor blade over a range of wind speeds. Under steady wind conditions, the tower shadow effect made up 40% of the total Damage Equivalent Loads. Therefore, a tower fairing could be useful to eliminate these fluctuations for operation in steady conditions, e.g. for a sub-scale model in a wind tunnel. A fairing may reduce the tower shadow effect by roughly 75% when aligned with the flow. This answers the first question above, i.e. a fairing can be helpful for steady-state wind conditions.

For turbulent wind typical of operating conditions, the tower shadow effect on blade DEL was almost negligible (accounting for an increase of only about 3%). This is because the wind velocity fluctuations due to turbulence were much more impactful than those due to tower shadow. The trend did not seem to be highly sensitive to tower clearance. Therefore, based on these results a tower fairing would be largely wasted as a load-reducing approach in a downwind extreme-scale turbine since the tower shadow effect is generally negligible, which answers the second question above.

Although a tower fairing is not needed to reduce blade load fluctuations from tower shadow in turbulent field conditions, it could still be useful in reducing aeroacoustic noise from shadow effects. This could be especially important for onshore siting, whereby acoustic concerns are more important. In contrast, turbines in locations which are far from the coast, e.g. 25-50 miles from shore, would yield much less concern with respect to acoustic emission. As such, off-shore extreme-scale downwind turbines are not expected to be have a significant negative impacted due to tower shadow. This helps clear the path for consideration and design of such downwind system for offshore deployment.

Acknowledgments

The authors would like to thank ARPA-e for funding and guiding the research reported herein. The authors would like to thank the following: Gavin Ananda from the University of Illinois Urbana-Champaign for conducting the aerodynamic design of the rotor and Dr. Todd Griffith from the University of Texas Dallas for conducting the structural design of the rotor.

Funding

Advanced Research Projects Agency – Energy: DE-AR0000667

References

Ananda, G. K., Bansal, S., & Selig, M. S. (2018). Aerodynamic Design of the 13.2 MW SUMR-13i Wind Turbine Rotor. In *2018 Wind Energy Symposium* (p. 0994).

Blaabjerg, F., & Ma, K. (2013). Future on power electronics for wind turbine systems. *IEEE Journal of Emerging and Selected Topics in Power Electronics*, *1*(3), 139-152.

Blevins, R. D. (1984). Applied fluid dynamics handbook. *New York, Van Nostrand Reinhold Co., 1984, 568 p.*

Butterfield, C. P., Musial, W., & Jonkman, J. (2007). *Overview of offshore wind technology: preprint* (No. NREL/CP-500-42252). National Renewable Energy Lab.(NREL), Golden, CO (United States).

Crawford, C., & Platts, J. (2008). Updating and optimization of a coning rotor concept. *Journal of Solar Energy Engineering*, *130*(3), 031002.

De Vries, E. (2016). Offshore Turbine Yearbook: A quarter-century of offshore turbine technology development. *RENews and Natural Power.* Retrieved June 20, 2018, from http://renews.biz/PDFs/reNEWS_OTY 2016.pdf

Eggers, A., Chaney, K., & Digurmarthi, R. (2005, January). An exploratory study of motion and loads on large flap-hinged rotor blades. In *43rd AIAA Aerospace Sciences Meeting and Exhibit* (p. 1184).

Hand, B., & Cashman, A. (2018). Aerodynamic modeling methods for a large-scale vertical axis wind turbine: A comparative study. *Renewable Energy*, *129*, 12-31.

Hand, M. M., Simms, D. A., Fingersh, L. J., Jager, D. W., Cotrell, J. R., Schreck, S., & Larwood, S. M. (2001). *Unsteady aerodynamics experiment phase VI: wind tunnel test configurations and available data campaigns* (No. NREL/TP-500-29955). National Renewable Energy Lab., Golden, CO.(US).

Hayman, G. J., & Buhl Jr, M. (2012). Mlife users guide for version 1.00. *National Renewable Energy Laboratory, Golden, CO*.

International Electrotechnical Commission. (2005). Wind Turbine—Part 1: Design Requirements, IEC 61400-1. *International Electrotechnical Commission, Geneva, Switzerland*.

Jonkman, B. J. (2009). *TurbSim user's guide: Version 1.50*(No. NREL/TP-500-46198). National Renewable Energy Lab.(NREL), Golden, CO (United States).

Jonkman, B., & Jonkman, J. (2016). FAST v8. 15.00 a-bjj. *National Renewable Energy Laboratory*.

Jonkman, J. M. (2003). *Modeling of the UAE wind turbine for refinement of FAST {_} AD* (No. NREL/TP-500-34755). National Renewable Energy Lab., Golden, CO (US).

Kaminski, M., Loth, E., Qin, C., & Griffith, D. T. (2018). Gravo-Aeroelastic Scaling a 13.2 MW Wind Turbine Blade to a 1-meter Model. In *2018 Wind Energy Symposium* (p. 1731).

Koh, J. H., & Ng, E. Y. K. (2016). Downwind offshore wind turbines: Opportunities, trends and technical challenges. *Renewable and Sustainable Energy Reviews*, *54*, 797-808.

Krogstad, P. Å., & Eriksen, P. E. (2013). "Blind test" calculations of the performance and wake development for a model wind turbine. *Renewable energy*, *50*, 325-333.

Leishman, J. G. (2002). Challenges in modelling the unsteady aerodynamics of wind turbines. *Wind energy*, *5*(2-3), 85-132.

Loth, E., Steele, A., Qin, C., Ichter, B., Selig, M. S., & Moriarty, P. (2017). Downwind pre-aligned rotors for extreme-scale wind turbines. *Wind Energy*, *20*(7), 1241-1259.

Moriarty, P. J., & Hansen, A. C. (2005). *AeroDyn theory manual* (No. NREL/TP-500-36881). National Renewable Energy Lab., Golden, CO (US).

Munduate, X., Coton, F. N., & Galbraith, R. A. M. (2004). An investigation of the aerodynamic response of a wind turbine blade to tower shadow. *Journal of solar energy engineering*, *126*(4), 1034-1040.

Noyes, C., & Loth, E. (2017). Tower Fairing Concept for Downwind Turbines. In *35th AIAA Applied Aerodynamics Conference* (p. 4070).

Noyes, C., Qin, C., & Loth, E. (2018a). Pre-aligned downwind rotor for a 13.2 MW wind turbine. *Renewable Energy*, *116*, 749-754.

Noyes, C., Qin, C., Loth, E., & Schreck, S. (2018b). Measurements and predictions of wind turbine tower shadow and fairing effects. *Journal of Wind Engineering and Industrial Aerodynamics*, *179*, 297-307.

O'Connor, K., Loth, E., & Selig, M. S. (2015). Experiments on Fairing Design for a Wind Turbine Tower. In *33rd Wind Energy Symposium* (p. 1664).

Pavese, C., Kim, T., & Murcia, J. P. (2017). Design of a wind turbine swept blade through extensive load analysis. *Renewable Energy*, *102*, 21-34.

Polinder, H., Ferreira, J. A., Jensen, B. B., Abrahamsen, A. B., Atallah, K., & McMahon, R. A. (2013). Trends in wind turbine generator systems. *IEEE Journal of emerging and selected topics in power electronics*, *1*(3), 174-185.

Powles, S. R. J. (1983). The effects of tower shadow on the dynamics of a horizontal-axis wind turbine. *Wind Engineering*, 26-42.

Reiso, M., Hagen, T. R., & Muskulus, M. (2013). A calibration method for downwind wake models accounting for the unsteady behaviour of the wind turbine tower shadow behind monopile and truss towers. *Journal of Wind Engineering and Industrial Aerodynamics*, *121*, 29-38.

Snyder, M. H., & Wentz Jr, W. H. (1981). Dynamics of wakes downstream of wind turbine towers.

Vargo, D. J. (1974). Wind energy developments in the 20th century.

Veers, P. S., Ashwill, T. D., Sutherland, H. J., Laird, D. L., Lobitz, D. W., Griffin, D. A., ... & Miravete, A. (2003). Trends in the design, manufacture and evaluation of wind turbine blades. *Wind Energy*, *6*(3), 245-259.

Wang, T., & Coton, F. N. (2001). A high resolution tower shadow model for downwind wind turbines. *Journal of Wind Engineering and Industrial Aerodynamics*, *89*(10), 873-892.

Yoshida, S., & Kiyoki, S. (2007). Load equivalent tower shadow modeling for downwind turbines. *Nihon Kikai Gakkai Ronbunshu, B Hen/Transactions of the Japan Society of Mechanical Engineers, Part B*, *73*(6), 1273-1279.

Zahle, F., Sørensen, N. N., & Johansen, J. (2009). Wind turbine rotor-tower interaction using an incompressible overset grid method. *Wind Energy*, *12*(6), 594-619.

Chapter 5

Extreme-Scale, Load-aligning Rotor: to Hinge or Not to Hinge?

Abstract

Load alignment, balancing the thrust moment with the centrifugal moment, is a promising innovation for extreme-scale wind turbines. Load alignment can allow for longer blades, facilitating an increase in power capture, while maintaining similar blade moments. As blades lengthen, larger coning angles are required to balance increasing thrust moments with centrifugal moments. This yields a key question for such extreme-scale load-aligned rotors: should the blades be hinged to actively vary coning or simply be pre-aligned at a fixed coning angle? To answer this, steady and turbulent FAST simulations were conducted on a variety of downwind rotors with different blade lengths and coning angles operating with a standard controller. The longest rotor without a hinge was shown to increase the energy production by 13.4% without an increase in peak blade moments. However, in turbulent wind there was an approximately 100% increase in fatigue loads as characterized by the associated damage equivalent load. When the coning angle was allowed to change slowly as a function of wind speed (by means of a morphing hinge), the power increased by 19% and the peak moments increased under turbulent wind conditions, but only by 40%. Inclusion of teeter with the hinge decreased both the peak flapwise moments and the fatigue damage equivalent loads back to near baseline values while maintaining 12% power production increase, as compared with the baseline rotor. The results show that load alignment can be achieved with a fixed coning angle (pre-alignment) or by a morphing hinge. A morphing hinge allows for up to a 4.6% power increase compared with a fixed coning angle.

Nomenclature

C_P	Power coefficient
k	Torque control constant
m	Blade mass
M	Root flapwise bending moment
M_{max}	Maximum allowed root flapwise bending moment
M_{peak}	Peak root flapwise bending moment from a single simulation
P	Generator power
R	Projected rotor radius
R_h	Hub radius
S	Blade length
U_∞	Free stream wind velocity
β	Coning angle
β_{ID}	Initial design coning angle to reach power constraint
β_{LA}	Coning angle that results in zero average root flapwise bending moment

β_{PA} Fixed rotor coning angle set by maximum flapwise moment at rated conditions
λ Tips speed ratio
ρ Air density
τ Torque
ϕ Blade pitch
ψ Azimuth angle, $\psi = 0°$ when the blade points up
ω Rotational rate of the rotor
$[\ ]_{rated}$ At rated power

1. Introduction

Wind energy plays a vital role in the world's energy sustainability and environmental stewardship. However, wind energy systems, like all renewable systems, face steep economic challenges compared with other carbon-based energy sources, e.g. natural gas (Esteban & Leary, 2012). Many wind turbine designers attempt to lower the cost per kilowatt-hour for wind energy by increasing the size of wind turbines. More power can be generated with larger turbines, and, to a point, this size increase outweighs the increased cost of the larger turbine (Arias-Rosales & Osorio-Gómez, 2018; Barlas & van Kuik, 2010; Sieros *et al.* 2012). One primary challenge limiting the size of wind turbines is the blade moments that must be structurally supported (Zhang *et al.* 2016; Fingersh *et al.* 2006). Many innovations for wind turbines focus on ways to support these extreme-moments e.g. advances in materials science or control schemes (Civelek *et al.* 2017; Murdani *et al.* 2017).

The load alignment concept is one very promising innovation that could reduce flapwise moments allowing for larger wind turbines (Noyes *et al.* 2018; Eggers *et al.* 2005; Crawford & Platts, 2008). By countering the thrust moment with a centrifugal moment, downwind coned rotors can have significantly lower average flapwise bending moments than similarly sized, upwind, low-coned rotors (Loth *et al.* 2017). Load alignment could allow for rotor sizes (>13MW) that would otherwise have impractically large bending moments with a conventional design. The ultimate flapwise bending moment is a common design driver (Ronold & Larsen, 2000; Griffith & Richards, 2014).

The advantages of load alignment as a mechanism for blade-moment reduction have been well documented (Noyes *et al.* 2018). However, load alignment may also be used to increase power capture without increasing the blade-bending moments. One way power can be increased is by designing a downwind rotor with a longer blade length, which is associated with a larger downwind thrust moment, but countering the thrust with a larger downwind coning angle to increase the upwind centrifugal moment. The coning angle can be selected to provide a good balance between power capture and load alignment as shown in Fig. 1a. If the resulting moment is unchanged but the effective radius increases, then the new rotor has greater power production with equivalent flapwise moments.

A second way to apply load alignment to increase energy production without increasing flapwise bending moments is with a morphing hinge (Ichter *et al.* 2016), shown in Fig. 1b. The hub with a morphing hinge allows the coning angle to adjust for different winds speeds. A morphing hinge would allow for relatively high coning angles near rated power (when moments are high) and lower coning angles at lower wind speeds (where moments are low) to maximize the power capture while ensuring the peak moments never exceed a prescribed design flapwise bending moments.

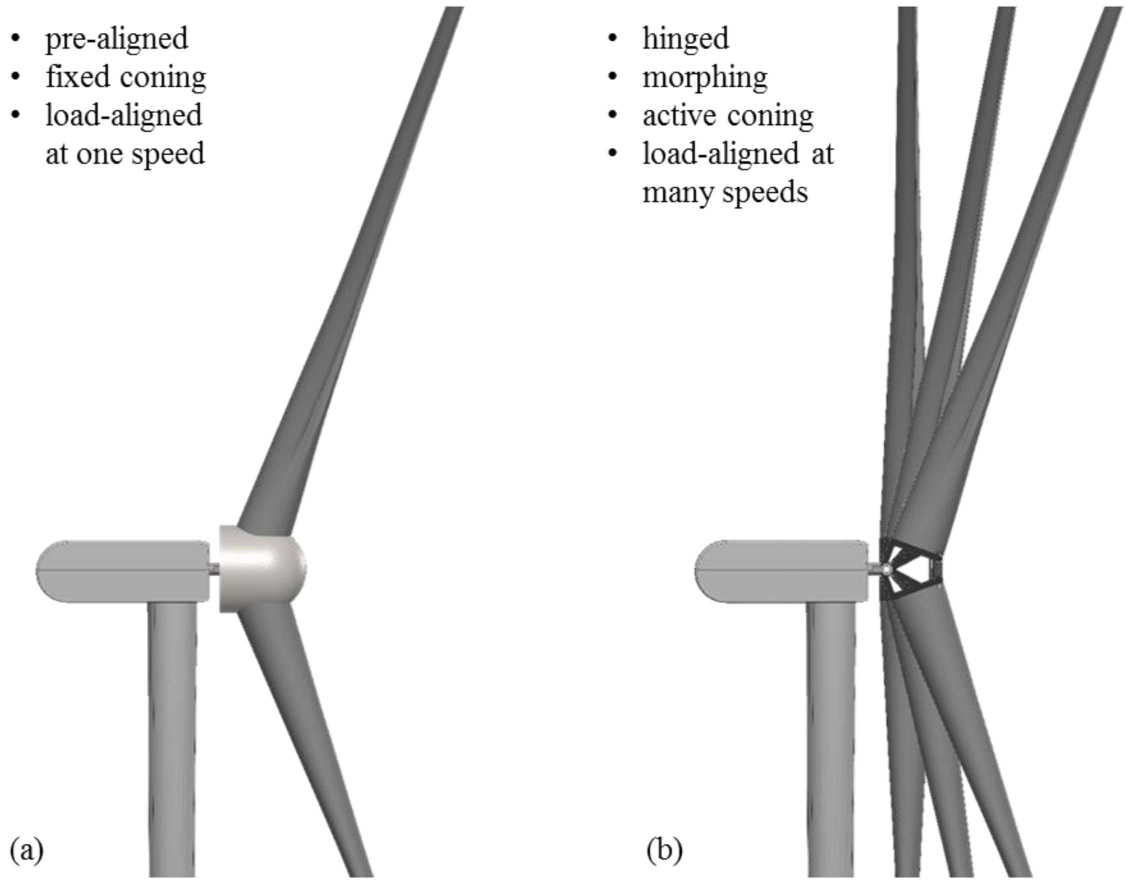

Fig. 1 Load-aligned wind turbine for (a) pre-aligned operation and (b) hinged operation

The use of longer blades or a morphing hinge is accompanied by an increase in turbine Capital Expense and Operational Expense (CapEx & OpEx). However, should the increase in Annual Energy Production (AEP) is sufficiently large, it would offset the increased cost and the Levelized Cost of Energy (LCOE) would decrease (Chen *et al.* 2018; Chehouri *et al.* 2015). Levelized cost of energy is calculated with a Fixed Charge Rate as

$$LCOE = \frac{(CapEx\ x\ FCR) + OpEx}{AEP} \tag{1}$$

The objective of this research, which to the authors' knowledge has never been investigated, is to quantify the increase in power capture by use of load alignment while avoiding, or at least minimizing, increases in peak flapwise blade moments. Rotors of various length and coning angles will be simulated. Energy production and blade moments will be compared for the different rotors with and without a morphing hinge. This investigation is the first that compares pre-aligned rotors (without a hinge) with morphing rotors (with a hinge) and quantifies the relative increase in power from the inclusion of a hinge. It is also the first study to investigate the sensitivity of blade length and/or blade teeter in the context of load alignment.

2. Methods for Aerodynamic Design, Load Prediction, and Control

To allow for equivalent (or greater) power capture with larger amounts of load alignment, longer blades at higher coning angles are required. The longer blades allow for the greater power capture, while the higher coning angle allows for better opportunities for load alignment. Load alignment occurs when the coning angle of the blades is such that the average upwind flapwise moment on the blades due to centrifugal forces is exactly equal to the average downwind flapwise moment on the blades due to thrust forces. Note that gravity forces (which vary with azimuthal location) and turbulence (which vary with time) will cause deviations such that a rotor can only be load-aligned in a mean sense. The coning angle where the blades are load-aligned at a specific wind speed is defined as β_{LA}. The following describes: a) the aerodynamic methods used to develop of a family of rotors of differing lengths and specifications in terms of length, geometry and mass and b) the methods to analyze the blade moments and the rotor control design process.

2.1 Aerodynamic Design and Family of Rotors

Two aerodynamic design tools developed at the University of Illinois at Urbana-Champaign were used in the design of the rotor family: PROFOIL (Selig 1998) and PROPID (Selig, 2012). PROFOIL, is a multipoint inverse airfoil design tool that allows users to prescribe the desired velocity distributions over different sections of the airfoil and set additional constraints such as thickness, camber, and pitching moment. The specifications and constraints are then solved in a system of nonlinear equations using a multidimensional Newton iteration scheme. PROFOIL was used to generate the F1-family of flatback airfoils based on a historical thickness distribution for typical wind turbines (Ananda *et al.* 2018). XFOIL (Drela & Youngren, 2001), an airfoil analyses tool, was used in concert with PROFOIL during the airfoil design process of the F1-family of airfoils.

PROPID is an inverse propeller and rotor design tool used to design the geometry of the rotor. The blade length, chord, and twist distribution, and pitch are output based on a set of performance and design constraints such as: tip-speed ratio (λ), axial induction factor, rated power and wind speed, lift coefficient distribution, and coning angle. Four rotors were designed using PROPID with the F1 airfoil family. The rotor family was named SUMR (Segmented Ultralight Morphing Rotor) and is part of a broader family of rotors previously investigated (Martin *et al.* 2017; Noyes *et al.* 2017; Ananda *et al.* 2018). All four SUMR rotors were designed for the same rated power ($P_{rated} = 13.2MW$), rated wind speed ($U_{rated} = 11.3m/s$), and average wind speed ($U_{avg} = 8.5m/s$). These values correspond with a concept rotor developed by Sandia National Lab (Griffith, 2011). Table 1 shows additional parameters that all four rotors hold in common. The design cone angle, β_{ID}, was varied resulting in various output blade lengths to achieve the rated power and speed constraints set.

Table 1. General SUMR rotor design parameters

Blade Number	2
Rated Generator Power (P_{rated})	13.2 MW
Nominal Rated Wind Speed (U_{rated})	11.3 m/s
Induction Factor	0.33
Tip Speed Ratio (λ)	9.25
Hub Radius (R_h)	2.5 m

The initial design coning angles ranged from $\beta_{ID} = 12.5°$ to 42.5° in 10° increments, and the resultant blade lengths ranged from $S = 104.2m$ to $S = 139.3m$ (Fig. 2). The five flatback airfoil geometries that constitute the F1 airfoil family are shown at roughly equally distributed spanwise stations. The different rotor blades are identified as SUMR-xxx, where the xxx is the nominal length of the blade in meters (105, 110, 120 and 140m) and the exact lengths are given in Table 2. All rotors by design have similar power curves when operating at the initial design coning angle.

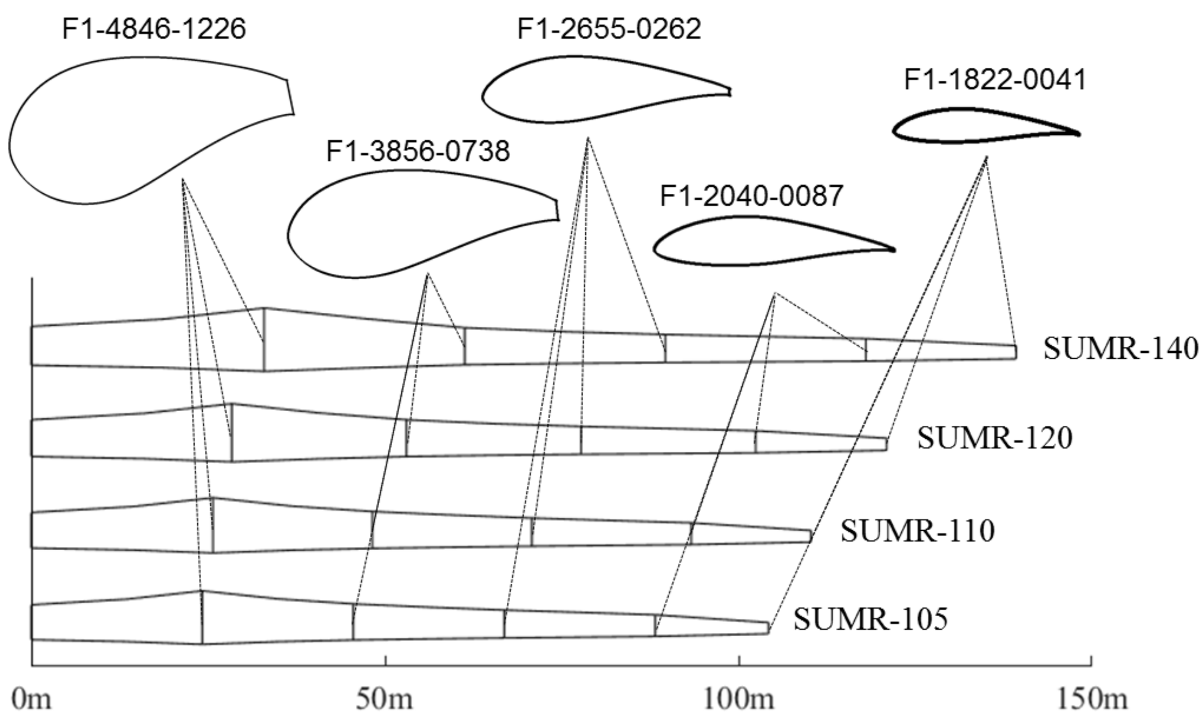

Fig. 2 Schematic of the four rotor blades, showing the blade planforms and flatback airfoils at five stations along the blades

A complete structural design of the SUMR-105 blades was conducted. The entire design process of SUMR-105 has been documented (Griffith, 2019), whereby SUMR13i-v6_S4 in the report is identical to SUMR-105 used herein. The structural properties of the other three rotors (SUMR-110, 120 and 140) were calculated using scaling laws. The scaling parameter (η) is defined as the new blade length normalized by the baseline blade length ($\eta \equiv \frac{S}{S_0}$). The linear mass density (m') was scaled by $\eta^{1.1}$, and the linear stiffness distribution (k') was scaled by $\eta^{3.5}$. These scaling factors have been shown to be reasonable approximations for structural properties in lieu of a complete structural design for each rotor (Griffith & Ashwill, 2011). The resulting blade masses based on scaling are also shown in Table 2 in terms of mega-grams (Mg = 10^3 kg = 10^6 g), which are also equivalent to metric tons.

Table 2. Specific definitions of the four rotor blades

	Blade Length (S)	**Initial Design Coning Angle (β_{ID})**	**Blade Mass (m)**
SUMR-105	104.2 m	12.5°	54.8 Mg
SUMR-110	110.2 m	22.5°	61.5 Mg
SUMR-120	121.0 m	32.5°	74.6 Mg
SUMR-140	139.3 m	42.5°	100.1 Mg

2.2 Load Prediction and Control

At the initial design coning angles ($\beta = \beta_{ID}$), all four rotors are designed to capture the same amount of power at any steady wind speed. For below rated speeds, all four rotors can generate more than this baseline power by operating at $\beta < \beta_{ID}$ (lowering the coning angle results in an increase in projected area). However, as the coning angle decreases, the average bending moments increase.

The following section will investigate how much power can be generated with the different rotors with a hinge (morphing conditions where β varies with wind speed) and without a hinge (pre-aligned conditions where β does not vary with wind speed). These two system cases will be considered with an imposed constraint of limiting the peak flapwise bending moment.

To predict blade moments, the rotors were simulated using FASTv8 (Jonkman & Buhl 2005). The tower degrees of freedom were turned off for all the simulations. The different rotor masses, and rotational rates result in different system resonance frequencies. To isolate the differences between the rotors without having redesign the tower for each rotor, an assumption is made that the tower design would be sufficiently stiff to avoid resonance inside the operating regime.

Two wind conditions were considered for each rotor: steady and normal turbulence. For steady wind operation, a constant wind input with no shear nor yaw was employed. Simulations were run with wind speeds ranging from cut-in (4 m/s) to rated power (nominally at 11.3 m/s) at 0.1 m/s increments. The simulations were run in an open loop configuration, by defining the blade pitch and rotational rate (ω) for each simulation. The rotational rate was calculated by fixing the tip speed ratio (λ) and calculating

$$\omega = \frac{\lambda\, U_\infty}{R_h + S\cos(\beta)}\left(9.549\,\frac{rpm}{rad/s}\right) \tag{2}$$

In Eq. 2, S is blade length and R_h is hub radius. While the C_P is a weak function of β assuming constant λ, the optimal C_P occurs at the same λ regardless of β.

For turbulent wind operation, simulations were run with numerically-generated turbulent wind fields. Each simulation ran for 11 min but the first minute was discarded. It was assumed that hinging at extreme scales would be slow and therefore having a constant value for a 10-min simulation is a reasonable simplification. The turbulent wind fields were generated using TurbSim (Jonkman & Buhl 2009). Kaimal turbulence model was used with medium turbulence intensity. The grid resolution was 14x14 with total size 350m x 350m. The reference height was set to the hub height, which was 180m for all rotors in accordance with IEC Class IIb wind. At a given nominal wind speed (roughly the average wind speed at the reference height) six simulations were run with different numerically generated wind fields.

Damage Equivalent Loads (DELs) for root flapwise bending moment were calculated using MLife (Hayman & Buhl 2012). The DEL is the amplitude of a zero mean, 1 Hz sinusoidal signal that results in the same fatigue damage as the original signal. MLife uses a rain flow counting algorithm to compute DEL. Short-term DEL was calculated from each 10-min simulation and the data from all the simulations was used to calculate Lifetime DEL. Lifetime DEL requires an assumed lifetime of 20 yr, and wind speed defined by a Weibull distribution with shape factor of 2 and scaling factor of 9.59 m/s. The same distribution is used to calculate Annual Energy Production (AEP).

From a controls perspective, a rotor with a variable coning angle poses interesting challenges, requiring control laws to be updated in order to account for the varying dynamics induced by the additional degree of freedom. Region II controllers typically vary the applied generator torque to control rotor speed to achieve maximum aerodynamic efficiency as the wind speed changes. The governing equation defining the system is given as

$$J_{rotor}\dot{\psi} = \tau_{aerodynamic} - \tau_{generator} \tag{3a}$$

$$\tau_{aerodynamic} = k\omega^2 \tag{3b}$$

where J is the polar moment of inertia, ω is the angular velocity, and τ is a torque. If the coning angle is invariant, the aerodynamic torque is defined as

$$k = \frac{1}{2}\rho\pi R^5 \frac{C_p}{\lambda^3} \tag{3c}$$

where ρ is the density of air, R is the projected rotor radius. A conventional control scheme (Manwell *et al.* 2010) is to set the generator torque equal to the torque constant (k) multiplied by the rotational rate squared, which can be shown to achieve maximum efficiency when the rotor characteristics are well known and in steady-state (Pao and Johnson 2011). Since a hinged rotor has an additional degree of freedom that influences J_{rotor} and therefore the behavior of the conventional control law (3b), the optimal k value is a function of coning angle (Zalkind *et al.*

2017), specifically k decreases with $\cos^2(\beta)$. For each rotor, k was determined at $\beta = 2.5°$ and scaled when the rotor is operating with a different coning angle.

Gain scheduled PI pitch control inspired by (Jonkman et al. 2009) and updated for the SUMR project is used for above-rated rotor speed control. The natural frequency (ω_n) and damping ratio (ζ) within the second approximating second order transfer function are tuned to achieve proportional (k_p) and integral (k_i) gains resulting in less than 10% rotor speed overshoot for a stepped inflow from 10 m/s to 12 m/s. Gain scheduling functions are determined by computing the sensitivity power with respect to pitch angle for wind velocities ranging from rated to cut-out (Jonkman et al. 2009).

Table 3. Control parameters

	Blade Length (S)	**Sensitivity (W/rad)**	**J (kg-m^2)**
SUMR-105	104.2 m	-3.5583e+07	217828768
SUMR-110	110.2 m	-1.1324e+08	262778944
SUMR-120	121.0 m	-1.3193e+08	355893696
SUMR-140	139.3 m	-8.848e+07	550432000

3. Results

3.1 Steady Wind

Throughout this investigation, three strategies were used to determine the coning angle schedule as a function of wind speed: low-cone, pre-aligned & hinged, outlined in Table 4. The low-cone strategy is used solely as a reference as it violates the design constraint. Neither the pre-aligned nor the hinged strategy violate the steady design constraint. The hinged strategy is expected to produce more power because it has lower coning at low speeds, but has the additional complexity of a morphing hinge.

Table 4. Three coning strategies

Low-Cone	Pre-Aligned	Hinged
$\beta = 2.5°$	$\beta = \beta_{PA}$	$\beta = f(U_\infty)$
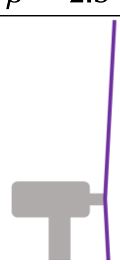	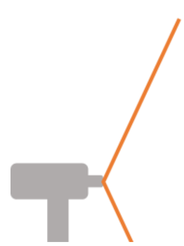	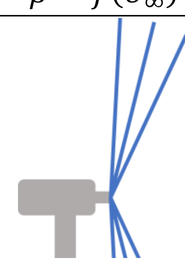
violates moment-constraint before rated power	reaches moment-constraint at rated power	reaches moment-constraint before rated power, then cones to maintain constraint

The design constraint used to develop β_{PA} for the pre-aligned strategy and $f(U_\infty)$ for the hinged strategy was a constraint on the peak root flapwise bending moment the rotor experiences during a simulation with steady wind. The moment-constraint ($M_{max} = 50$ MN · m) was selected as the maximum moment for the SUMR-105 rotor at its initial design coning angle ($\beta = 12.5°$).

This moment-limiting constraint was used to conduct a preliminary parametric study to quantify the tradeoffs between blade length and power with and without a morphing hinge. The constrained coning angle limits the increase in root flapwise bending moment that is associated with increased blade length. Constraining the steady state peak moments via coning angle yields a reasonable starting point for a design. The rotor performance in more realistic turbulent conditions will be analyzed in the following section. It is assumed that two different rotors that experience the same peak bending moment (M_{peak}) under steady wind conditions would experience similar ultimate moments under unsteady turbulent wind conditions. The validity of this assumption will be tested in the next section.

The three rotor coning angle strategies (low-cone, pre-aligned & hinged) and the associated peak root flapwise bending moment (M_{peak}) for each rotor are shown in Figs. 3 and 4 for all wind speeds in Region II. Although no simulations were conducted above rated power (Region III), it is known that the mean flapwise bending moments decrease for these higher wind speeds because the blades begin to pitch toward feather to regulate rotor speed and power. Therefore, the required coning to meet the moment constraint would also begin to decrease, as indicated by the dotted arrow.

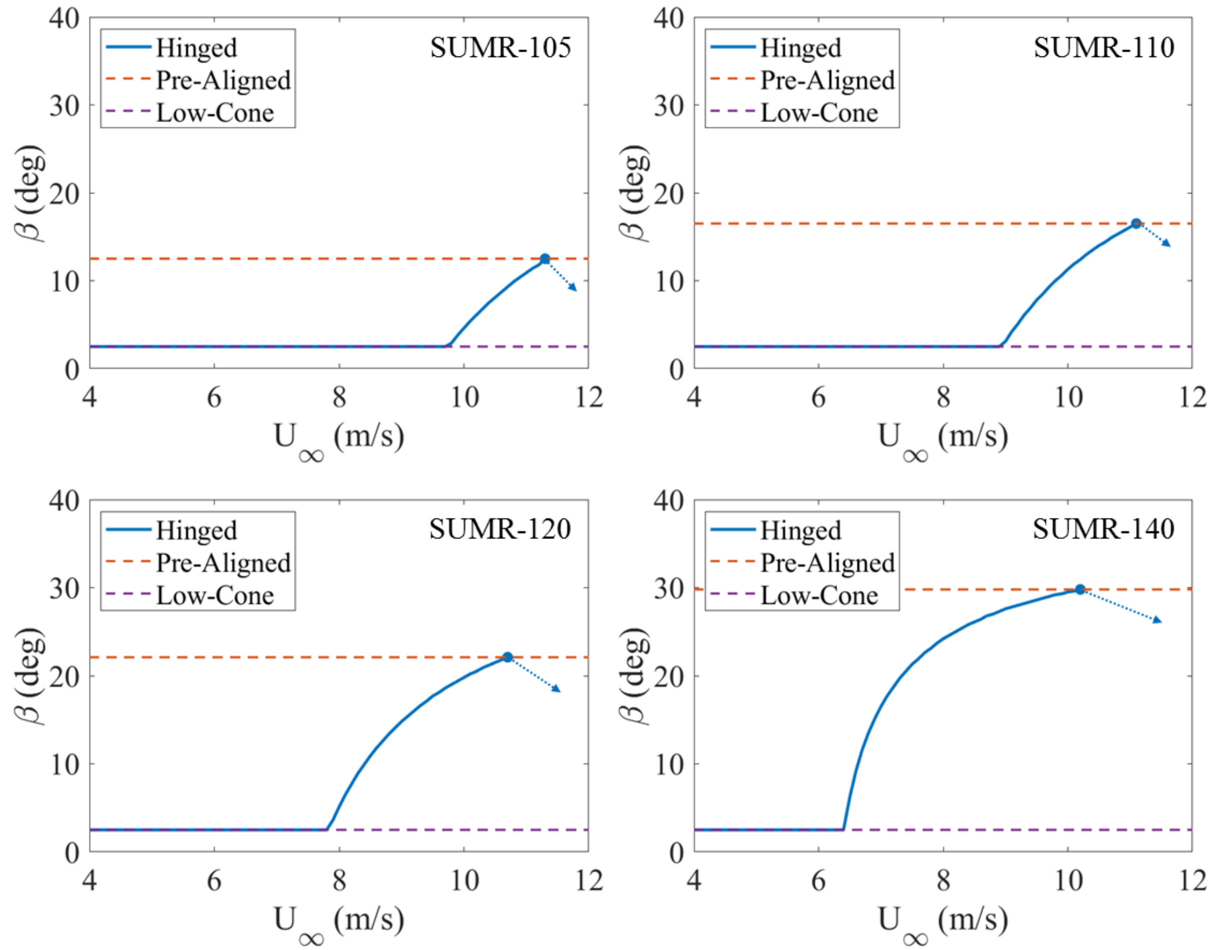

Fig. 3 Coning angle schedules as a function of wind speed in Region II for four rotor designs

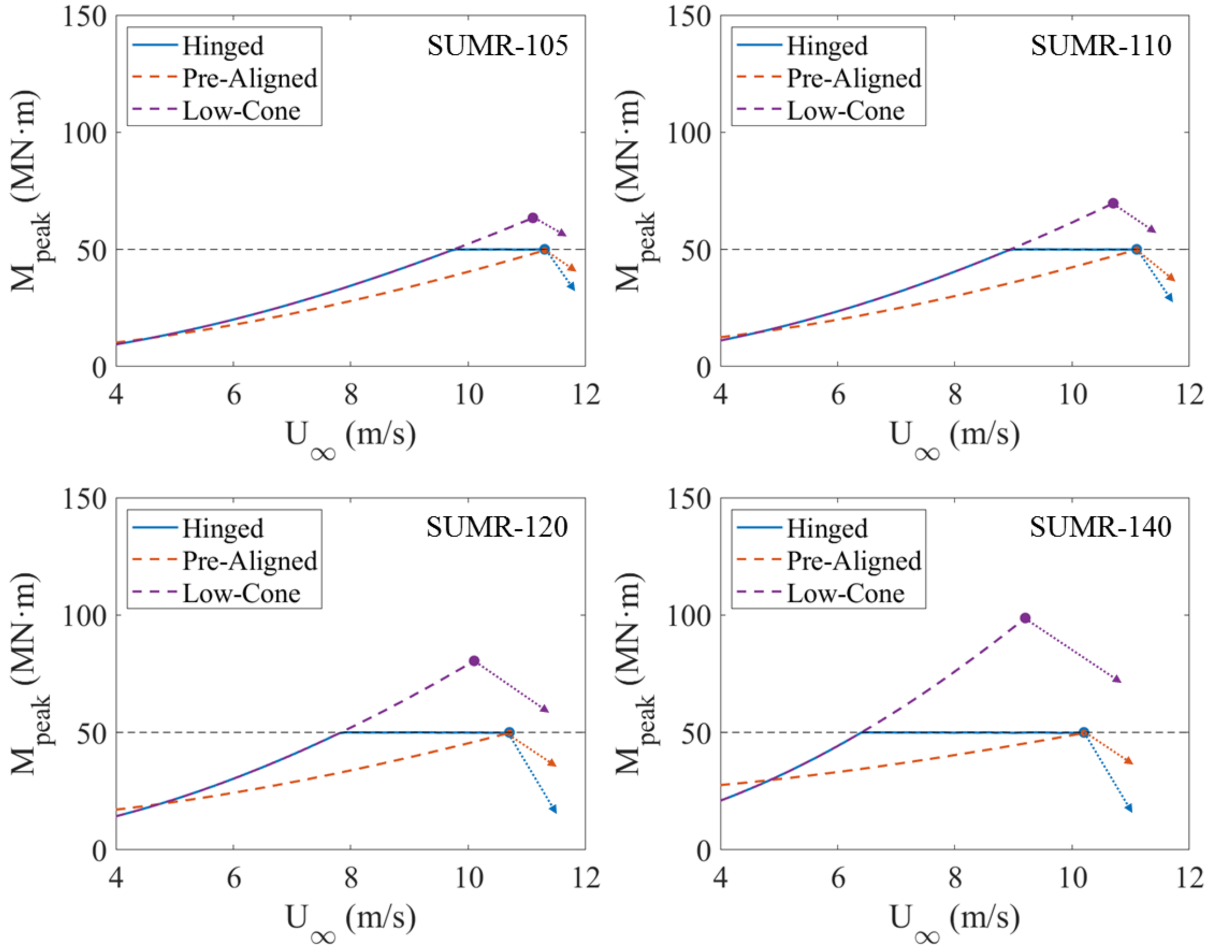

Fig. 4 Simulation-maximum root flapwise bending moment for the four rotors in Region II, under three coning angle schedules (defined in Fig. 3), the moment-constraint shown in black

For the rotors at the low-cone angle, each of the four rotors has the same coning angle of 2.5° as shown in in Fig. 3 and Table 4. As shown in Fig. 4, the associated peak rated moments (M_{peak}) for these low-cone rotors exceed the maximum allowable value before the wind speed reaches the rated condition. The point at which the rotor exceeds the maximum allowable value occurs at lower wind speeds as the blade gets longer.

For the pre-aligned rotors the coning angle (β_{PA}) is constant over wind speed for a given rotor, and for different rotors it increases from $\beta_{PA} = 12.5°$ to $\beta_{PA} = 29.8°$ as blade length increases from $S = 104m$ to $S = 139m$, respectively. As the wind speed increases M_{peak} increases, until it reaches rated power (indicated by the dot). The pre-aligned rotor reaches M_{max} at rated power for all rotors, thus satisfying the maximum moment constraint.

For the rotors at the variable morphing angle, the hinged schedule for coning angle is shown in Fig. 3 as a function of mean wind speed. The angle schedule was set to be the same as the low-cone schedule at low winds speeds, in order to maximize power for conditions where the blade moments are low. However, as the wind speed and the moments increase, the peak bending moment will eventually reach the maximum allowable condition. After this point, the hinged rotor increases its coning angle such that the peak moment plateaus at the maximum allowable value ($M_{peak} = M_{max}$), as shown in Fig. 4. The schedule ensures maximum power within the moment constraint. As the rotor length increases, the morphing schedules predictably need to start an increase in coning angle at a lower wind speed and need to cone to a greater magnitude to stay within the maximum moment. Note that the hinged schedule angle equals the pre-aligned angle at rated power for each rotor. Above rated power (Region III), the moments will decrease as indicated by the dotted arrow. Because the hinge allows for adjustment of the coning angle, the moments in Region III can be reduced to be even less than that for the pre-aligned rotor.

Figure 5 shows the power generated for each rotor in Region II. As expected the low-cone rotor generates the most power, and the pre-aligned rotor generates the least power. The hinged rotor generates power constrained between these two extremes. At low speeds, the hinged rotor follows the low-cone rotor then converges on the pre-aligned rotor at rated power. As the blade length increases so does the difference in area under the curve between the low-cone and the pre-aligned rotors, increasing the potential benefit of the hinge. However, there is a point of diminishing returns because as the blade length increases, the flow speeds over which the hinged rotor can mimic the low-cone rotor decreases. Therefore, the difference in the area under the hinged curve and the pre-aligned curve is a complex function of blade length. Note that low-cone, pre-aligned and morphing all produce the same rated power for all rotors between rated and cut-out conditions, indicated by the dotted arrows.

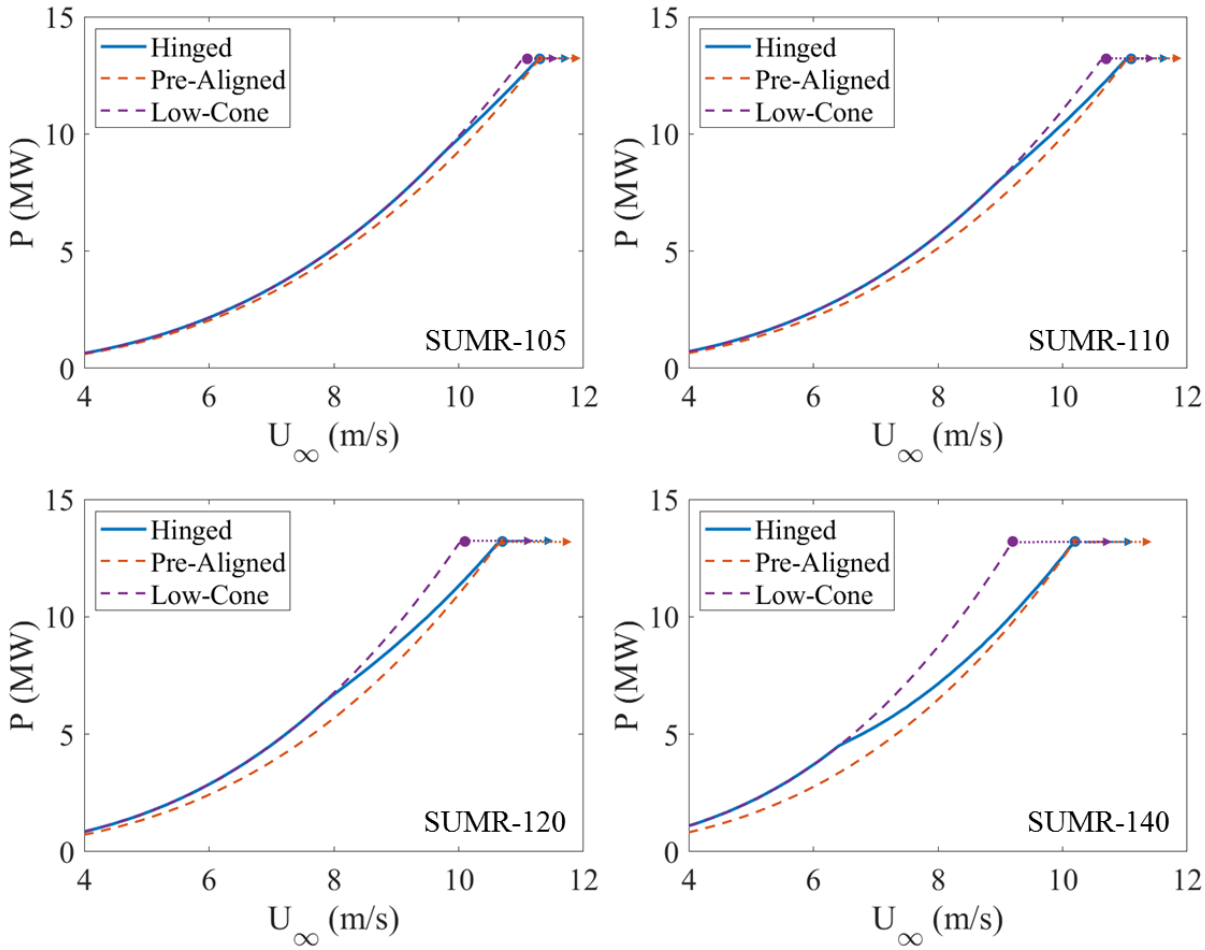

Fig. 5 Simulation-average generator power for the four rotors in Region II, under three coning angle schedules (defined in Fig. 3)

Comparing power production between rotors is most generally assessed with Annual Energy Production (AEP). Many of the key rotor metrics are displayed in Table 5. As blade length increases, so does AEP (for a fixed peak root flapwise bending moment). Increasing the blade length by 33.7% (SUMR-105 to SUMR-140) yields an AEP increase of 13.6% for a pre-aligned rotor, and 19.0% for a hinged rotor. The net AEP advantage of using a hinge over a constant pre-aligned coning angle for a given blade length occurs since one can achieve larger effective diameters below rated conditions with morphing. As such, there are tradeoffs between the increase in AEP and the increase in cost/complexity from a hinge or the increase in material/manufacturing cost of a longer blade. In addition, turbulence can have a significant effect on the peak moments and the power produced, and thus should be considered as part of any tradeoff study.

Table 5. Summary for the four rotors under steady wind conditions, percent difference is compared with SUMR-105 with the pre-aligned schedule

	SUMR-105	SUMR-110	SUMR-120	SUMR-140
Blade Length (S)	104.2 m	110.2 m	121.0 m	139.3 m
Blade Mass (m)	54.8 Mg	61.5 Mg	74.6 Mg	100.1 Mg
Pre-Aligned Angle (β_{PA})	12.5°	16.5°	22.1°	29.8°
Projected Rotor Radius (R)	104.2	108.2	114.6	123.4
Rated Wind Speed (U_{rated})	11.3 m/s	11.1 m/s	10.7 m/s	10.2 m/s
AEP Pre-Aligned - MW·hr/yr	538000	554000	580000	611000
AEP Increase vs SUMR-105 PA	N/A	2.97%	7.80%	13.6%
AEP Hinged - MW·hr/yr	551000	574000	606000	640000
AEP Increase vs SUMR-105 PA	2.42%	6.69%	12.6%	19.0%

3.2 Turbulent Wind

Peak moments under steady wind are a more straightforward way to design for load alignment. However, turbines in actual operation experience time-varying, turbulent wind, which can lead to fatigue damage as well as moments of larger magnitude than in steady wind. The characteristics of the turbulent wind fields, defined in Sect. 2, are consistent throughout this chapter. The rotors defined in Sect. 2, operating with the schedules defined in Fig. 3 (based on the steady-state analysis), will be re-examined in this section using turbulent wind. Peak moments, fatigue damage characterized by DELs, and power generation will be compared to determine if the previously noted trends hold true under more realistic conditions.

Figure 6 shows flapwise bending response of the SUMR-105 rotor at rated wind conditions both in the pre-aligned state ($\beta = 12.5°$) and in the low-cone state ($\beta = 2.5°$) in steady wind (Fig. 6a) and in turbulent wind (Fig. 6b). It can be seen that the turbulence causes the bending moment response to be highly variable, fluctuating a great deal over one rotation. When comparing the response at the two different coning angles, it can be observed that there is a fairly consistent offset with the pre-aligned mean moment being closer to zero. The consistent offset demonstrates that load alignment has a consistent effect even under unsteady conditions.

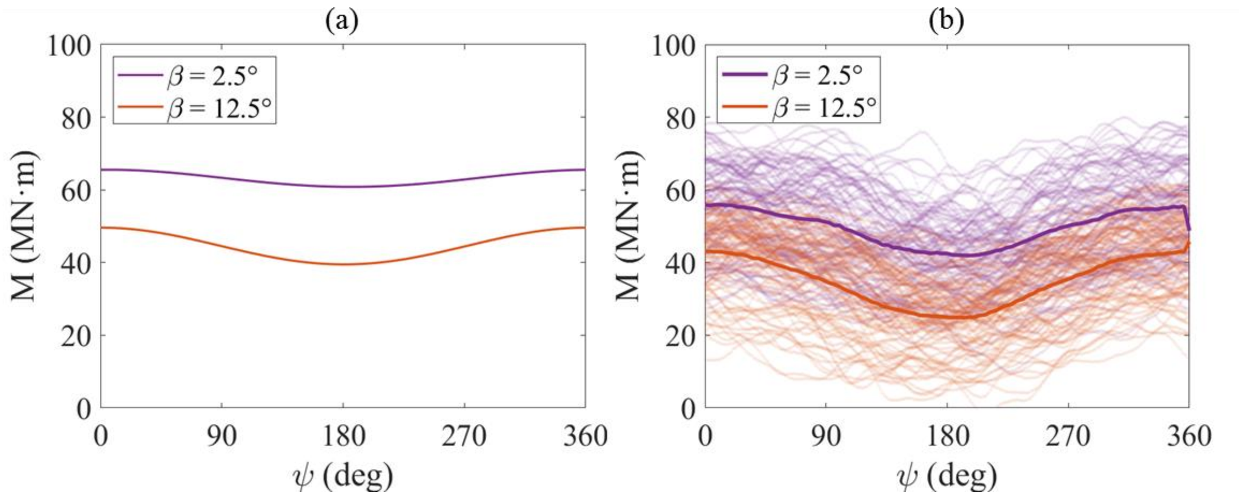

Fig. 6 Instantaneous and average root flapwise bending moment as a function of azimuth angle for the SUMR-105 rotor with nominal wind speed of 11.3 m/s for low-cone and pre-aligned conditions under (a) steady rated wind conditions and (b) turbulent wind conditions

Figure 7 shows the peak bending moments that the four rotors experience both when operating with the pre-aligned angle and with the hinged schedule as calculated from 6 simulations per mean wind speed. The assumption employed in Sect. 3.1 was that two rotors that experience similar peak moments under steady conditions would experience similar peak moments under unsteady turbulent conditions. For the pre-aligned rotor, this assumption holds reasonably well. All four rotors ramp to a peak moment near rated conditions within a tight variance band, as was the case under steady wind conditions. The peak moment of about 73 MN·m for the SUMR-105 PA (the baseline case) is about 46% higher than that in the steady case. If one uses this new peak value as the maximum moment, it can be seen that the other pre-aligned rotors satisfy the moment constraint. The same trend does not hold for the hinged case. At low speeds, the longer blades have significantly higher peak moments compared with the moments experienced near rated conditions. This discrepancy is due to the fact that the coning angle does not adapt to changes in wind speed during a simulation. While FAST could be modified to allow for such adaption, the changes in flow speed due to turbulence may be generally too fast given the large rotational inertia of the rotor. As such, the prediction, while conservative, may reasonably represent an important issue associated with a hinged rotor. However, use of teeter can help reduce these moments (as will be discussed in the next section).

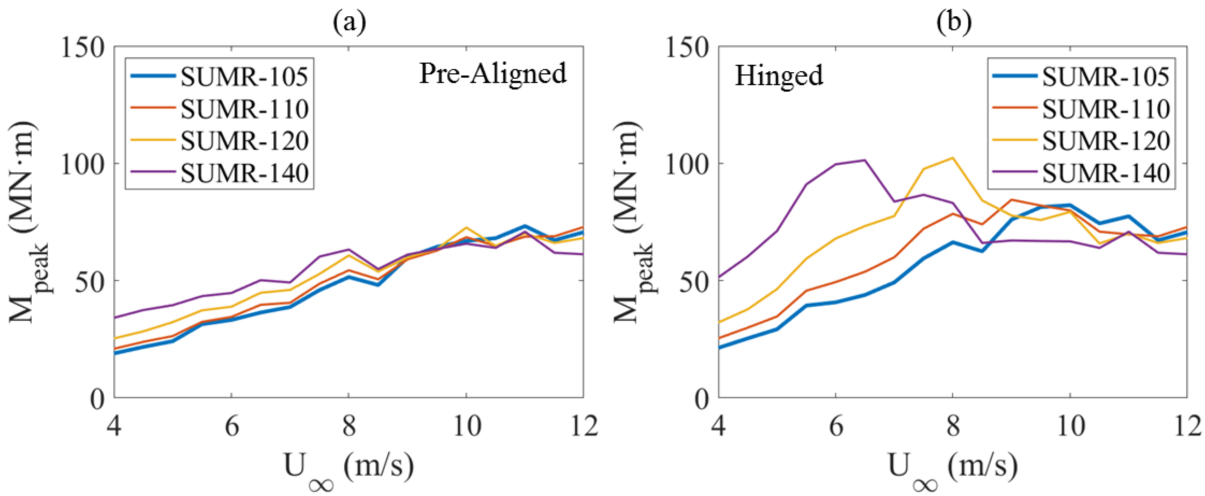

Fig. 7 Peak root flapwise bending moment as a function of nominal turbulent wind speed for the four rotors operating (a) with a pre-aligned schedule (fixed coning angle) and (b) with a hinged schedule (variable coning angle)

While maximum bending moments are an important design consideration; another important (and related) structural design consideration is fatigue life. Figure 8 shows the short-term (over one simulation) DEL of the flapwise bending moment as a function of wind speed for the pre-aligned schedule and the hinged schedule. There is only slight sensitivity of DEL to coning angle, as seen in relatively little difference between the hinged and the pre-aligned cases. However, there is great sensitivity to blade length. The longer blades experience greater shear (vertical gradient of wind speed), veer (vertical gradient of wind direction), and general unsteady variations, leading to large moment fluctuations and higher damage. If the fatigue life is a design driver, the higher DEL indicates that the larger rotors may require additional structural design. It should be noted that advanced control systems may be able to achieve moment reductions to limit moment increases for the pre-aligned system. The use of a hinge tends to reduce DEL at low speeds as compared with that for the pre-aligned case of the same blade length, but it still results in significant net increases relative to the baseline case (pre-aligned SUMR-105). Like the peak case, use of teeter can also help reduce these DELs (as will be discussed in the next section).

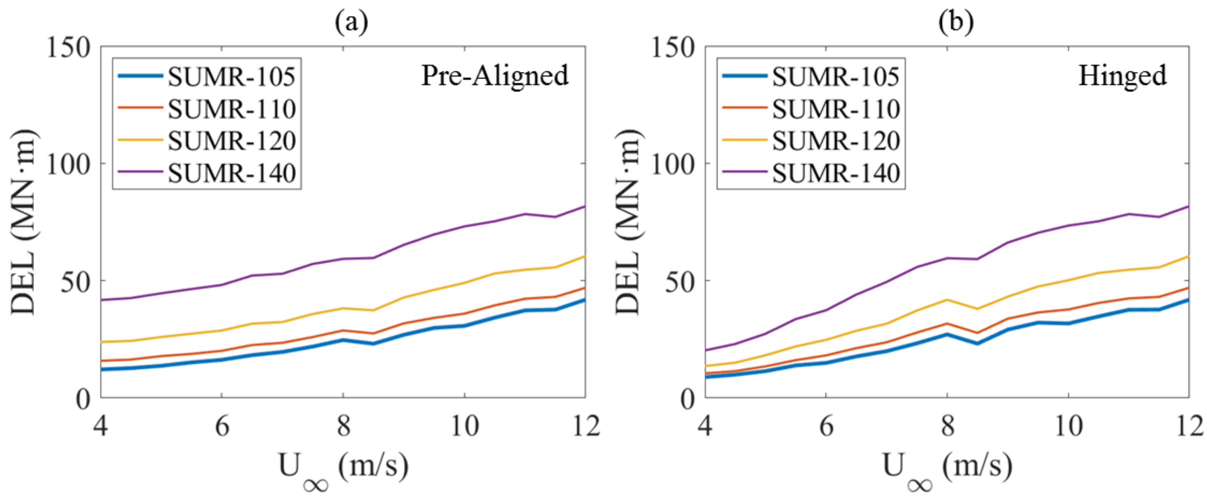

Fig. 8 Short-term DEL of the root flapwise bending moment as a function of nominal turbulent wind speed for the four rotors operating (a) with a pre-aligned schedule (fixed coning angle) and (b) with a hinged schedule (variable coning angle)

Power generation (Fig. 9) in turbulent conditions follows very similar trends as seen in steady conditions. The longer blades consistently produce more power than the shorter blades. The longer blades are operating at a relatively higher coning angle to reduce moments, but still low enough to have a larger projected area. The hinge allows for more power generation especially at the lower speeds.

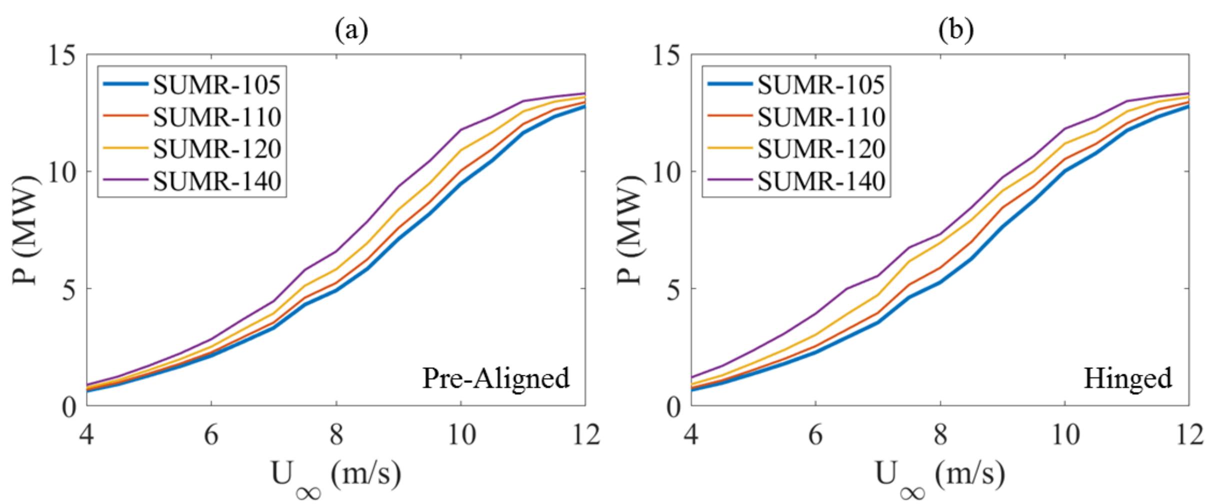

Fig. 9 Average power production as a function of nominal turbulent wind speed for the four rotors operating (a) with a pre-aligned schedule (fixed coning angle) and (b) with a hinged schedule (variable coning angle)

A summary of the rotor performance metrics is shown in Table 4. For the pre-aligned strategies, the SUMR-140 rotor increases the AEP by 13.4% while decreasing the peak moment experienced under normal turbulent conditions by 3% compared with the baseline SUMR-105 pre-aligned rotor. However, the lifetime DEL increased by nearly 100%. The higher DEL suggests that if fatigue was the design driver it could result in a more costly blade.

The inclusion of a hinge on the SUMR-140 rotor increases the AEP increase from 13.4% to 19.4% compared to the pre-aligned case. There is no accompanying increase in DEL as compared to a pre-aligned rotor of the same length. This indicates that either DEL is only weakly dependent on β, or most of the DEL comes from region III, where hinged and pre-aligned rotors were the same. However, there is an increase in peak bending moment of 40%. If the peak moment were a design driver, the increase in peak moment would require reinforcement, which would result in an increase in blade cost. In general, it is expected that the extra power generation could be more than sufficient to off-set the additional cost to reinforce the blades because the rotor cost is typically about 10% of the Capital Expenditures (Stehly *et al.* 2018).

Table 6. Performance summary for the four rotors under unsteady wind conditions, percent difference is based on comparison with the SUMR-105 rotor with the pre-aligned schedule

		SUMR-105	SUMR-110	SUMR-120	SUMR-140
Pre-Aligned	**M_{peak} in MN·m (difference)**	73.25 (N/A)	72.85 (-0.5%)	72.62 (-0.9%)	70.83 (-3.3%)
	DEL in MN·m (difference)	37.11 (N/A)	42.18 (+13.7%)	52.38 (+41.1%)	73.32 (+97.6%)
	AEP in MW·hr/yr (difference)	514900 (N/A)	530600 (+3.05%)	555500 (+7.89%)	584100 (+13.4%)
Hinged	**M_{peak} in MN·m (difference)**	82.16 (+12.2%)	84.49 (15.3%)	102.30 (+39.7%)	101.30 (+38.3%)
	DEL in MN·m (difference)	37.19 (+0.2%)	42.29 (+14.0%)	52.49 (+41.4%)	73.34 (+97.6%)
	AEP in MW·hr/yr (difference)	528100 (+2.56%)	550300 (+6.88%)	582800 (+13.19%)	614700 (+19.38%)

3.3 Morphing Hinge and Impact of Teeter

A key question in evaluating the use of a morphing hinge is whether the improved adaptivity is worth the complexity and cost of the additional degree of freedom and associated actuation/control. This question is important since adding additional components can significantly increase system mass in some cases. For example, teeter requires additional components and complexity but is often used for a two-bladed rotor as it can significantly reduce unsteady bending moments (Anderson *et al.* 1984; Civati *et al.* 2018). If one considers a two-bladed rotor with teeter, a morphing hinge could be designed to be nearly the same size/ weight as a teeter-only hub, with the additional components of actuators/dampers and bearings as shown in Fig. 10. In this manifestation, the hinge allows for both morphing (which allows adjustment of coning angle) and teetering (which allows for the rotor plane to tilt with respect to horizontal). As such, a wind turbine that has the ability to morph could also teeter with little additional system mass.

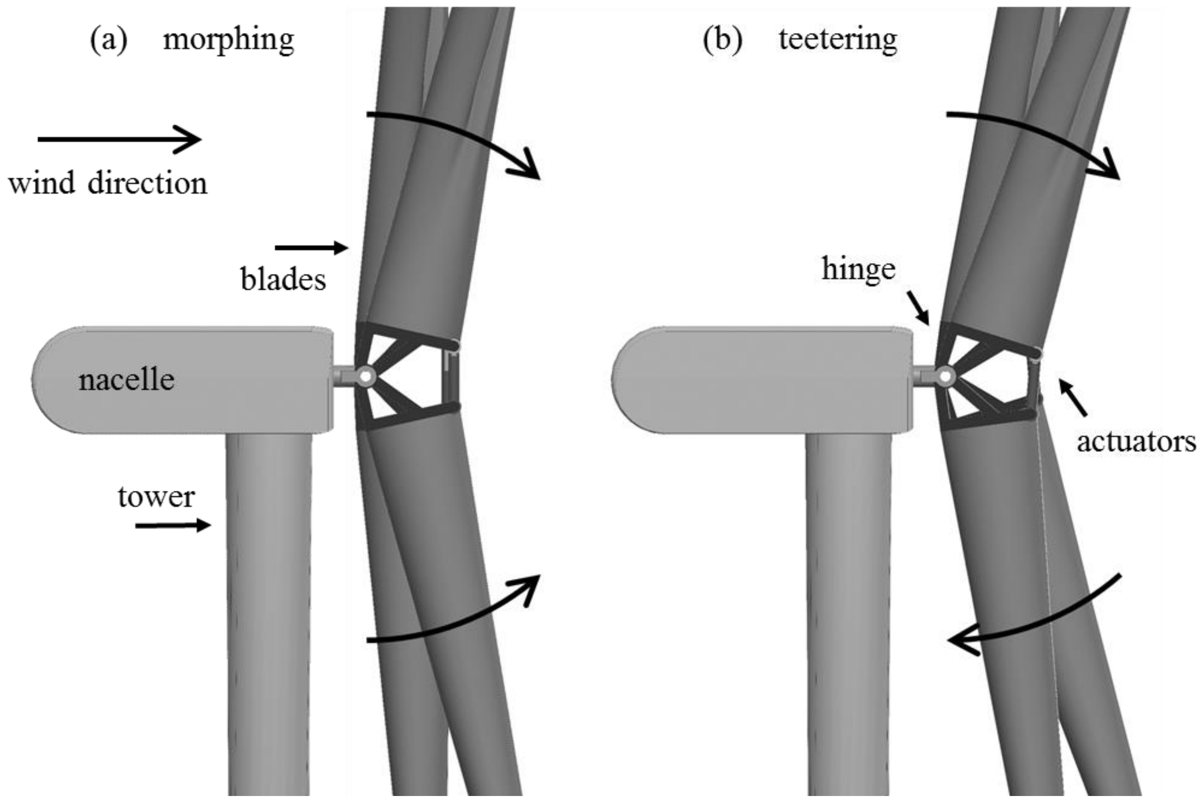

Fig. 10 The morphing hinge design concept allows for two degrees of freedom (a) morphing (changing cone angle) and (b) teetering (changing rotor plane angle)

A key objective of this research was to determine if load alignment can facilitate an increase in power without a corresponding increase in blade moments. The teeter degree of freedom can be used to assist in that objective. Teeter allows for load imbalances between the two blades to dissipated as rotational energy. Teeter can protect the blades from both peak moments and from fatigue damage.

To illustrate the effect of teeter, FAST simulations were conducted for two rotors (SUMR-105 and SUMR-140) with and without the teeter degree of freedom activated. The coning angles for the simulations were determined based on the hinged schedules defined in Fig. 3. Figure 11 shows the results from those simulations. Figure 11a shows the azimuthally binned average root flapwise bending moment with and without teeter. Without teeter, the longer blade experiences a large amount of moment variance, which would lead to large amounts of fatigue. Teeter has relatively little effect on the baseline rotor, however teeter has a massive beneficial effect on the longer blade. The long blade with teeter behaves similarly to the short blade without teeter. The difference in effect from teeter between the two rotors is probably in part due to the greater operating coning angles for the larger rotor.

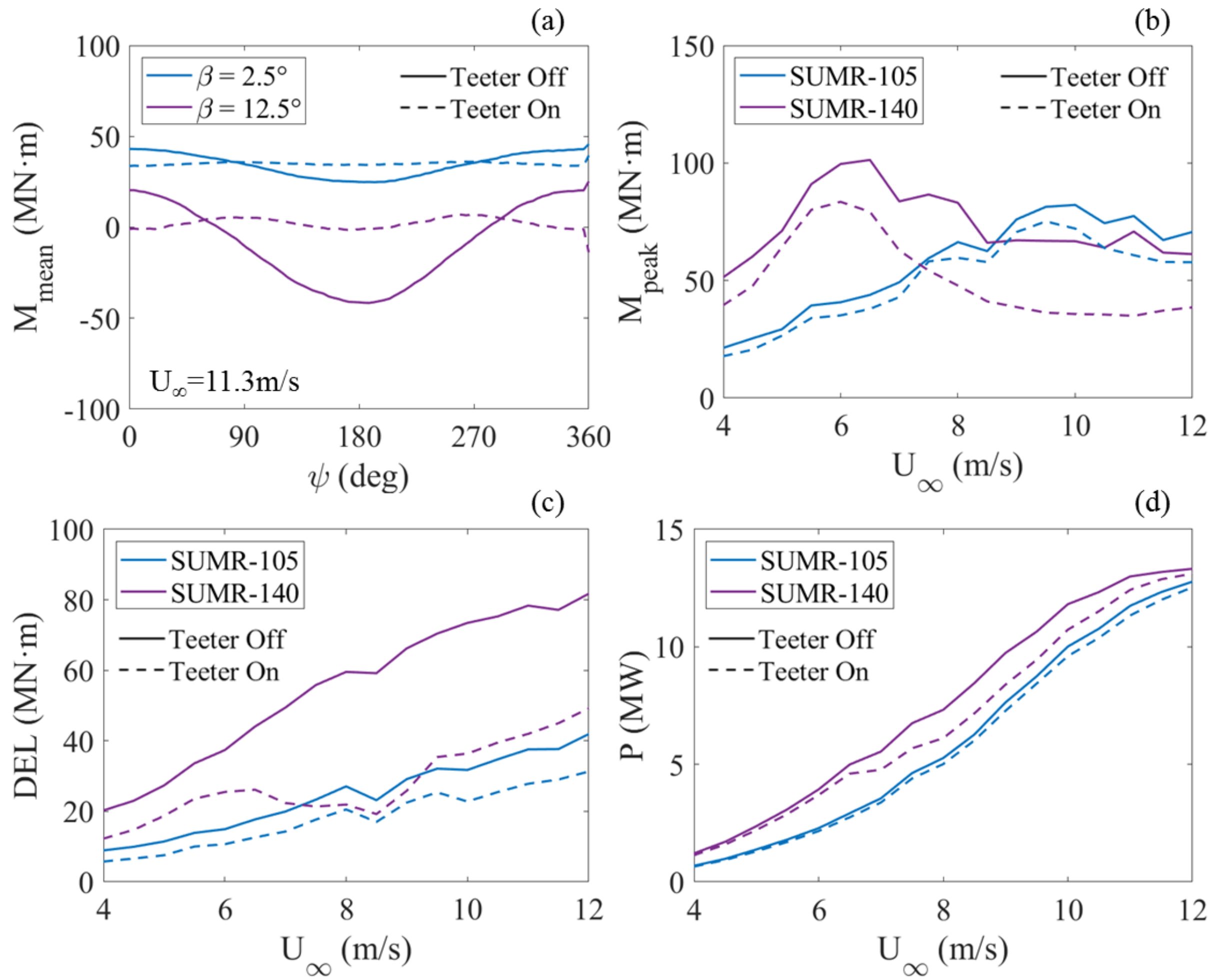

Fig. 11 Performance of two rotors (shortest and longest) in turbulent conditions with and without the teeter degree of freedom using Fig. 3 coning schedule showing (a) azimuthally binned average root flapwise bending moment versus azimuth angle, (b) peak root flapwise bending moment versus nominal wind speed, (c) damage equivalent loading versus nominal wind speed and (d) average power generation versus nominal wind speed

Figure 11b shows the maximum moment experienced from the six simulations conducted for the range of nominal wind speed. Teeter has a large beneficial effect on the long blade and a minor effect on the short blade. The peak moment for the long blade with teeter is similar to the peak moment for the short blade without. Figure 11C shows the fatigue damage with and without teeter. The same trend can be seen; the long blade with teeter behaves similar to the shorter blade without. Figure 11D shows the effect that teeter has on power. The longer blade loses more power due to teeter than that of the shorter blade, however the longer blade (with teeter) still has a higher power curve than the shorter blade (without teeter).

Including teeter with the hinged schedule can decrease the peak moments and fatigue damage to nearly the baseline values, though the morphing power benefits are reduced. These tradeoffs are shown in Table 7. For the longest blade, including a hinge and teeter results in peak moments and fatigue damage that are very similar to the baseline values while increasing the power by 12%. Similar trends are seen with the SUMR-110 and SUMR-120 blades though with lesser power increases relative to the baseline value. While not shown, the pre-aligned rotor with teeter can also achieve peak moments and fatigue damage very similar to the baseline values while increasing the power. However, it should be noted that advanced control systems (potentially coupled with fast outboard actuators) may also be able to achieve such teeter-like moment reductions. This research did not consider such advanced control systems.

Table 7. Performance summary for the four rotors under unsteady wind conditions, using the hinged schedule and the teeter degree of freedom, percent difference is based on comparison with the SUMR-105 rotor with the pre-aligned schedule, without the teeter degree of freedom

	SUMR-105	**SUMR-110**	**SUMR-120**	**SUMR-140**
M_{peak} in MN·m (difference)	75.14 (+2.5%)	80.16 (+9.4%)	91.09 (+24.4%)	83.49 (+14.0%)
DEL in MN·m (difference)	27.89 (-24.8%)	30.09 (-18.9%)	35.21 (-5.1%)	43.09 (+16.1%)
AEP in MW·hr/yr (difference)	515200 (+0.06%)	535200 (+3.9%)	562800 (+9.3%)	577700 (+12.2%)

5. Conclusions

A key objective of this study was to quantify the increase in power capture by use of load alignment and rotor length increase for a two-bladed, downwind, extreme-scale rotor, while minimizing any increases in maximum flapwise blade moments relative to a well-designed baseline rotor. This study used a set of blades aerodynamically designed for lengths ranging from 104 m to 139 m with initial design coning angles ranging from 12.5° to 42.5° so as to yield the same rated power under steady wind conditions. The SUMR-105 rotor was chosen as a baseline as this rotor had been previously shown to be the lightest rotor ever designed and published for a 13.2 MW turbine that satisfied key IEC requirements. The results showed that the new set of longer rotor blades combined with pre-aligned moment strategy increased AEP by 13.4% without increasing the peak moments the rotor experiences for steady conditions. However, the extra length does result in an 82.7% increase in blade mass and a 97% increase in fatigue damage when subjected to turbulent winds, both of which could increase the cost of the blade if these moments are a design driver.

A second objective was to quantify the increase in power production resulting from a morphing hinge. Including a hinge increases the power by an additional 4.6% beyond that of a pre-aligned rotor for the longest blades. However, due to the assumed very slow bandwidth of the hinge that controls the coning angle, rapid wind speed changes make the rotor prone to off-design moment misalignment, which led to peak moments about 40% greater than the baseline values. This increase in fatigue damage and peak moments can be significantly mitigated by allowing the rotor to teeter. In particular, morphing combined with teeter results in an increase in power of about 12% relative to a baseline rotor, without a significant increase in blade peak moments nor in DEL values. This research suggests that a 13.2 MW, downwind, two-bladed rotor can reasonably benefit from a combination of load alignment, longer rotor blades, teeter, and morphing.

To better understand the potential benefits of morphing and to better optimize coning angle schedules, FAST and other rotor dynamics codes should be adapted to allow for variable coning during a simulation. In addition, it is recommended that other DLCs be investigated e.g. extreme gusts with direction changes to establish designs that are robust and closer to industry design practice. It is recommended that further work focuses on how cost is impacted by the extra mass of the blades, loads on other components, and the morphing hinge.

ACKNOWELDGEMNTS

The authors would like to thank ARPA-e for funding and guiding the research reported herein. Any opinions, findings, and conclusions or recommendations expressed in this material are those of the authors and do not necessarily reflect the views of ARPA-e.

FUNDING

Advanced Research Projects Agency – Energy: DE-AR0000667

Ananda, G. K., Bansal, S., & Selig, M. S. (2018). Aerodynamic Design of the 13.2 MW SUMR-13i Wind Turbine Rotor. In *2018 Wind Energy Symposium* (p. 0994).

Anderson, M. B., Garrad, A. D., & Hassan, U. (1984). Teeter excursions of a two-bladed horizontal-axis wind-turbine rotor in a turbulent velocity field. *Journal of wind engineering and industrial aerodynamics*, *17*(1), 71-88.

Arias-Rosales, A., & Osorio-Gómez, G. (2018). Wind turbine selection method based on the statistical analysis of nominal specifications for estimating the cost of energy. *Applied Energy*, *228*, 980-998.

Barlas, T. K., & van Kuik, G. A. (2010). Review of state of the art in smart rotor control research for wind turbines. *Progress in Aerospace Sciences*, *46*(1), 1-27.

Ronold, K. O., & Larsen, G. C. (2000). Reliability-based design of wind-turbine rotor blades against failure in ultimate loading. *Engineering structures*, *22*(6), 565-574.

Chehouri, A., Younes, R., Ilinca, A., & Perron, J. (2015). Review of performance optimization techniques applied to wind turbines. *Applied Energy*, *142*, 361-388.

Chen, J., Wang, F., & Stelson, K. A. (2018). A mathematical approach to minimizing the cost of energy for large utility wind turbines. *Applied Energy*, *228*, 1413-1422.

Civati, M., Sartori, L., & Croce, A. (2018, June). Design of a two-bladed 10 MW rotor with teetering hub. In *Journal of Physics: Conference Series* (Vol. 1037, No. 4, p. 042007). IOP Publishing.

Civelek, Z., Lüy, M., Çam, E., & Mamur, H. (2017). A new fuzzy logic proportional controller approach applied to individual pitch angle for wind turbine load mitigation. *Renewable Energy*, *111*, 708-717.

Crawford, C., & Platts, J. (2008). Updating and optimization of a coning rotor concept. *Journal of Solar Energy Engineering*, *130*(3), 031002.

Drela, M., & Youngren, H. (2001). XFOIL manual.

Eggers, A., Chaney, K., & Digurmarthi, R. (2005, January). An exploratory study of motion and loads on large flap-hinged rotor blades. In *43rd AIAA Aerospace Sciences Meeting and Exhibit* (p. 1184).

Esteban, M., & Leary, D. (2012). Current developments and future prospects of offshore wind and ocean energy. *Applied Energy*, *90*(1), 128-136.

Fingersh, L. J., Hand, M. M., & Laxson, A. S. (2006). Wind turbine design cost and scaling model.

Griffith, D. T. (2013). The snl100-02 blade: Advanced core material design studies for the sandia 100-meter blade. *Sandia National Laboratories Technical Report, SAND2013-10162*.

Griffith, D. T., & Ashwill, T. D. (2011). The Sandia 100-meter all-glass baseline wind turbine blade: SNL100-00. *Sandia National Laboratories, Albuquerque, Report No. SAND2011-3779*, 67.

Griffith, D. T., & Richards, P. W. (2014). The snl100-03 blade: Design studies with flatback airfoils for the sandia 100-meter blade. *Sandia National Laboratory, SAND2014-18129*.

Griffith, D. T., & Ashwill, T. D. (2011). The Sandia 100-meter all-glass baseline wind turbine blade: SNL100-00. *Sandia National Laboratories, Albuquerque, Report No. SAND2011-3779*, 67.

Griffith, D.T. (2019). “Mass Reduction for 2-bladed Downwind Rotors”. (unpublished)

Ichter, B., Steele, A., Loth, E., Moriarty, P., & Selig, M. (2016). A morphing downwind- aligned rotor concept based on a 13- MW wind turbine. *Wind Energy*, *19*(4), 625-637.

International Electrotechnical Commission. (2005). Wind Turbine—Part 1: Design Requirements, IEC 61400-1. *International Electrotechnical Commission, Geneva, Switzerland*.

Jonkman, J., Butterfield, S., Musial, W., and Scott, G. (2009). *Definition of a 5-MW reference wind turbine for offshore system development*. Technical Report NREL/TP-500-38060, NREL.

Loth, E., Steele, A., Qin, C., Ichter, B., Selig, M. S., & Moriarty, P. (2017). Downwind pre-aligned rotors for extreme- scale wind turbines. *Wind Energy*, *20*(7), 1241-1259.

Manwell, J. F., McGowan, J. G., & Rogers, A. L. (2010). *Wind energy explained: theory, design and application*. John Wiley & Sons.

Martin, D. P., Johnson, K. E., Zalkind, D. S., & Pao, L. Y. (2017, May). LPV-based torque control for an extreme-scale morphing wind turbine rotor. In *American Control Conference (ACC), 2017* (pp. 1383-1388). IEEE.

Murdani, A., Hadi, S., & Amrullah, U. S. (2017). Flexural properties and vibration behavior of jute/glass/carbon fiber reinforced unsaturated polyester hybrid composites for wind turbine blade. In *Key Engineering Materials* (Vol. 748, pp. 62-68). Trans Tech Publications.

Noyes, C., Qin, C., & Loth, E. (2017). Low Mass, Morphing Rotor for Extreme Scale Wind Turbines. In *35th Wind Energy Symposium* (p. 0924).

Noyes, C., Qin, C., & Loth, E. (2018). Pre-aligned downwind rotor for a 13.2 MW wind turbine. *Renewable Energy*, *116*, 749-754.

Pao, L. and Johnson, K., “Control of wind turbines: Approaches, challenges, and recent developments,” *IEEE Control Systems Magazine*, Vol. 31, no. 2, April 2011, pp. 44-62.

Selig, M. S. (1999). PROFOIL-A Multipoint Inverse Airfoil Design Method, User’s Guide. *Cleveland Ohio, Feb*.

Selig, M. S. (2012). Propid user manual. *Aerodynamic Design Software for Horizontal Axis Wind Turbines Version*, *5*(1).

Shulong Yao, D. Todd Griffith, Mayank Chetan, Christopher Bay, Rick Damiani, Meghan Kaminski, Eric Loth (2019). Structural Design of a 1/5th Scale Gravo-Aeroelastic Scaled Wind Turbine Demonstrator Blade for Field Testing. Accepted in *2019 Wind Energy Symposium*.

Sieros, G., Chaviaropoulos, P., Sørensen, J. D., Bulder, B. H., & Jamieson, P. (2012). Upscaling wind turbines: theoretical and practical aspects and their impact on the cost of energy. *Wind energy*, *15*(1), 3-17.

Stehly, T. J., Beiter, P. C., Heimiller, D. M., & Scott, G. N. (2018). *2017 Cost of Wind Energy Review* (No. NREL/TP-6A20-72167). National Renewable Energy Lab.(NREL), Golden, CO (United States).

Zalkind, D. S., Pao, L. Y., Martin, D. P., & Johnson, K. E. (2017). Models used for the simulation and control of a segmented ultralight morphing rotor. *IFAC-PapersOnLine*, *50*(1), 4478-4483.

Zhang, M., Tan, B., & Xu, J. (2016). Smart fatigue load control on the large-scale wind turbine blades using different sensing signals. *Renewable Energy*, *87*, 111-1

Chapter 6

A method to analyze experimental data for load-aligned wind turbines

Abstract

Extreme-scale wind turbines have grown in popularity over the last decade. Load-alignment is an effective concept to lower average loads allowing for longer blades with larger than before possible rated powers. The first gravo-aeroelastically-scaled, experiment of an extreme-scale wind turbine is underway. This unique experiment requires unique methods to analyze the data. With load-alignment it is necessary to separate the out-of-plane bending loads into their fundamental components (thrust, centrifugal and gravitational). The data analysis approach developed herein allows the measured resultant moment at a fixed coning angle to be decomposed into the fundamental components, and uses these components to estimate the resultant bending load the rotor would have experienced at a variety coning angles. The methodology was demonstrated using simulated data. The results show that a coning angle of 12.5° (testing conditions) results in a bending load that is 75% less than the load would have been without coning, and that a coning angle of 15° would result in near-zero average bending load over all wind speeds.

1. Introduction

1.1 Load-Aligned Turbine

A commonly noted trend is that average wind turbine size has been consistently growing over the last several decades (Arias-Rosales & Osorio-Gómez, 2018; Barlas & van Kuik, 2010). This trend is driven economically, the increase in power generation outweighs the cost for the larger turbine. There is a size limit to that tradeoff, however over time with technological innovations the optimal sized turbine has been increasing (Sieros *et al.* 2012). One primary design driver limiting the size of wind turbines is the out of plane bending loads. The out of plane bending load from thrust forces scale with blade length cubed. An average rotor diameter in 1980 was 15m (Quarton & Hanssan, 1998), today General Electric has plans to build a wind turbine with a diameter of 220m. The 15-fold increase in blade length has led to bending loads that are structurally difficult to manage. The blade has to be both strong enough to withstand the load and also stiff enough not to deflect backwards and strike the tower. This becomes more difficult as bending moments increase.

A proposed solution to the address the increasing out-of-plane bending loads and tower-clearance concerns resulting from a conventional rotor design is to instead employ a load-aligned rotor (Fig. 1). The load-alignment concept is a suggested solution to mitigate the immense thrust loads characteristic of extreme-scale wind turbines (Ichter *et al.* 2016). A rotor that is coned downwind has a centrifugal bending moment that generally opposes the bending moment resulting from thrust forces (Loth *et al.* 2017). Because the gravitational moment is oscillatory in the rotating blade coordinate frame, there is no coning angle that will result in zero bending moment for all azimuth positions. However, if one considers the mean azimuthal position, gravity is neglected and there exists a coning angle (β) where the thrust and centrifugal combination cancel out so that the average bending load is zero. Because the ratio between thrust and centrifugal loads is dependent on wind speed, the coning angle that results in load-alignment (zero azimuthally averaged bending moment) is a function of wind speed.

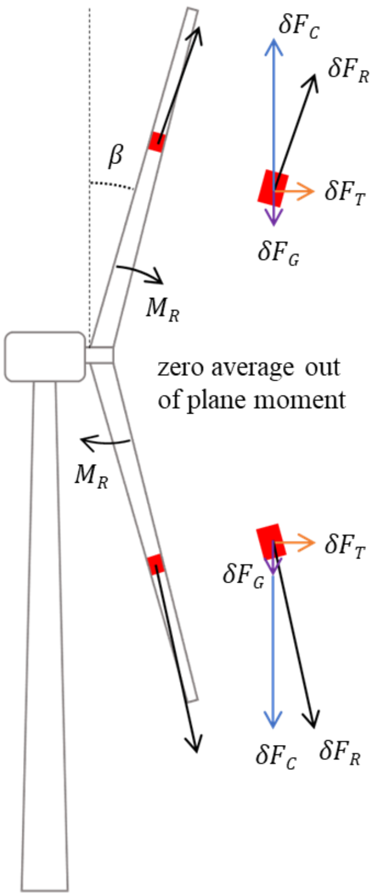

Figure 1. Load-aligned downwind coned rotor whereby the azimuthal average out-of-plane bending moment is zero due to balance of centrifugal and thrust components.

A downwind rotor with a constant pre-cone angle (pre-aligned rotor) can be load-aligned at a single wind speed, and this yields many advantages. One study showed a pre-aligned rotor could satisfy structural and power constraints using 25% less material than a similar low-coned rotor (Noyes *et al.* 2018a). Another study showed that increasing the coning angle and blade length together could result in a 13% increase in annual energy production (AEP) without increasing the average out of plane bending moments (Chapter 5). Several studies (Eggers *et al.* 2005; Crawford & Platts, 2008) have noted the advantages of load-alignment either analytically or computationally, but there have been no detailed experimental analyses of the concept.

1.2 Gravo-Aeroelastic Scaling

The most direct test of the potential of load-alignment is to build and field test a full-scale experiment. However, a full-scale experiment of an extreme-scale (>10MW) wind turbine would be incredibly expensive and it is difficult to replicate the important dynamics on a conventional subscale test. This is because extreme-scale wind turbines have a much more significant ratio of thrust to centrifugal loads, than the ratios for turbines with rating of a few MW. Thus, the extreme-scale blades experience large relative downwind loads and deflections. Because of the long blade length and large mass, the blade's natural frequencies are low. In some cases, these flapwise frequencies can be near the operating range of the rotor, and the flutter margin can be low. The low natural frequencies and flutter margin could lead to unpredictable and unsteady dynamics for extreme-scale wind turbines. Therefore, it is important to understand the dynamics and deflection of an extreme-scale rotor and to determine if load-alignment can help to reduce these.

Sub-scale experiments typically can replicate one aspect of the full scale system well (e.g. aerodynamics) but struggle to replicate the entirety of the system (Hassanzadeh *et al.* 2016). As explained above, extreme-scale wind turbines have important dynamics that are a factor of the aerodynamic and structural interplay. To best capture these dynamics and deflections, it is therefore important to carefully scale all blade parameters (mass, stiffness, rotational rate etc.) such that the ratios of loads are reasonably maintained (centrifugal, thrust, gravitational etc.). In this way, the resulting deflections will be scaled in terms of both average and unsteady fluctuations. The scaling methodology (Loth *et al.* 2017) ensuring dynamic similitude is called Gravo-Aeroelastic Scaling (GAS).

Gravo-Aeroelastic Scaling ensures that key dimensionless parameters are maintained: outer blade geometry, tip speed ratio, non-dimensional frequencies, deflection angles, and load ratios (Kaminski *et al.* 2018). These values are maintained by prescribing the scaling of certain parameters (EQ. 1 a-e) using subscripts s & f to indicate subscale and full-scale respectively, R is rotor radius, U_∞ is windspeed, ω is rotational rate, ρ is air density, m is blade mass, E is the modulus of elasticity and I is the second moment of inertia (herein, for flapwise movement):

geometric lengths: $$\eta \equiv \frac{R_s}{R_f} \tag{1a}$$

wind speed: $$U_{\infty,s} = U_{\infty,f}\sqrt{\eta} \tag{1b}$$

rotational rate: $$\omega_s = \frac{\omega_f}{\sqrt{\eta}} \tag{1c}$$

blade mass: $$m_s = m_f\left(\frac{\rho_s}{\rho_f}\right)\eta^3 \tag{1d}$$

blade stiffness: $$(EI)_s = (EI)_f\left(\frac{\rho_s}{\rho_f}\right)\eta^5 \tag{1e}$$

SUMR-D is the first experimental demonstration of the load-alignment concept and is also the rotor that was scaled using GAS from an extreme-scale turbine. In particular, it is scaled based on the SUMR13i (Yao *et al.* 2019) rotor with geometric scaling factor η = 0.2. The rotor is planned to be tested at the National Wind and Technology Center in Golden, CO, on the CART-2 wind turbine. Due to manufacturing and safety constraints, as well as fixed turbine parameters e.g. hub radius, the SUMR-D is not an exactly scaled replica of the SUMR-13i. The parameter whose target was most difficult to achieve was the very low linear mass density distribution. This is because sufficient material was needed at the root for bolt connections and throughout the blade to ensure the panels do not buckle and that the blade can handle the extreme winds that can occur (gusts in excess of 40 m/s) at the NWTC. Another limitation of the SUMR-D rotor test is that the coning angle is fixed. As such, one may not measure a range of coning angles to determine which angle provides average load-alignments, whereby the mean flapwise bending load is zero.

1.3 Project Objectives

This chapter proposes a unique methodology of analyzing experimental data focusing on load-alignment. Specifically this chapter develops the equations necessary to deconstruct the measured out-of-plane bending moment of a coned rotor into its fundamental components (thrust, centrifugal and gravitational). The fundamental components can be used to approximate the magnitude the bending load would be at a different coning angle, but under similar inflow conditions. This analysis is the first that extends experimental data to the rotor at differing coning angles. The developed methodology is constrained to use only data channels available to the SUMR-D experiment. The equations are demonstrated using data of the SUMR-D simulated from FAST.

2. Analytical Analysis

The objective of this section is to develop a methodology that uses experimental data to estimate the bending loads resulting from centrifugal, thrust and gravitational loads. The methodology will be constrained to data available for the SUMR-D experiment. This constraint was selected such that this methodology can be directly applied to the SUMR-D when the test is completed.

Detailed structural properties for the SUMR-D are available (Yao *et al*. 2019), mass and stiffness distribution. With mass and stiffness, blade mode shapes can be calculated. Figure 2 shows the SUMR-D mass distribution (Panel A) and the first flapwise mode of the blade (Panel B). Time series data of root flapwise bending moment (M), tip deflection (Δ_{tip}) will be measured using strain gauges and hub mounted cameras respectively, azimuth angle (ψ) and rotational rate (ω) will also be measured. Additionally a time series of reference wind speed (U_{ref}) will be measured by nearby towers. This reference wind speed is not exactly the wind speed that the rotor sees (U_{∞}), and therefore should not be used in the calculation but instead as a way to categorize the results.

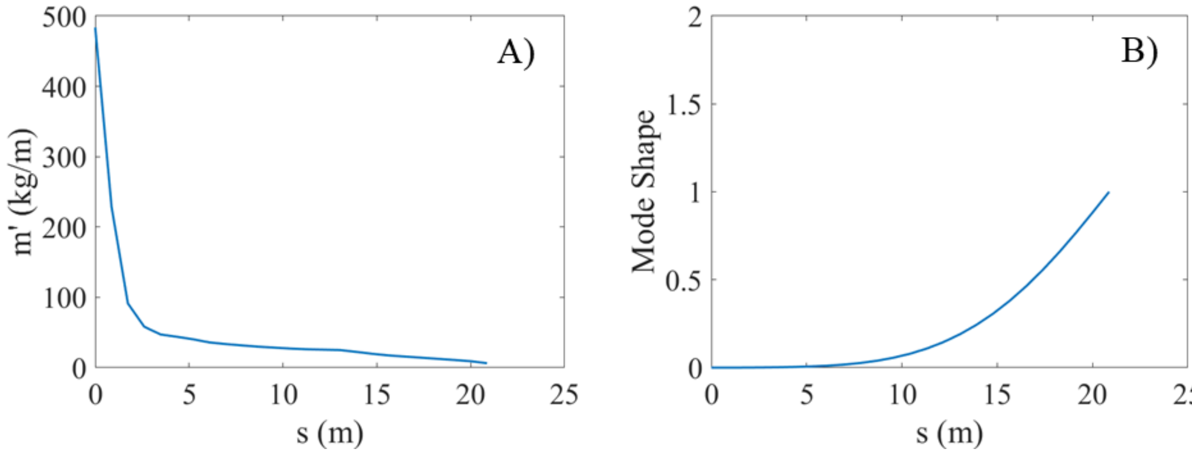

Figure 2. Structural properties of the SUMR-D rotor blade: A) linear mass density and B) first flapwise mode shape.

Figure 3 shows a schematic of a downwind turbine. Panel A, shows the coordinate directions (r, s and n) and geometric parameters hub radius (R_h), coning angle (β) and shaft tilt (τ) for the condition where there is no aeroelastic deflection. Panel B shows how the location of a blade element that translates due to flapwise aeroelastic deflection. The location of the deflected blade element retains its spanwise location (s) but has an local aeroelastic deflection angle (β_Δ) such that the effectively new coning angle is β +β_Δ. Panel C shows a free body diagram of this differential blade element in reference to it deflected radial and normal location (r, n) and the differential forces that lead to out-of-plane moments are centrifugal (δF_C), gravitational (δF_G) and thrust (δF_T).

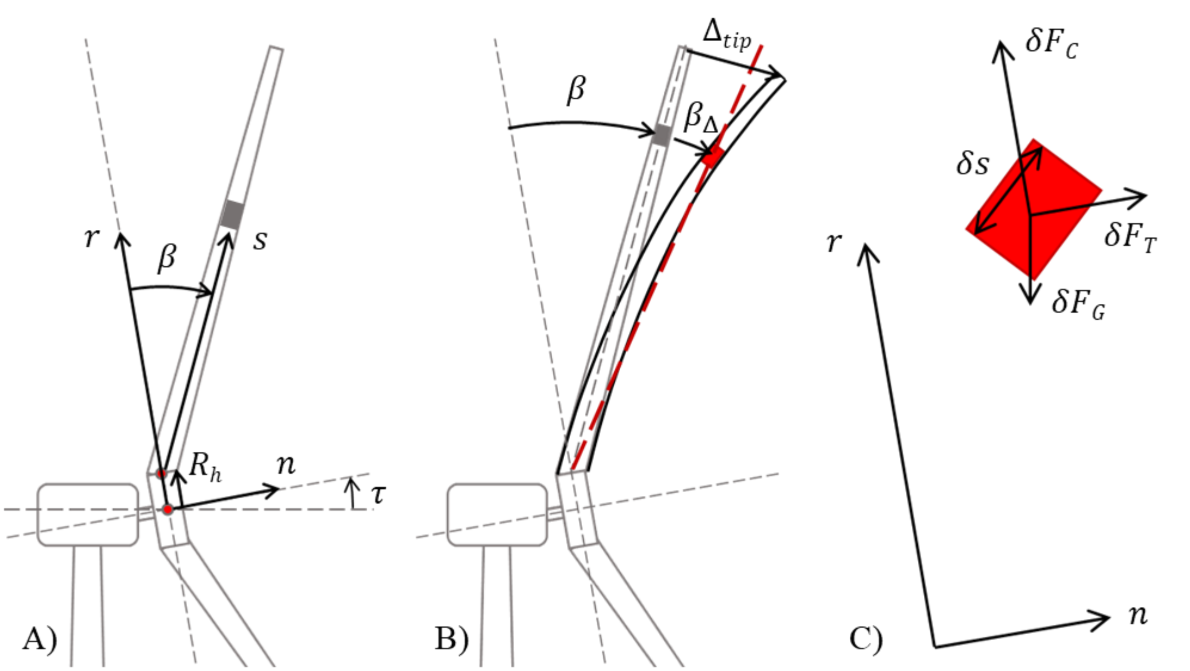

Figure 3. downwind coned rotor schematic: A) general geometric definitions, B) geometric definitions involving blade deflection and C) free body diagram of differential blade element.

The differential forces on a differential blade element are defined below as a function of rotational rate (ω), linear mass density (m'), radial location (r), acceleration due gravity (g), and thrust distribution (F_T'). The prime operator indicates spanwise derivative (i.e. $q' \equiv \frac{dq}{ds}$).

$$\delta F_C = m' \, \omega^2 \, r \, \delta s \tag{2a}$$
$$\delta F_G = m' \, g \, \delta s \tag{2b}$$
$$\delta F_T = F_T' \, \delta s \tag{2c}$$

While centrifugal and gravitational force components can be determined directly from orientation and rotation rate, thrust distribution will not be directly measured. This poses a significant challenge in the load-alignment analysis, which must be addressed later.

The radial position is a function of known values of the hub radius (R_h) and coning angle (β) and the unknown deflection angle. This position and the deflection angle can be related to the local deflection angle (β_Δ) and distance (Δ) as

$$r = R_h + s \cos(\beta + \beta_\Delta) \tag{3a}$$
$$\beta_\Delta = atan\left(\frac{\Delta}{s}\right) \tag{3b}$$

Note that local deflection and its angle are not directly measured in the SUMR-D test, instead it must be modeled using a measurement of tip deflection (Δ_{tip}). The assumption used herein is that the out of plane deflection profile can be reasonably modeled as the first flapwise mode shape. Thus, a given shape and a given tip deflection specify the local deflection and angles.

The differential out-of-plane moment resulting from the forces on the differential blade element (Appendix of Chapter 1) are given as

$$\delta M_C = -\omega^2 \, s \, (R_h + s \, cos(\beta + \beta_\Delta)) \, sin(\beta + \beta_\Delta) \, m' \delta s \tag{4a}$$
$$\delta M_G = g \, s \, (sin(\beta + \beta_\Delta) \, cos(\tau) \, cos(\psi) - cos(\beta + \beta_\Delta) \, sin(\tau)) \, m' \delta s \tag{4b}$$
$$\delta M_T = s \, cos(\beta + \beta_\Delta) \, F_T' \, \delta s \tag{4c}$$

Note that the differential thrust moment cannot be calculated directly because F_T' is not available from the experimental data measurements.

The differential moments can be integrated over the span of the blade to yield the three components of the total root out of plane bending moment (M_C, M_G & M_T). The addition of these three components yields the resultant out-of-plane bending moment (M). Since M can be experimentally measured with strain gauges placed at the root, M_T can be approximated as

$$M_T = M - M_C - M_G \tag{5}$$

With all three moments defined, the load alignment analysis can be performed. If one ignores the effects of hub radius and shaft tilt, which is reasonable to within 5% accuracy, the components of M can be expressed as some coefficient multiplied by a trigonometric function of coning angle as

$$M_C = K_C \tan(\beta) \tag{6a}$$
$$M_G = K_G \sin(\beta) \tag{6b}$$
$$M_T = K_T \cos^3(\beta) \tag{6c}$$

The K coefficients are independent of coning angle but are a function wind speed, rotational rate and azimuth angle.

The above equations can be used to develop an expression that predicts the load that the rotor would experience at different coning angle, but at the same wind speeds and similar turbulence levels. For example the expressions can be used to predict at what angle would the average load have been zero (β_{LA}). These values can be predicted using only the data measured experimentally from the SUMR-D experiment.

3. Simulation Results

To demonstrate the load-alignment analysis methodology developed in the previous section, this section applied the methodology with simulated data. FASTv8 (Jonkman *et al.* 2005) was used to simulate the SUMR-D experiment. To mimic the experiments, only FAST data that will be experimentally available from the SUMR-D field tests was used in the present analysis. Simulations were conducted with turbulent wind fields consistent with that expected for operational conditions. Data are then binned using the reference wind speed at the hub height (U_{ref}) with bin size of 0.5m/s.

The general turbine parameters used in fast are shown in Table 1 (Yao *et al.* 2019).

Table 1. SUMR-D turbine parameters.

Rated Power	55.9 kW
Rated Wind Speed	5.05 m/s
IEC Wind Condition	Class IIA
Rated Rotational Rate	21.5 rpm
Blade Number	2
Blade Length	20.9 m
Coning Angle	12.5°
Hub Height	34.9 m
Hub Radius	1.9 m
Shaft Tilt Angle	3.8°

Two FAST data output channels are shown in Fig. 4 and include the out of plane bending moment (panel A) and tip deflection (panel B). Both of these two channels will be experimentally measured in the SUMR-D experiment and directly relate to the load-alignment analysis. Therefore, this is a simulation of the available experimental data. Both parameters follow a similar average trend. The mean values (solid line) parameters start relatively low, ramp to a maximum near rated conditions, decrease above rated, crossing zero near $1.5U_{rated}$. Due to high levels of turbulence, there is a significant range of values at each wind speed, and this range is much larger than the mean value at all wind speeds.

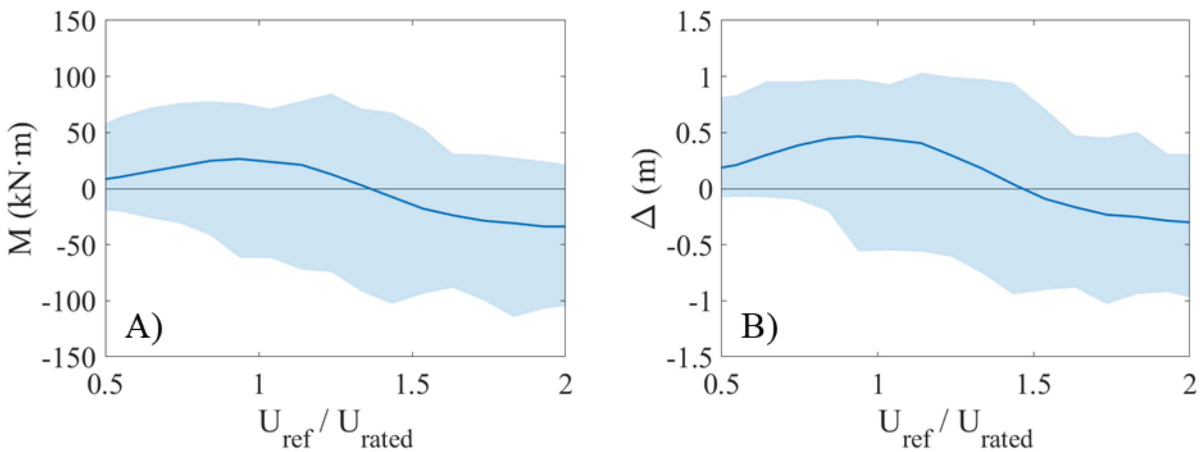

Figure 4. SUMR-D structural performance as a function of reference wind speed for SUMR-D simulated data: A) out of plane bending moment and B) tip deflection. The solid line indicates averaged values and the shaded region indicates the simulated range due to turbulent fluctuations.

Using the simulated data from FAST and the equations outlined in the previous section, the individual flapwise load components are shown in Fig. 5. Centrifugal and gravitational loads were calculated using Eqs. 4 a&b, while the thrust load was calculated using Eq. 5. As expected, the thrust moment ramps up to a maximum value near rated conditions after which it decreases. The centrifugal load ramps down to a maximum (negative) value near rated after which it is constant because rotational rate is constant in region III. The gravitational component's weak dependence on wind speed is due to the effects of aeroelastic deflection. The individual components can be used to calculate load ratios such as M_T/M_C.

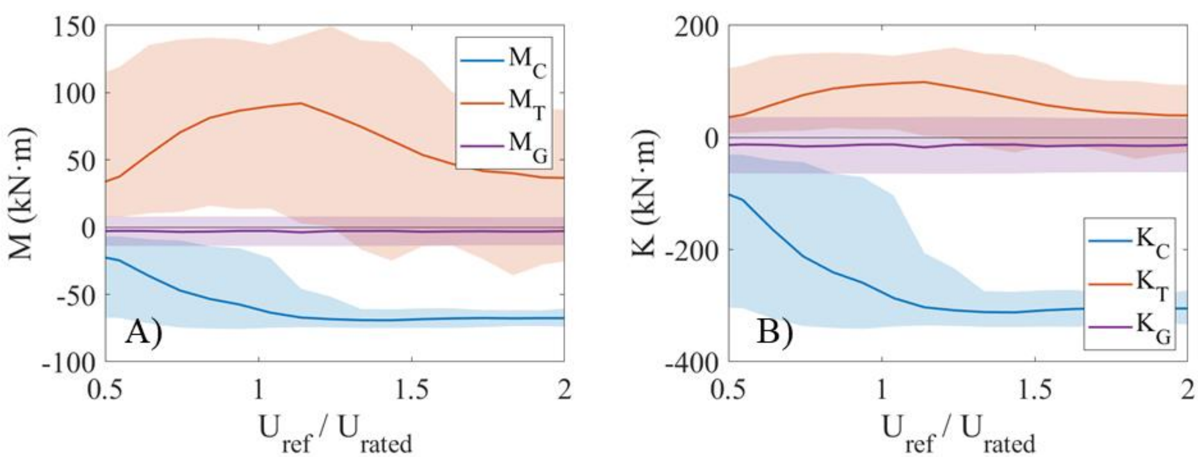

Figure 5. individual load components (A) and coefficients (B) calculated for SUMR-D simulated data, where mean and range of values are denoted by line and shaded regions.

The instantaneous load coefficients (K_C, K_T & K_G) were calculated from the instantaneous load components using Eq. 6 a-c and are shown in the above figure. Conceptually, the load coefficients are the magnitude of the individual bending load components at the coning angle that results in the their greatest value. The coning angles that maximize the individual load components are $\beta = 0°, 45°$ & $90°$ for thrust, centrifugal and gravity loads respectively. Since the coefficients are independent of coning angle for a given wind speed and rpm value, they can be used to predict the load the turbine would experience under similar conditions operating but with different coning angle.

Using the load coefficients with a range of coning angles provides important results regrading proximity to load-aligned conditions. Figure 6a shows what the load on the rotor would be if the coning angle were 0° compared with the actual value of 12.5°. The average load can be reduced by roughly 75% by coning the rotor to 12.5°. Figure 6b shows the coning angle for which the average flapwise moment would be zero. It is interesting to note that the load-alignment angle is fairly constant (at about 15° -18°) as a function of wind speed in Region II (between cut-in conditions and rated conditions). This is because both thrust and centrifugal bending loads increase with the square of wind speed, so their ratio is relatively constant leading to a nearly constant load-path angle. However, Region III (beyond rated wind speed) causes the load-alignment angle to decreases since the centrifugal load is maintained (for nearly constant rpm) while the thrust load decreases (for nearly constant power output).

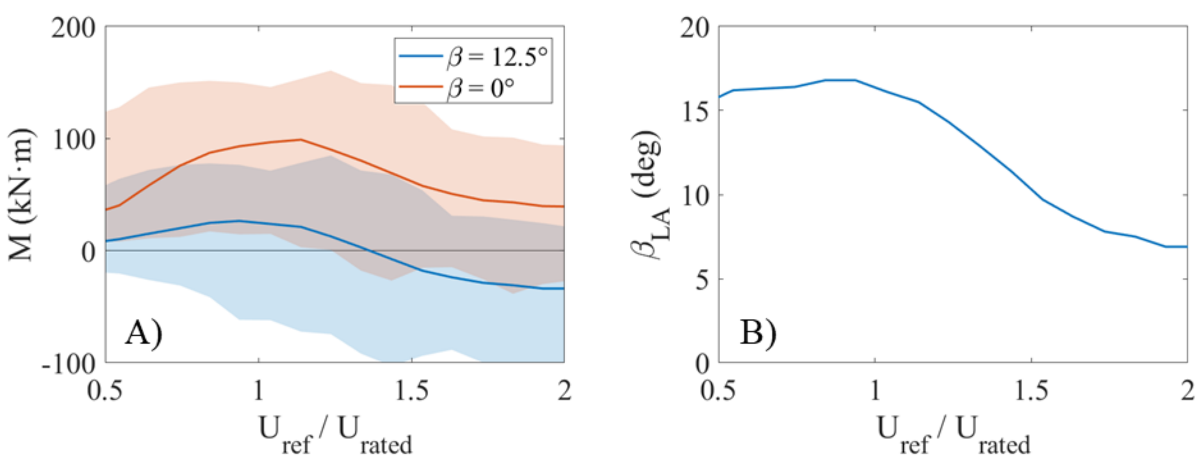

Figure 6. load-alignment analysis for SUMR-D simulated data: A) out of plane bending moment for simulated rotor (blue) and predicted no-coned rotor (orange) and B) estimated coning angle that would result in zero average out of plane bending load. The mean and range of values are denoted by line and shaded regions.

Thus, highly coned downwind rotors above rated wind speeds can result in average bending loads that are negative. For example, a rotor with 12° of coning will have a net moment and aeroelastic deflection in the upwind direction for Region III, based on a conventional controller (which has an objective to reduce bending loads while constraining the power to a nearly constant rated value and constraining rpm to a constant value). This suggest a different control strategy could be used for load-aligned extreme-scale turbines. In particular, a different strategy could allow variation of rpm and pitch in Region III so as to constrain the ratio of centrifugal to thrust loads to a constant value that is consistent with a pre-aligned coning angle, while still constraining the power to be nearly equal to the rated value. This would minimize the absolute value of the out-of-plane bending load, while still yielding a level power output. This strategy could decrease blade fatigue damage as well as increase pitch actuator/bearing life.

4. Conclusions

Load-alignment, countering the thrust moment with a centrifugal moment, is a novel concept that can be very helpful for reducing flapwise loads for extreme-scale wind turbines. This alignment is generally incorporated through a downwind rotor with a significant coning angle. In order to asses load-aligned performance with a sub-scale demonstrator, it is important to note that highly-coned, lightweight, downwind rotors are expected to have very different aeroelastic and dynamic behavior as compared to conventional wind turbine rotors. Load-aligned wind turbines will have highly coupled aerodynamic and structural dynamic interplay. The SUMR-D is the first such sub-scale field demonstrator that has been scaled to preserve the dynamic interplay of an extreme-scale, load-aligned wind turbine.

Herein, a methodology was developed to analyze load-alignment using the experimental data of the SUMR-D operational test campaign. The available data include rpm, root moments and tip deflections, and ground-tested flapwise shape modes of the blades. The method developed herein uses the instantaneous data from a single coning angle to provide an approximation of the instantaneous moments for a wide range of coning angles.

The SUMR-D turbine was simulated using FAST to provide data channels that will be available in the full experiment data set during operation. The results of the method show that average bending load of the simulated rotor with 12.5° coning has an average bending load that is only 25% of that for the same rotor with no coning angle, demonstrating the benefit of load alignment on the mean moments. Additionally, it was found that the ideal coning angle that would result in zero average bending load is nearly constant in Region II, and decreases with wind speed in Region III. However, atmospheric turbulence leads to large deviations of bending moments away from the moments, the coning has little effect on these deviatoric moments.

References

Arias-Rosales, A., & Osorio-Gómez, G. (2018). Wind turbine selection method based on the statistical analysis of nominal specifications for estimating the cost of energy. *Applied Energy*, *228*, 980-998.

Barlas, T. K., & van Kuik, G. A. (2010). Review of state of the art in smart rotor control research for wind turbines. *Progress in Aerospace Sciences*, *46*(1), 1-27.

Crawford, C., & Platts, J. (2008). Updating and optimization of a coning rotor concept. Journal of Solar Energy Engineering, 130(3), 031002.

Eggers, A., Chaney, K., & Digurmarthi, R. (2005, January). An exploratory study of motion and loads on large flap-hinged rotor blades. In 43rd AIAA Aerospace Sciences Meeting and Exhibit (p. 1184).

Hassanzadeh, A., Naughton, J. W., Kelley, C. L., & Maniaci, D. C. (2016, September). Wind turbine blade design for subscale testing. In *Journal of Physics: Conference Series* (Vol. 753, No. 2, p. 022048). IOP Publishing.

Ichter, B., Steele, A., Loth, E., Moriarty, P., & Selig, M. (2016). A morphing downwind- aligned rotor concept based on a 13- MW wind turbine. *Wind Energy*, *19*(4), 625-637.

Jonkman, J. M., & Buhl Jr, M. L. (2005). FAST user's guide. *National Renewable Energy Laboratory, Golden, CO, Technical Report No. NREL/EL-500-38230*.

Kaminski, M., Loth, E., Qin, C., & Griffith, D. T. (2018). Gravo-Aeroelastic Scaling a 13.2 MW Wind Turbine Blade to a 1-meter Model. In *2018 Wind Energy Symposium* (p. 1731).

Loth, E., Fingersh, L., Griffith, D., Kaminski, M., & Qin, C. (2017). Gravo-Aeroelastically Scaling for Extreme-Scale Wind Turbines. In *35th AIAA Applied Aerodynamics Conference* (p. 4215).

Loth, E., Steele, A., Qin, C., Ichter, B., Selig, M. S., & Moriarty, P. (2017). Downwind pre-aligned rotors for extreme- scale wind turbines. *Wind Energy*, *20*(7), 1241-1259.

Noyes, C., Qin, C., & Loth, E. (2018). Pre-aligned downwind rotor for a 13.2 MW wind turbine. *Renewable Energy*, *116*, 749-754.

Sieros, G., Chaviaropoulos, P., Sørensen, J. D., Bulder, B. H., & Jamieson, P. (2012). Upscaling wind turbines: theoretical and practical aspects and their impact on the cost of energy. *Wind energy*, *15*(1), 3-17.

Yao, S., Griffith, D. T., Chetan, M., Bay, C., Damiani, R., Kaminski, M., Loth, E. (2019). Structural Design of a 1/5th Scale Gravo-Aeroelastic Scaled Wind Turbine Demonstrator Blade for Field Testing. Accepted in *2019 Wind Energy Symposium*.

Chapter 7

Conclusions

1. Key Results

Load-alignment via downwind coning can significantly reduce root flapwise bending loads. Based on the analytical analysis developed in this dissertation, for a three-bladed 13.2 MW turbine, downwind coning (~25°) can be used to eliminate the average bending loads at rated conditions. Less extreme coning angles (~8°) could be used to significantly reduce the loads (by 33%) such that the structural requirements can be met less expensively, with only minimal decrease in swept area (2% decrease). The SUMR turbine implemented an active coning schedule to align the rotor blades closer with the resultant loads at high wind speeds, but at low wind speeds the rotor extends to capture more power. The SUMR turbine does not experience the typical load increase that would accompany a transition from 3-bladed to 2-bladed rotors because of leveraging the load-aligned concept. In fact, the two-bladed SUMR rotor significantly lowered the loads while producing similar power outputs.

In reference to the UAE wind tunnel experiment, at low freestream velocities (high tip speed ratios), there was a pronounced tower shadow effect on the resultant flow angle deficit and fluctuations and blade bending moments. The flow-aligned fairing reduced the tower shadow effects. However, the fairing misaligned with the flow by 20° did not reduce shadow effects at any speed. At high upstream velocities (low tip speed ratios), unsteady spatially-distributed aerodynamic interactions dominated the chord-wise and span-wise characteristics more than tower shadow effects. The simulation model of the UAE simulated some aspects of the experiment accurately. Despite significant aerodynamic simplifications, the simulation reasonably models the cycle-averaged values of the flow field seen by the blade at a given azimuthal angle, away from the tower shadow region. Inside the wake region, the steady wake cannot predict the highly unsteady variations in flow angles, since the model neglects vortex shedding.

Based on FAST simulations of the full-scale SUMR rotor, the tower shadow effect on blade DEL was almost negligible (accounting for only about 3%) under realistic turbulent conditions. This is because the wind velocity fluctuations due to turbulence were much more impactful than those due to tower shadow. The trend did not seem to be highly sensitive to tower clearance. Therefore, based on these results a tower fairing would be largely wasted as a load-reducing approach in a downwind extreme-scale turbine since the tower shadow effect is generally negligible.

FAST simulations of the SUMR rotors indicated that the new set of longer rotor blades combined with pre-aligned load strategy increased power by 13.4% without increasing the peak loads the rotor experiences for steady conditions. However, the extra length does result in an 82.7% increase in blade mass and a 97% increase in fatigue damage when subjected to turbulent winds, both of which could increase the cost of the blade if these loads are a design driver. Including a hinge increases the power by an additional 4.6% beyond that of a pre-aligned rotor for the longest blades. However due to the assumed very slow response time of the coning angle, rapid wind speed changes make the rotor prone to off-design load misalignment, which led to peak loads about 40% greater than the baseline values. However, the increase in fatigue damage and peak loads can be highly mitigated by allowing the rotor to teeter. In particular, morphing combined with teeter results an increase in power of about 12% relative to a baseline rotor, without a significant increase in blade peak moments nor in DEL values. Furthermore, a morphing hinge can be designed such that it has a similar mass as that of a teeter hinge. This suggests that a 13.2 MW, downwind, two-bladed rotor can reasonably benefit from a combination of load-alignment, longer rotor blades, teeter, and morphing.

The SUMR-D turbine was simulated using FAST to provide data channels that will be available in the full experiment data set during operation. The results of the method show that average bending load of the simulated rotor with 12.5° coning has an average bending load that is only 25% of that for the same rotor with no coning angle, demonstrating the benefit of load alignment on the mean moments. Additionally, it was found that the ideal coning angle that would result in zero average bending load is nearly constant in Region II, and decreases with wind speed in Region III. However, atmospheric turbulence leads to large deviations of bending moments away from the moments, the coning has little effect on these deviatoric moments.

2. Contributions to the Field

This dissertation develops and demonstrates an original theory of load-aligned rotors. The relationship between centrifugal, gravitational and thrust bending moments was derived as a trigonometric function of coning angle. These relationships can be solved for a particular coning angle that eliminates (or reduces by a specified amount) the root flapwise bending load. The relationships can be used to predict how a conceptual or real wind turbine would perform with a different coning angle. This can simplify load-alignment experiments requiring only a single coning angle to be tested to glean information over an entire domain of coning angles.

This dissertation clearly demonstrated the effects of load alignment as a method of reducing blade mass or by means of increasing the swept area without increasing out-of-plane bending loads. The benefits of a morphing hinge have been quantified and discussed.

This dissertation explored the fundamental physics of tower shadow. The critical question relating to downwind turbines was answered, when is tower shadow problematic. Under steady wind conditions, e.g. a wind tunnel experiment, tower shadow has a great effect on bending loads, and therefore a tower fairing may be helpful. Under turbulent conditions e.g. field operation, the atmospheric fluctuations dominate the blade loading and a tower fairing is unnecessary.

3. Recommended Future Work

To better understand the potential benefits of morphing and to better optimize coning angle schedules, FAST and other rotor dynamic codes should be adapted to allow for variable coning during a simulation. In addition, it is recommended that other DLCs be investigated e.g. extreme gusts with direction changes to establish designs that are robust and closer to industry design practice. It is recommended that further work focuses on how cost is impacted by the extra mass of the blades, loads on other components, and the morphing hinge.

The load-alignment concept could be extended to larger scales for example 25 or 50 megawatts rated power. It is estimated that the effect of coning will be relatively smaller with increased sizes, therefore larger coning angles will be required for similar load-reductions. This should be analyzed.

Recommended future experimental work includes investigating the tower shadow effects for a downwind rotor in field conditions with cylindrical tower and for a lightweight self-aligning fairing to determine if the result for the FAST prediction is reliable. Additionally a large-scale downwind turbine experiment of tower shadow could include acoustic measurements with and without a tower fairing. The low-frequency “thumping” noise is a commonly cited concern for on-shore wind turbines.